Investigation of $CaWO_4$ Crystals for Simultaneous Phonon-Light Detection in the CRESST Dark Matter Search

Jelena Ninković

Technische Universität München

Max-Planck-Institut für Physik
(Werner-Heisenberg-Institut)

Investigation of $CaWO_4$ Crystals for Simultaneous Phonon-Light Detection in the CRESST Dark Matter Search

Jelena Ninković

Vollständiger Abdruck der von der Fakultät für Physik der Technischen Universität München zur Erlangung des akademischen Grades eines

Doktors der Naturwissenschaften

genehmigten Dissertation.

Vorsitzender:	Univ.-Prof. Dr. Manfred Lindner
Prüfer der Dissertation:	1. Priv.-Doz. Dr. Rainer Kotthaus
	2. Univ.-Prof. Dr. Lothar Oberauer

Die Dissertation wurde am 13.01.2005 bei der Technischen Universität München eingereicht und durch die Fakultät für Physik am 16.02.2005 angenommen.

Abstract

The goal of the CRESST Dark Matter Search is the direct detection of Weakly Interacting Massive Particles (WIMPs) via elastic scattering off the nuclei in a target absorber. Due to the low event rates expected for WIMP-nucleus scattering it is of crucial importance to suppress background signals which might mimic WIMP events as much as possible. Passive suppression is achieved by the use of radiopure materials and by operating the detectors in a deep underground location. In the second phase of the CRESST experiment an active signal-to-background discrimination is achieved with the use of low temperature scintillating calorimeters. Nuclear recoils, caused by neutrons and WIMPs, produce considerably less light than electron recoils of the same energy. Therefore, a simultaneous measurement of scintillation light and temperature rise can be used to identify the type of interaction.
In this work the properties and quality of $CaWO_4$ single crystals of different origin were studied. Special attention was attributed to the radiopurity and the optimization of the light output of large cylindrical crystals ($\phi = 40\,mm$; $h = 40\,mm$; $m = 300\,g$). A low level of radioactive contamination ($\sim 100\,\mu Bq/kg$) by isotopes of the natural decay chains was obtained. The influence of different parameters and conditioning procedures on the light yield of $CaWO_4$ crystals was studied resulting in a significantly improved reproducibility of the scintillation properties. The effect of different mechanical and thermal treatments on the energy resolution and the light output of the crystals was investigated and an energy resolution $\Delta E/E \sim 8\%$ at $E = 662\,keV$ was obtained. In particular, a new technique for the measurement of nucleus dependent quenching factors was developed and the quenching factor of tungsten in $CaWO_4$ was measured for the first time. Based on the obtained results, restrictive upper limit could be obtained for the spin-independent WIMP-nucleus scattering cross section using CRESST Phase II prototype detectors.

Contents

Chapter 1

The quest for Dark Matter

1.1 Introduction

The existence of (non-baryonic) matter that does not absorb or emit electromagnetic radiation was first proposed by Zwicky in 1933 [Zwi33] based on estimates of the total mass of clusters of galaxies. Nowadays there is overwhelming indirect evidence for the existence of such Dark Matter, sensed by gravitational effects only, but up to the present day it has not been detected directly despite the increasing world wide effort. Over the last few years, precision measurements of the microwave background spectrum, combined with other astronomical and astrophysical data, have yielded the basic parameters of the cosmological model of the Universe with high accuracy. It has been shown that luminous and non-luminous baryonic matter only represents about 4 % of the mass of the Universe, while non-baryonic Dark Matter represents a much larger part (about 26 %) of the total mass. About 70 % of the total density needed to close the Universe is energy of unknown nature, called Dark Energy. The Dark Matter enigma appears to find a well-motivated solution in supersymmetric Weakly Interacting Massive Particles, generically called WIMPs. The CRESST [1] Dark Matter search is dedicated to directly detect WIMPs.
This chapter summarizes the arguments for the existence of Dark Matter and reviews the main candidates. The physics principles of direct detection of Dark Matter are then presented followed by a description of some of the leading experiments.

1.2 Motivation for Dark Matter search

The discovery of Hubble´s law of an expanding universe [Hub29] at the beginning of the last century together with the first measurements of the cosmic microwave

[1] Cryogenic Rare Event Search with Superconducting Thermometers

background (CMB) were a solid base for the nowadays well established Standard Cosmological Model relaying on the "Big Bang" scenario. This extremely sophisticated model is able to explain the thermal evolution, relic background radiation, abundance of light elements, structures at all scales and many other properties of the Universe.
The Cosmological Model is based on: the Einstein equations (relating the geometry of the Universe with its matter and energy content), the metric (describing the symmetries of the problem) and the equation of state (specifying the physical properties of the matter and energy content). For an isotropic and homogeneous universe, as supposed by the so called "Cosmological Principle", a specific form of the metric, the so called Friedmann-Robertson-Walker metric, applies

$$ds^2 = -\,c^2 dt^2 + a^2(t)\left[\frac{dr^2}{(1\,-\,kr^2)} + r^2 d\omega^2\right], \tag{1.1}$$

where $a(t)$ is the so-called scale factor and the constant k, describing the spatial curvature (values k=-1, 0, +1 correspond to spatially open, flat or closed Universe). The Einstein equations can be solved for this metric, giving the Friedmann equation that with an introduction of the Hubble parameter H, the critical density ρ_c and $\Omega = \rho/\rho_c$ can be written as

$$\Omega - 1 = \frac{k}{H^2\,a^2}\,. \tag{1.2}$$

The sign of k is therefore determinated by the value of Ω, where three cases can be distinguished:

1. $\rho < \rho_c$; $\Omega < 1$; $k = -1$; open Universe,
2. $\rho = \rho_c$; $\Omega = 1$; $k = 0$; flat Universe,
3. $\rho > \rho_c$; $\Omega > 1$; $k = 1$; closed Universe.

Defining normalized densities of matter, Ω_m, curvature, Ω_k, and cosmological constant terms, Ω_Λ, as

$$\Omega_m \equiv \frac{8\,\pi\,G\,\rho_0}{3\,H_0^2}\,,\quad \Omega_k \equiv \frac{-\,k}{a_0^2\,H_0^2}\,,\quad \Omega_\Lambda \equiv \frac{\Lambda}{3\,H_0^2}\,, \tag{1.3}$$

where G is the Newtonian gravitational constant, Λ is the cosmological constant and ρ is the density of the Universe (subscript 0 denotes present day values) equation 1.2 can be written as

$$\Omega_m + \Omega_k + \Omega_\Lambda = 1\,. \tag{1.4}$$

Despite its predictive power the Standard Cosmological Model is still only a partial model that can not describe the first instants of our Universe history. It does not explain the finite baryon density, the extraordinary flatness and smoothness of the Universe on very large scales and the origin of primordial density perturbations that gave rise to the cosmic structure formation. A Cosmic Inflation (exponential expansion in the early stage of the Universe) provides a solution to some of these problems. It nicely explains the isotropy and homogeneity on very large scales and it generically predicts a flat Universe i.e. $k=0$. Indeed we now have convincing evidence from Cosmic Microwave Background (CMB) measurements that $\Omega = 1$ [Spe03]. WMAP[2] and high red-shift SuperNova (SN) observations indicate a non-zero value for the cosmological constant (therefore existence of Dark Energy) and give impressively consistent results for the value of Ω_M [Spe03] [Kno03]. The contribution of the luminous matter to the total density is however by far too small ($\Omega_{lum} = 0.002 - 0.006$ [Fuk98]) to saturate Ω_m, implying the presence of Dark Matter in the Universe. The standard Big Bang Nucleosynthesis (BBN) sets stringent constraints on the total amount of baryons, which implies that non baryonic Dark Matter has to be present in the Universe.
The concepts of Dark Energy and Dark Matter do not find an explanation in the framework of the Standard Model of particle physics. Dark Matter is therefore a motivation to search for physics beyond the Standard Model. Moreover, it is a nice example of the strong interplay between theoretical and experimental particle physics, cosmology and astrophysics. Particle physics theories beyond the Standard Model predict new particles that turn out to be suitable Dark Matter candidates. On the other side, cosmological and astrophysical observations constrain the properties of such particles and consequently the parameters of such new theories.

1.2.1 The evidence for the existence of Dark Matter

The Galactic scale

The most convincing and direct evidence for Dark Matter on galactic scales comes from the observations of flat rotation curves of spiral galaxies[3] (see figure 1.1). From Newtonian dynamics the rotational velocity is expected to be

$$v(r) = \sqrt{\frac{G\,M(r)}{r}}\,. \tag{1.5}$$

[2]The Wilkinson Microwave Anisotropy Probe (WMAP)

[3]Rotation curves are graphs of rotational velocities of stars and gas as a function of their distance from the galactic center.

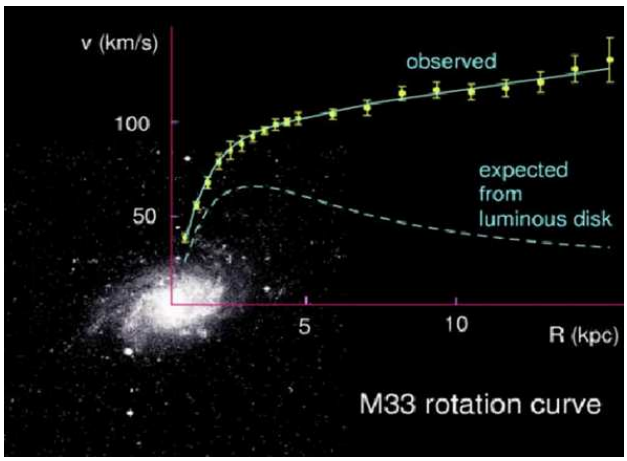

Figure 1.1: Rotation curve of galaxy M33 [Kha02] (see text).

So, it should be falling $\propto 1/\sqrt{r}$ beyond the optical disc marking the region containing the entire luminous mass of the galaxy. The fact that $v(r)$ is approximately constant implies the existence of a halo with $M(r) \propto r$ and $\rho \propto 1/r^2$. Despite the uncertainties of the slope in the innermost regions of galaxies there is a consensus about the shape of Dark Matter halos at large distances. The measured rotation curves of disk galaxies provide strong evidence for the existence of a spherical Dark Matter halo. The total amount of Dark Matter is hard to be estimated as it is not known to what distances Dark Matter halos extend. Other observations on both galactic and sub-galactic scales indicate the presence of Dark Matter and here only some of them will be mentioned: weak gravitational lensing of distant galaxies by foreground structure [Hoe02] and the velocity dispersions of dwarf spheroidal galaxies [Mat98] which imply mass-to-light ratios larger than those observed in our "local" neighborhood.

The Galaxy Clusters scale

Clusters of galaxies are the largest gravitational bound systems in the Universe. They have typical radii of 1.5 Mpc and typical masses of $5 \times 10^{14}\,\mathrm{M}_\odot$. In 1933 Zwicky noted, making use of the virial theorem, that these systems appear to contain large amounts of Dark Matter [Zwi33]. Today, the estimates [Bah92] [Kas98] [Car99] are consistent with a value of $\Omega_m \sim 0.2 - 0.3$ on cluster scales. Clusters of galaxies turn out to be the most powerful X-ray sources in the sky. The emission extends over the entire cluster and thus reveals the presence of large amounts of hot X-ray emitting gas. Using the virial theorem (assuming this gas to be in the hydrostatic equilibrium) the total cluster mass can be estimated. Results obtained from these measurements indicate the existence of a substantial amount of nonbaryonic Dark Matter in clusters.

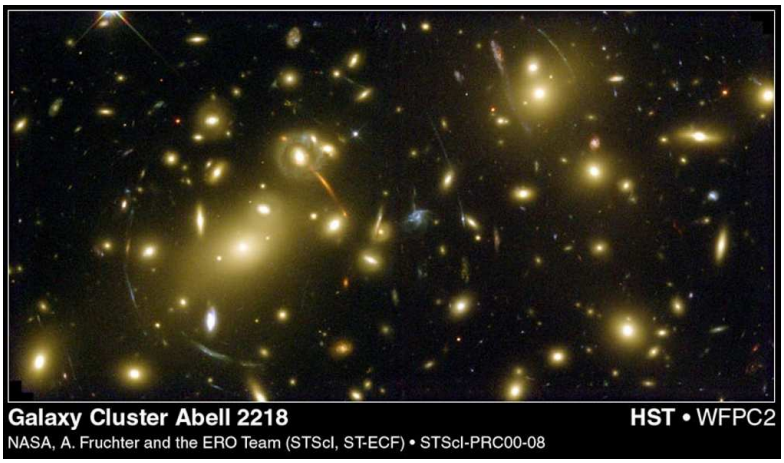

Figure 1.2: Gravitational arcs observed in the galaxy cluster Abell 2218 (see text).

The observation of the giant arc-like structures in galaxy clusters due to the gravitational lensing effect (see figure 1.2) gives, in a rough agreement with other observations, estimates of the Dark Matter content [Sad99].

Cosmological scales

The existence of background radiation originating from photons created in the early Universe was predicted in 1948 [Alp48] and discovered in 1965 [Pen66]. Significant improvement of the detection technology showed the existence of CMB anisotropies.
Today, the analysis of these anisotropies enables accurate testing of cosmological models and puts stringent constraints on cosmological parameters.

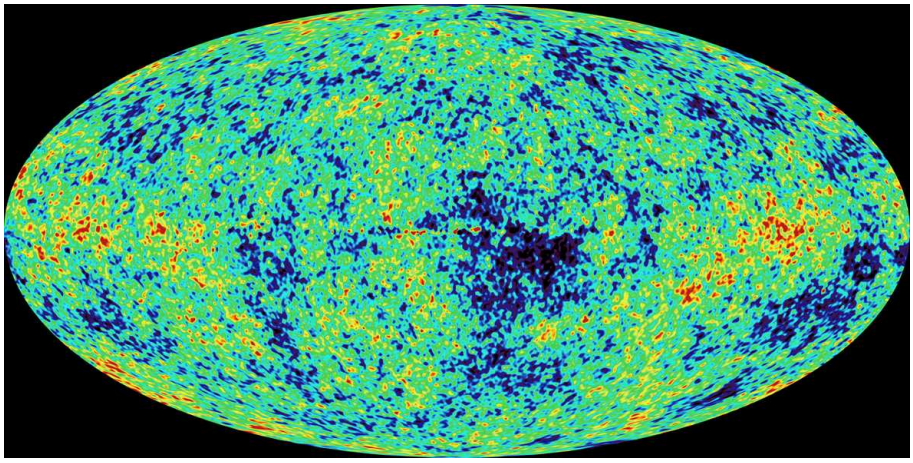

Figure 1.3: CMB temperature fluctuations seen by WMAP. Image from http://map.gsfc.nasa.gov .

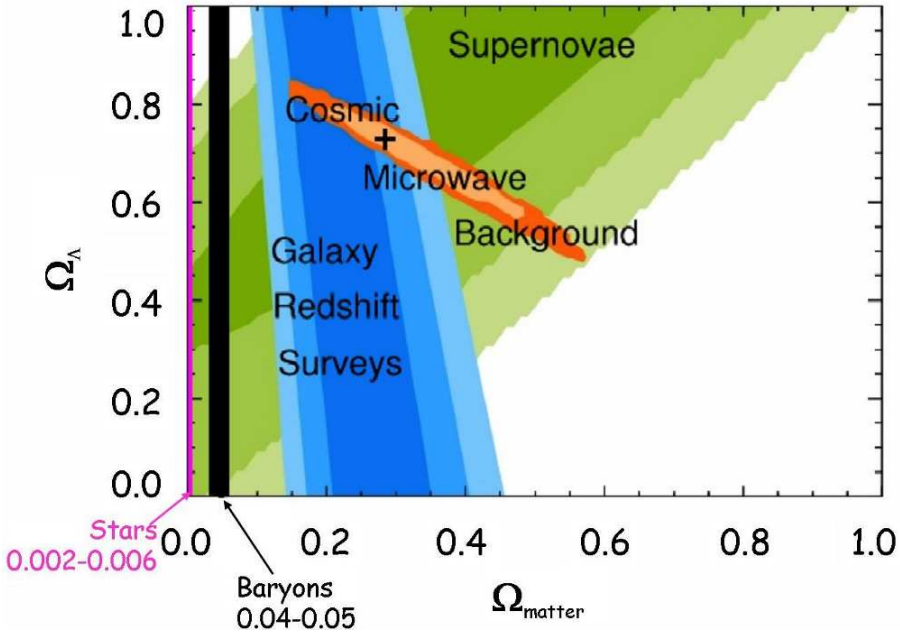

Figure 1.4: Current cosmological constraints on the matter density Ω_m and the energy density Ω_Λ give the best estimate marked with a cross at $\Omega_m = 0.27$, $\Omega_\Lambda = 0.73$. The baryon density (black vertical band) does not exceed 0.05. The rest of the matter is non-baryonic. Luminous matter (pink vertical band) does not contribute more then 0.006. Figure adapted from [Gon04].

The analysis of WMAP data (see figure 1.3) gave the following values for the abundance of baryons and matter in the Universe

$$\Omega_b\, h^2 \;=\; 0.024 \,\pm\, 0.001\,, \quad \Omega_m\, h^2 \;=\; 0.14 \,\pm\, 0.02\,, \tag{1.6}$$

where Ω_b is the normalized baryonic density and h = 0.72±0.05 Hubble parameter [Spe03].
The summary of present measurements of the matter density Ω_m and the energy density Ω_Λ are shown in figure 1.4 [Gon04]. The best estimates from combined cosmological constraints are $\Omega_m = 0.27$ and $\Omega_\Lambda = 0.73$.

1.3 Dark Matter candidates

As illustrated in the previous section, the evidence for the existence of non-baryonic Dark Matter is compelling on all astrophysical scales. The inventory of Dark Matter candidates is rather large. Whereas baryonic Dark Matter is in the form of "standard" astropartical objects the nature of non-baryonic Dark Matter is still unknown. A summary of plausible candidates is presented in the following.

1.3.1 Baryonic candidates

Since baryonic matter interacts with light, even if the baryons are non-luminous themselves, they would absorb light. This results in stringent observational limits on many plausible candidates [Spi99]. Thus baryonic Dark Matter can not be in the form of hot diffuse gas as this would result in a larger X-ray flux than the observed, nor in the form of cold gas since it would absorb light and re-emit it in the infrared. Neutron stars or black holes that are created in supernova explosions would eject heavy elements into the galaxy and thus could be spectroscopically observed. White dwarfs are the next candidate since they are not massive enough to reach the supernova phase. However, they would produce too many light elements or too many elements heavier then H and He that is not observed. The most plausible candidates are brown dwarfs, stars with small mass ($0.01\,M_\odot < M < 0.08\,M_\odot$), which never ignite hydrogen and thus shine only due to gravitational contraction. As most of the stars are small, one would expect significant number of such objects in the galaxy. Up to the present time their existence is difficult to prove. Nevertheless, they appear to be the most plausible candidate of baryonic Dark Matter. Finally primordial black holes, which have been created in the early Universe could also be a good candidate, but the main objection against them is a lack of a plausible mechanism for their formation. All mentioned objects are usually collectively called MACHOs[4] and may be identified through gravitational lensing [Alc00].

1.3.2 Non-baryonic candidates

Non-baryonic candidates are usually classified as hot and cold Dark Matter (also an intermediate state, called warm Dark Matter has been proposed), depending on their kinematical state in the early Universe at the time of decoupling of light and matter. Hot Dark Matter candidates would have been relativistic, cold Dark Matter ones non-relativistic. The reason for such a classification originates from the fundamentally different consequences for structure formation in the Universe, like formation of superclusters and clusters of galaxies. Hot Dark Matter would form huge structures first, cold Dark Matter vice versa. The important efforts of research groups using supercomputers for N-body simulations of huge parts of the Universe showed that structure formation cannot be understood with dominantly hot Dark Matter. A consistent scenario results for a substantial cold Dark Matter component and a rather negligible hot Dark Matter component [Dav85].

Standard Model neutrinos

Neutrinos have been considered, until recently, as a natural hot Dark Matter candidate [Sch88]. However, recent measurements of the neutrino mass [Wei03],

[4]MAssive Compact Halo Objects (MACHOs)

gave the upper limit of $m_\nu < 2.05\,eV$ (at 95% CL). This implies an upper bound on the total neutrino relic density of $\Omega_\nu h^2 \leq 0.07$, which means that neutrinos are not abundant enough to be a significant component of the Dark Matter [Han04].

Sterile neutrinos

Sterile neutrinos are hypothetical particles similar to neutrinos but with gravitational interactions only. They were proposed as warm Dark Matter candidate by Dodelson and Widrow in 1993 [Dod94]. Recent results from the WMAP [Spe03] indicate the marginal role of warm Dark Matter, although at present it is not definitely ruled out by any observations.

According to the most popular models a good candidate for non-baryonic Dark Matter has to satisfy several criteria enclosed into a acronym CCDM - Cold Collisionless Dark Matter:

- **Cold** means that the particles are nonrelativistic at the time of decoupling and therefore able to cluster gravitationally;
- **Collisionless** means that the interaction cross-section between Dark Matter particles (and between Dark Matter and ordinary matter) is so small to be negligible for densities found in Dark Matter halos. The particles are only gravitationally bound.

In addition, the lifetime of the particle must be comparable to or greater than the present age of the Universe, (∼14 billion years). A special subclass of this general group are the so called Weakly Interacting Massive Particles (WIMPs). Of a large number of possible WIMPs here only the well motivated and most interesting candidates will be presented.

Supersymetric candidates

Supersymmetric (SUSY) theories hypothesize the existence of a SUSY partner (or sparticle) for each particle of the Standard Model. They are characterized by a new quantum number called R-parity, where R = 1 for Standard Model particles and R = - 1 for SUSY particles (sparticles). Assuming R-parity conservation, sparticles can only decay into an odd number of sparticles which implies the existence of a stable Lightest Supersymmetric Particle (LSP). Therefore, the LSP can be destroyed only via pair annihilation and thus in a Universe that is asymmetric in its particle and antiparticle contents it is a viable WIMP candidate.

The best motivated LSP candidates are the neutralinos, the SUSY partners of the photon, W- and Z-bosons or mixtures there of. Sneutrinos have large annihilation cross-sections that require a mass exceeding several hundred GeV to be cosmologically interesting. "Ordinary" sneutrinos have been already excluded by direct Dark Matter searches [Fal94] while the other two in the supersymmetric scenarios have some unattractive properties and are therefore less favored.

Axions

Axions are hypothetical light pseudoscalar particles that arise in models which resolve the strong CP problem in quantum chromodynamics (QCD) by the Peccei-Quinn (PQ) mechanism [Pec77]. They could have been produced in the early stages of the Universe. They are expected to be very light particles ($1\mu\,eV < m_{axion} < 2\,meV$ [Raf00]) that are extremely weakly interacting with ordinary particles. This implies that they were not in thermal equilibrium in the early Universe and are sufficiently long-lived to be attractive cold Dark Matter candidate. Axions could also be produced in the core of the stars by means of the Primakoff conversion of the plasma photons. Observed properties of globular cluster stars [Raf99] and laboratory searches for solar axions [col04a] have placed stringent limits on the coupling of axions to photons.

Other candidates

Although CCDM is still the dominant form of Dark Matter it does not give a picture consistent with observations on small scales (from 1 Mpc down to the scales of galaxies and below). It is believed that the discrepancies come from the specific assumptions about the nature of Dark Matter. The perfect agreement that has been achieved on the large scales involves only computations based on Newton's and Einstein's laws of gravity while on the small scales complex hydrodynamical interactions must be included. Two main problems can be distinguished at the small scales:

1. Problem of substructures: number of small halos and galaxies within the larger objects is smaller than expected from the CCDM calculations;

2. Density profile of Dark Matter: Dark Matter halos should exhibit a cuspy core in which the density rises sharply as the distance from the center decreases. Many studies of spiral galaxy kinematics, on the other hand, find Dark Matter halos with cores that depend little on radius.

Theoretical explanations for the absence of substructures are numerous, however explanations of the non-cuspy density profile are still missing. Solution can be found in a modification of the nature of Dark Matter. Among the numerous models of alternative forms of Dark Matter, here only two of them will be

mentioned: Strongly self-Interacting Dark Matter (SIDM) and Repulsive Dark Matter (RDM). SIDM can explain the reduced number of small structures but it does not offer an explanation for the density profile. RDM consists of a condensate of massive bosons with a short range repulsive potential and therefore can explain non-cuspy density profile. For an overview of other possible scenarios see for example [Ost03].

1.4 The direct detection of Dark Matter

Direct detection experiments appear today as one of the most promising techniques to detect particle Dark Matter. The basic idea on which all direct detection experiments are based relies on the fact that if the Galaxy is filled with WIMPs, then many of them should pass through the Earth, making possible the detection of the interaction of such particles with ordinary matter by elastic scattering with a nucleus of the detector material. Indirect detection relies on observing the radiation produced in Dark Matter annihilations. The two quantities which are crucial to both direct and indirect detection are the Dark Matter density ρ_0 and the velocity dispersion, $\overline{v} = \sqrt{\langle v^2 \rangle}$, of Dark Matter particles. Direct detection relies on local properties of both parameters (near the Earth) while the detection rates of indirect searches are strongly affected by uncertainties in matter distribution. In order for the galaxies to reach a constant outer rotation curve, the density profile of the Dark Matter halo must fall approximately proportional to r^{-2} in the relevant radius range. Such a profile resembles the density structure of an isothermal, self-gravitating system of particles which is characterized by a constant velocity dispersion. Measured rotation curves of dwarf spiral galaxies are well represented by the following phenomenological density distribution

$$\rho_{DM} = \frac{\rho_0 \, r^3}{(r + r_0)\,(r^2 + r_0^2)}, \tag{1.7}$$

where ρ_0 is central density and r_0 a core radius [Bur95]. The existence of a "core" where the density is approximately constant has been challenged by high resolution N-body simulations [Nav96] and the canonical value for the density of Dark Matter halo is $\rho_0 = 0.3\, GeV/cm^3$ [Jun96]. The form of the halo distribution function presumably depends on the details of the collapse process which formed the galaxy. General dynamical arguments suggest that WIMP velocities were thermalized by the fluctuations in the gravitational collapse. Based on this it can be assumed that WIMPs have approximately Maxwell-Boltzmann velocity distribution [5] (assuming non-rotating WIMP halo) [Fre88]. The canonical value for velocity dispersion in our Galaxy is $\overline{v} = 270\, km/s$ [Jun96]. Yet, one has to

[5] The velocity dispersion is directly related to the asymptotic flat rotation velocity as $\overline{v} = \sqrt{3/2}\, v_\infty$.

take into account considerable uncertainties and model dependencies when using these values.

1.4.1 Nuclear form factor

The most important direct detection process is elastic scattering on nuclei, and recoil energy can be measured by means of various experimental techniques with different nuclear species. The detection efficiency for nuclear recoils might be different from that for the background events and there is a form factor correction dependent on nuclear radius and recoil energy which also differs for spin-dependent and spin-independent interactions [Lew96a]. The form factor parameterizes the loss of coherence due to the finite size of the nucleus for the WIMP-nucleus interaction as the WIMP-energy increases. Both spin dependent (axial) and spin-independent (scalar) cross sections are modified at high momentum transfer q by form factors that reflect the spatial distribution of nucleons inside the nucleus. When the momentum transfer to the nucleus $q = \sqrt{2\, m_N\, E_r}$ is such that the de-Broglie wavelength $\lambda = h/q$ is smaller than the size of the nucleus, the effective scattering cross section decreases with increasing momentum. While spin-independent form factors are simply related to nuclear densities, spin dependent cross sections reflect delicate aspects of nucleonic and nuclear structure [Eng92]. Spin-independent scattering is a coherent process and an analytic expression for the form factor can be derived. At non-zero momentum transfer the form factor is defined as the Fourier transform of the nuclear matter distribution, which in this case has a well defined form. In contrast, in the spin dependent case the form factor calculations require significant effort since nuclear properties have to be calculated for each nucleus with an appropriate nuclear model. The effective cross section for both types of interaction can be thus written as

$$\sigma = \sigma_0\, F^2(E_r)\,, \tag{1.8}$$

where σ_0 is the zero momentum transfer cross section which contains all dependencies on the specific interaction. From the detailed calculation (see for example [Ber04b]) the cross section at zero momentum transfer for spin-independent WIMP interaction is related to the mass of the target nucleus, m_N by

$$\sigma_{0si} \propto \mu^2\, m_N^2\,, \tag{1.9}$$

where μ is the reduced mass[6]. Therefore, for the coherently interacting WIMPs very massive nuclei are desirable since the interaction cross section scales as the nucleus mass squared. However, in this case coherence loss must be considered. In the case of spin-dependent interaction σ_0 is proportional to the nuclear spin factor, $\lambda\, J(J+1)$. For the measurements of the spin-dependant interaction cross

[6] $\mu = (m_\chi\, m_N)/(m_\chi + m_N)$

section the most desirable detector nuclei would be such which match nuclear and WIMP masses and therefore maximize energy transfer.

1.4.2 Energy spectrum

The energy deposited in a detector, E_r, due to the WIMP nucleus elastic scattering is

$$E_r \;=\; \frac{m_\chi^2\, m_N}{(m_\chi \,+\, m_N)^2}\, v^2\, (1 - cos\theta)\,, \tag{1.10}$$

where m_χ and v are WIMP mass and velocity respectively and θ is the scattering angle in the center of mass frame.
The differential rate for the elastic WIMP-nucleus scattering is given by the equation [Jun96]

$$\frac{dR}{dE_r} \;=\; N_T\, \frac{\rho_0 \sigma_0}{2 m_W \mu^2}\, F^2(E_r) \int_{v_{min}}^{v_{esc}} \frac{f_1(v)}{v}\, dv\,, \tag{1.11}$$

$$v_{min} \;=\; \sqrt{\frac{E_r\, m_N}{2\,\mu^2}}\,,$$

where N_T represents the number of target nuclei, $f_1(v)$ is the velocity distribution of WIMPs in the laboratory frame, m_N is the mass of the nucleus and μ is the reduced mass. Assuming simple Maxwellian WIMP halo as defined in section 1.4.1 and neglecting (for simplicity) motion of Earth and Sun integration over all detectable recoil energies (between the energy threshold of the detector, E_{thr} and $E_{max} \;=\; 2\mu^2 v^2 / m_N$, for light WIMPs where $F(E_r) \;\sim\; 1$ gives the total event rate

$$R \;=\; N_T\, \frac{\rho_0\, \sigma_0}{m_W\, m_N}\, \frac{2}{\sqrt{\pi}}\, v_0\, \exp\left(-\frac{E_{thr}\, m_N}{2\,\mu^2\, v_0^2}\right)\,, \tag{1.12}$$

where $v_0 \;\simeq\; 220\, km/s$ is the rotational velocity of the Sun around the Galactic center. In order to obtain a more realistic result the motion of the Earth and the Sun should be accounted. A general WIMP will have both scalar and spin-dependent interactions with the nucleus, so there will be a scalar cross section, and a spin cross-section. The differential and total event rate will be the sum of the differential and total event rates due to the two interactions. For the scalar interaction, an analytic form factor can be used. For the spin interaction, the form factor will differ from nucleus to nucleus. These must generally be integrated numerically to obtain a total cross section. Form-factor suppression becomes small for target nuclei of sufficiently low mass. For a detailed calculations see for example [Goo85] [Jun96].
The direct experiments measure the differential event rate (energy spectrum).

Registered counts contain the signal and the background. Therefore, the three main experimental requirements for direct detection experiments are [Ram99]:

1. A low as possible energy threshold due to the quasi exponential dependence of signal vs. recoil energy;

2. A high background suppression in order to allow a spectrum of rare nuclear recoils to be observed;

3. A detector mass as high as possible in order to compensate the low interaction cross section.

Figure 1.5 illustrates the quasi-exponential dependence of the signal rate on the recoil energy for three hypothetical WIMP masses, for the $CaWO_4$ target material.

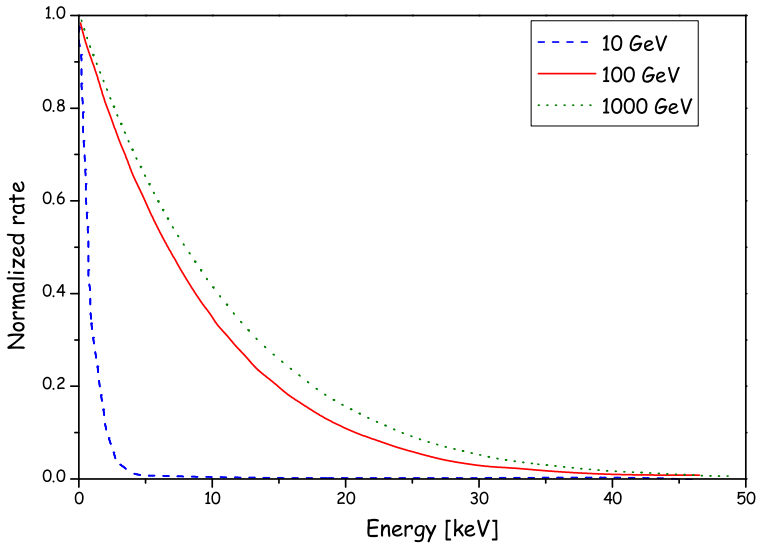

Figure 1.5: Normalized recoil spectra for WIMP elastic scattering on $CaWO_4$ for WIMP masses of 10, 100 and 1000 GeV/c^2.

1.4.3 WIMP exclusion limits

Constraints on the WIMP interaction cross section are set by calculating the upper limit of the theoretical event rate, which is compatible with the observed event rate. Any set of parameters which produces a theoretical event rate exceeding this limit is then excluded to a given confidence level (usually 90% CL). As a

first step in the calculation procedure the theoretical WIMP recoil spectrum has to be convoluted with the experimental resolution and then, for a given mass, compared with the observed spectrum applying the 90% CL criterion. For details of the calculation of the exclusion limits see e.g. [Gre02], [Tov00], [Ang02], [Yel02].

1.4.4 Experimental sensitivities

The expected WIMP event rates are $\leq 0.1\,\mathrm{event/(kg\,day)}$ [Abr02],[Ben02] while the background rates in detectors operated at the surface of the Earth, from naturally occurring radioactivity are orders of magnitude higher. The sensitivity of a WIMP search is determined by the ability to detect a WIMP energy spectrum on top of energy depositions by the background particles. There are four ways to deal with this challenge.
Consider first the case of a detector that cannot distinguish WIMPs from background particles. Any such detector observes some spectrum of background particle interactions. With such detector one can claim a WIMP signal by observing the expected exponential recoil-energy spectrum on top of its background spectrum while conclusively showing that such a spectrum could not arise from interactions of any other particle. Conversely, such a detector can exclude a WIMP model if the model predicts a spectrum with a higher event rate than the observed background. If no counts are observed, the sensitivity improves as MT, where M is detector mass and T is exposure time. The 90% CL upper limit on zero observed counts is 2.3 events, so the event rate excluded at 90% CL in some empty energy bin is $2.3/MT$. However, once background events are seen, the sensitivity improvement slows down and finally stops. Once enough counts have been collected that the statistical error on the background spectrum is small compared to the spectrum itself, the WIMP sensitivity is fixed by the background spectrum. Increasing the mass or the integration time yields no more improvement. The only way to improve WIMP sensitivity is to reduce the background spectrum.
The next possibility is background subtraction. If one has independent knowledge that predicts the background spectrum, then it is possible to subtract this spectrum and look for a WIMP spectrum in the residuals. If the background model fits the observed spectrum perfectly, then the upper limit of the residual number of counts in an energy bin increases as $\sqrt{MT}$ and the WIMP-nucleon cross section being probed decreases as $1/\sqrt{MT}$. In any such analysis, the required accuracy of the background model also grows with time: the fractional systematic error on the background subtraction must decrease as $1/\sqrt{MT}$ in order for statistical errors to continue to dominate. Most experiments of this type eventually reach the point where the systematic errors cannot be further decreased and the sensitivity stops improving.

Sensitivity can also be improved by background rejection. This may be done in many ways, but is always based on finding some signature that uniquely distinguishes WIMP events from background events. One method that has been pursued by many groups is nuclear-recoil discrimination. WIMPs and neutrons interact with nuclei, producing nuclear recoils. Most other background particles interact dominantly with electrons, producing electron recoil signatures. Therefore, rejection of the electron recoil background puts one back into the first situation above, but with a much lower background rate. However, there are indistinguishable signatures of electron and nuclear recoils such that there will always be a certain contamination of nuclear with electron recoils. The misidentification rate is measured using a calibration data set (usually a photon source producing electron recoils in the detector) and is used together with the measured electron recoil background to predict the number of misidentified electron recoils. This prediction is subtracted from the observed nuclear-recoil rate. As discussed above, this only works until systematics dominates.
A second class of background-rejection techniques utilizes the unique kinematics of WIMP interactions. One such signature would be diurnal variation. Because the Earth and the Sun move at approximately $232\,km/s$ through an isotropic WIMP halo (the $220\,km/s$ is the rotational velocity of the Sun around the Galactic center plus the additional Earth velocity of $12\,km/s$ relative to the disk), WIMPs primarily come from the direction into which the solar system is moving. Because of the Earth's rotation about its axis, this direction completes a circle in the lab frame once per day. A detector sensitive to the direction of the recoiling nucleus would see a diurnal variation in the angular distribution of nuclear recoils with a specific phase.
A similar technique is to observe an annual modulation in the rate and recoil-energy spectrum. The Earth's velocity with respect to the halo is sinusoidally modulated due to the Earth's orbit around the Sun. The lab-frame velocity of the WIMPs thus changes with a one year period, yielding a small variation in the WIMP flux and recoil energy spectrum. It is not necessary to measure the recoil direction. The modulation amplitude of the WIMP interaction rate is a few percent. The known phase of the annual-modulation provides an additional handle for rejecting background events and instrumental effects. On the other hand, such experiments require incredible stability, especially if the signal is a small modulation on a large background signal.

1.4.5 Sources of particle background

Rare event searches are currently limited by radioactive background signals due to cosmic rays, natural or induced radioactivity. The shielding against cosmic radiation is achieved by installing the setup in a deep underground site and against environmental radioactivity by selection of the materials to be used in

the experimental apparatus and by implementing adequate shielding. For WIMP searches, special attention must be devoted to neutrons since they scatter off nuclei and can mimic a WIMP signal.

Cosmic rays

Primary cosmic radiation is mainly composed of a hadronic component, mainly protons and a smaller fraction of α particles and heavier nuclei (99%) and a leptonic component of electrons (<1%), gammas and neutrinos ($\approx 0.01\%$). Due to a very high interaction probability with atmospheric atoms only a very small fraction will reach the surface of the Earth.
Secondary cosmic radiation at see level is composed of about 75% muons, $\leq 25\%$ electrons and $< 1\%$ of protons and neutrons. Muons, the most penetrating component, are the main source of background in low-counting facilities. Muons can contribute to the detector background in different ways: by depositing energy in the detector itself; by producing energetic electrons which induce secondary electrons and gamma radiation; by interacting with materials surrounding the detectors followed by X, γ and neutron emission. Effective shielding against muons is achieved by installing the experimental setup in deep underground sites. Figure 1.6 shows the depth-intensity relation of cosmic ray muons.

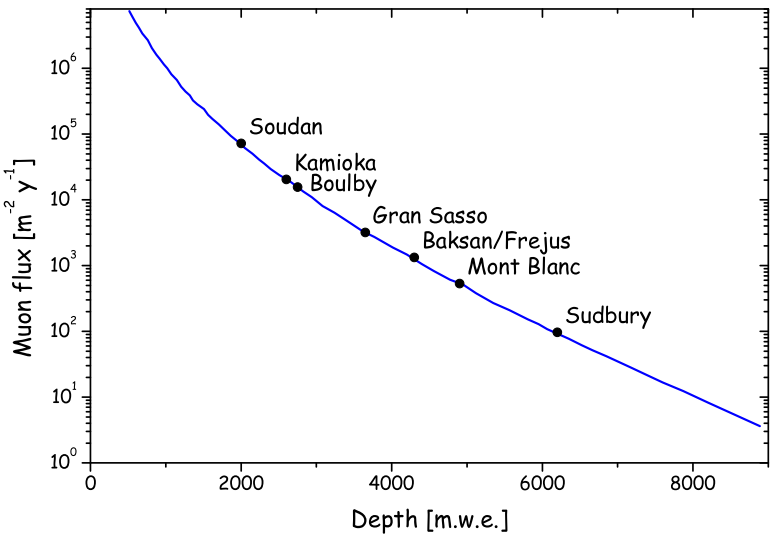

Figure 1.6: The depth - intensity relation of cosmic ray muons. The circles indicate values for some of the large depth underground laboratories. The depth is given in meters of water equivalent. Figure adapted from [Kos92].

Environmental radioactivity

Among the survivor isotopes of the original synthesis of matter in the Solar system, the most important radionuclides are ^{40}K,^{87}Rb and those belonging to the natural radioactive chains [Eis87].
Potassium is present in nature in three different isotopes of which only ^{40}K is β unstable with a half-life of 1.3×10^{9} y. Despite its low isotopic abundance (0.012%) it is one of the most relevant contributors to natural radioactivity.
Rubidium is present in nature in two isotopes of which only ^{87}Rb is radioactive with 4.8×10^{10} y half-life. It has an isotopic abundance of 27.8% and it is a pure β emitter.
From the four natural **radioactive decay chains** today only Uranium, Thorium and Actinium are still observable since there half-lives are of the order of the age of the Earth. Uranium and Thorium are usually present in nature with an abundance ranging from a few to several tens of ppm (parts per million).
Among the man-made radionuclides, mainly originating from weapon tests or nuclear power plant accidents, the most important ones are ^{90}Sr and ^{137}Cs. They are both β emitters and relatively long lived: 20.8 y and 30.3 y half-life, respectively. The β emission of ^{137}Cs is followed by a 661.6 keV γ emission. In the production lines in steel works, cobalt is commonly used and therefore the radionuclide ^{60}Co is present in all modern types of steel. It is a β emitter with 5.12 y half-life and it decay leads to cascade γ lines of 1.173 and 1.332 MeV.

Neutrons

The dominant sources of neutrons at large depth underground laboratories are (α, n) reactions on light elements (e.g. Li, F, Na, etc.) and spontaneous fission, mainly of ^{238}U. In general, at a depth of 3000 - 4000 m.w.e.[7], the flux of neutrons from activity in the experimental environment is two to three orders of magnitudes higher than the flux of neutrons from cosmic ray muons.

1.4.6 Description of leading direct detection experiments

As already mentioned, it is useful to classify the existing experiments according to whether or not the detectors are able to distinguish between the WIMP signal and background on the event by event basis. Figure 1.7 shows an overview of the detection principles implemented in the most prominent existing and coming experiments.

[7] meter water equivalent

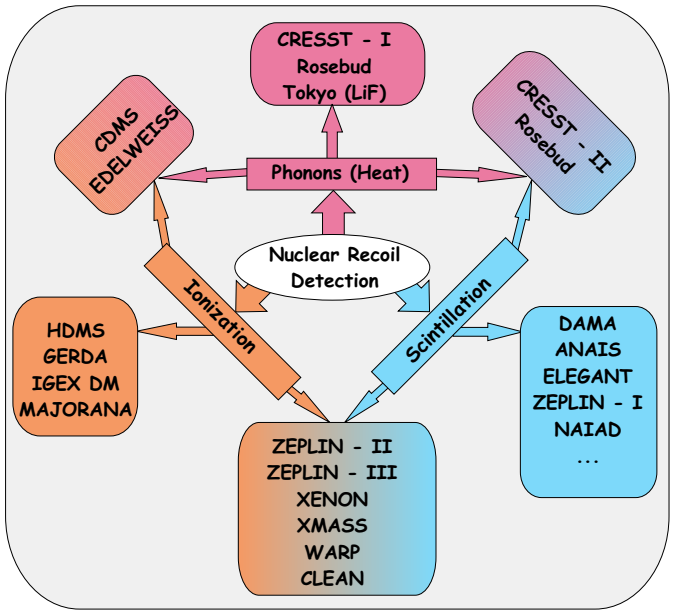

Figure 1.7: Detection techniques employed in the most prominent direct Dark Matter experiments.

Non-discriminating experiments

Classical germanium detectors are employed in the Heidelberg-Moscow experiment (HDMS). Due to the substantial work on low-background conditioning, they have achieved the lowest background rate (0.05 counts/kg/keV/day above 15 keV) without background rejection technique [Bau99]. Presently, the project GERDA has been proposed where 100 kg of high purity germanium enriched in ^{76}Ge will be enclosed by high purity nitrogen. The MAJORANA project is aiming for the operation of 1/2 ton of high purity ^{76}Ge detectors.
The list of experiments using NaI as a target material is long (DAMA, ANAIS, ELEGANT, NAIAD...). The highest sensitivity has been achieved by the **DAMA** collaboration. 100 kg of NaI(Tl) were operated for 7 years in the deep underground Gran Sasso laboratory, for a total exposure of 107000 kg day. The DAMA group observed an annual modulation in their count rate (see figure 1.8), which they claim to be compatible in phase and amplitude with a signal from WIMPs of ~ 52 GeV mass and a spin-independent WIMP-nucleon cross section of 7.2×10^{-42} cm^2 [Ber04a]. The DAMA experiment was upgraded in 2002. The second phase of this experiment is named LIBRA and is now running with 250 kg of NaI crystals.
The UKDMC group is using liquid xenon scintillator detectors. The ZEPLIN-I detector, located in the Boulby mine in the UK, consists of a 4 kg prototype tank. Three photomultiplier tubes are used in order to reject background by requiring triple coincidences.

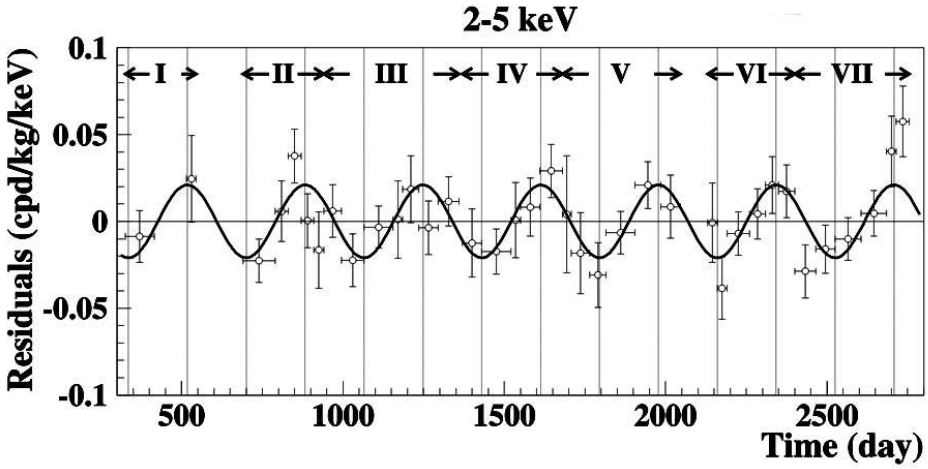

Figure 1.8: Annual modulation of the count rate in the energy region 2-5 keV as observed by the DAMA collaboration over a period of seven years [Ber04a].

The CRESST Phase I experiment was using sapphire cryogenic detectors and, as will be discussed later, gave the best sensitivity for low WIMP masses with spin-dependent interaction. However, due to the non-discriminating technique, it was limited by the background [Ang02].

Discriminating experiments

The experiments which use event by event discriminating techniques include a number of cryogenic experiments such as CDMS, EDELWEISS, ZEPLIN-II(III) and CRESST-II.
The **CDMS-II** experiment, in the Soudan mine, operates germanium and silicon cryogenic detectors with both superconducting thin films and NTD[8] Ge thermistors as temperature sensors [Abr02]. Additionally, ionization charges are drifted to thin film electrodes on the crystal surface and provide efficient electron recoil discrimination. At present, this experiment gives the most sensitive limit of all Dark Matter searches (see figure 1.9) [Col04b].
The **EDELWEISS** experiment, in the Modane underground laboratory, has operated three 320 g germanium bolometers measuring heat and ionization. Currently the experiment is in the preparation for its second phase.
Figure 1.9 displays the current exclusion limits as they appear in the most recent published papers. Both the CDMS and the EDELWEISS collaboration claim exclusion of the DAMA candidate at $> 99.8\,\%$ confidence level. Recent publications have shown that this exclusion also resists to all realistic variations of the halo parameters [Cop03], [Kur04].

[8] neutron transmutation doping

A number of experiments using liquid xenon are being proposed (like ZEPLIN-II(III), XMASS, XENON...) aiming at the discrimination on an event by event basis by using pulse shape discrimination of electron and nuclear recoil signals [Har02] [Apr04].
The next generation experiments, like EDELWEISS-II, CDMS-II, CRESST-II, ZEPLIN-III, are aiming for an improvement of about 2 orders of magnitude, down to $10^{-44}\,\mathrm{cm}^2$ (see figure 1.9) which would allow to test a much more significant part of the parameters space. This will require an increased detector mass, further background rejection, lower energy thresholds and overall improved discrimination. Special care has to be taken to keep background rate at low enough levels so that the mass increase can be fully exploited. It is already evident that both experimental issues and data analysis will be very challenging. Combining results from different target materials, measuring different signatures, such as the directionality of interactions, may prove to be the only way to ever ascertain the existence of WIMPs with reasonable confidence.

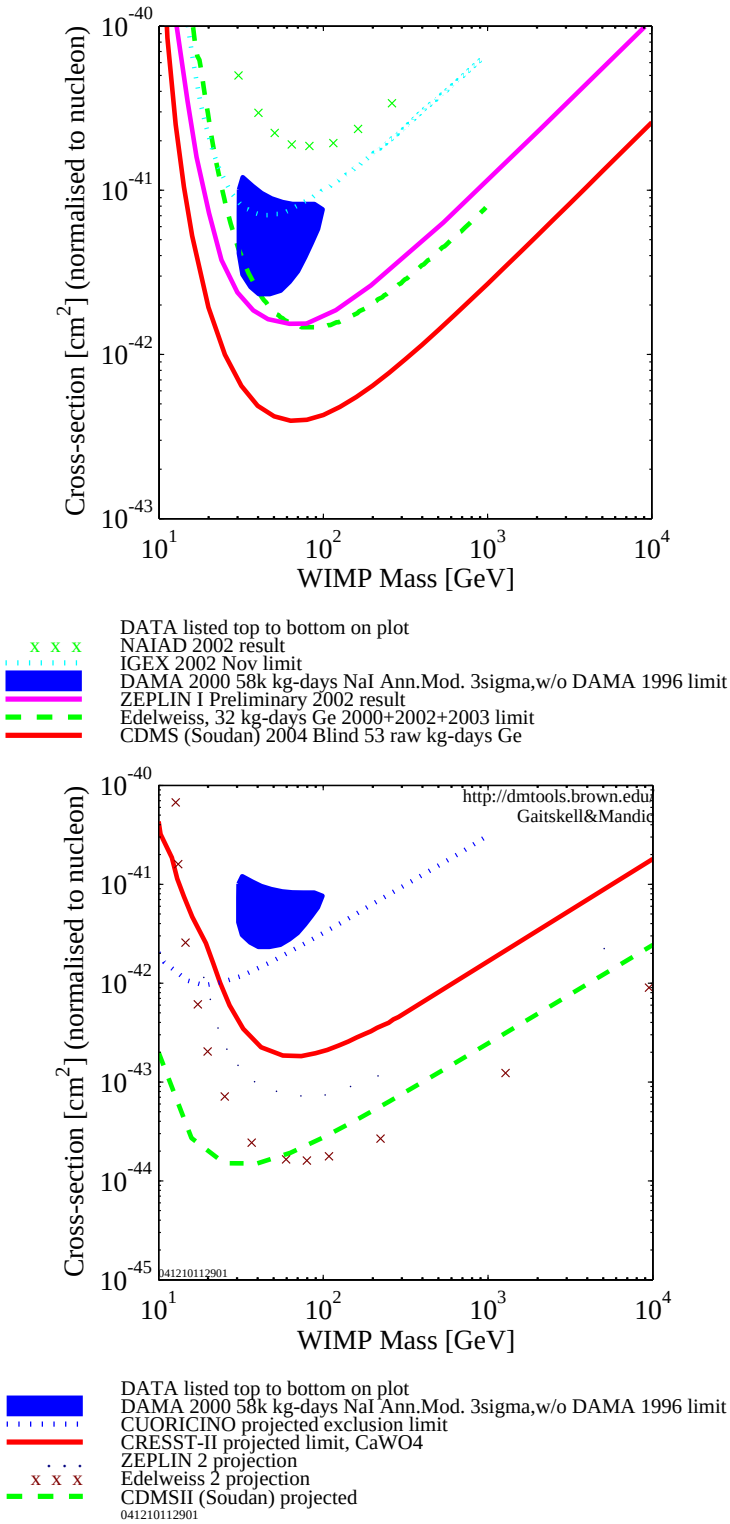

Figure 1.9: WIMP mass - cross section upper limits by several leading experiments (upper), and projected sensitivity of some of the next generation experiments (lower). The regions above the curves are excluded and a filled region indicates the DAMA evidence. Figure taken from [Gai].

Chapter 2

The CRESST Dark Matter search

The aim of CRESST is the search for WIMP Dark Matter particles via their elastic scattering off the target nuclei in an absorber, sapphire crystals in CRESST Phase I and $CaWO_4$ crystals for CRESST Phase II. As discussed in the previous chapter, due to the small cross section event rates are expected to be less than one per day and per kg of detector mass. It is therefore of crucial importance to suppress signals due to radioactivity which would hide or mimic WIMP signals. In this chapter, the characterization of the CRESST experimental setup and the basic principles of cryogenic detectors as well as the final results and limitations of the first phase of the experiment are presented. Finally, the idea of background discrimination by simultaneous measurements of phonons and scintillation light employed in CRESST Phase II is described.

2.1 The CRESST experimental set-up

2.1.1 Gran Sasso laboratory

The CRESST experiment is situated at the Laboratori Nazionali del Gran Sasso in Assergi, Italy. The laboratory is located in the highway tunnel of the Gran Sasso mountain at an average depth of 3.5×10^5 g·cm^{-2} of standard rock [1]. The location under the mountain provides an efficient shielding against cosmic rays, but due to the presence of natural radionuclides in the rock it is itself a source of radioactivity. Due to its mean thickness of $\sim$ 3700 m.w.e the flux of the most penetrating component of the cosmic rays, muons, is reduced by a factor of $\sim 10^{-6}$ to 1 m^{-2}h^{-1} (see figure 1.6). The Gran Sasso rock has an average density of 2.71$\pm$0.05 g cm^{-3} and is mainly calcareous but also elements such

[1] homogeneous material with Z=11 and A=22

Table 2.1: Gamma activity of samples of rock from different halls of Gran Sasso underground laboratory [Arp92].

Sample from	**Activity** [Bq / kg]			
	^{232}Th	^{238}U	^{40}K	^{214}Bi
Hall A Rock	8.8±0.3	84.7±8.4	224±6	41.9±0.6
Hall B Rock	0.25±0.08	5.2±1.3	5.1±1.3	4.2±0.3
Hall C Rock	0.27±0.10	8.2±1.7	2.9±1.4	5.1±0.2

as aluminium, magnesium and organic sediments are present. The activity of samples of rock coming from the different laboratory halls has been measured and the results are reported in table 2.1. It is rather low in Hall C and B while there is a higher activity in Hall A. This is due to a different composition of the rock. The integral gamma flux calculated for all natural chains is $\sim 1\ \gamma\text{cm}^{-2}\cdot\text{s}^{-1}$ [Arp92]. The activity due to ^{222}Rn with the present ventilation system and monitored near Hall C is about 30 Bq·m^{-3}.
The neutron flux in the Gran Sasso halls has been measured by different groups with different techniques as reported in table 2.2. The integral flux calculated for energies above 1 MeV is in the order of $10^{-6}\text{cm}^{-2}\text{s}^{-1}$. The flux is dominated by neutrons produced in the concrete layer and therefore does not vary much from hall to hall. The neutron flux present in the CRESST set-up comes from

Table 2.2: Neutron fluxes measured in the given energy intervals.
in Hall A: with BF_3 counters [Bel85].
in Hall C: with proton recoil scintillators in energy range > 1 MeV [Arn99].

Hall A		***Hall C***	
Energy interval (MeV)	Neutron flux ($10^{-6}\text{cm}^{-2}\text{s}^{-1}$)	Energy interval (MeV)	Neutron flux ($10^{-6}\text{cm}^{-2}\text{s}^{-1}$)
$< 50 \times 10^{-9}$	1.07 ± 0.05		
$50 \times 10^{-9} \div 10^{-3}$	1.99 ± 0.05		
$10^{-3} \div 2.5$	0.53 ± 0.008	$1 \div 2.5$	0.14 ± 0.12
$2.5 \div 5$	0.18 ± 0.04	$2.5 \div 5$	0.13 ± 0.04
$5 \div 10$	0.04 ± 0.01	$5 \div 10$	0.15 ± 0.04
$10 \div 15$	$(0.7 \pm 0.2)10^{-3}$	$10 \div 15$	$(0.4 \pm 0.4)10^{-3}$
$15 \div 20$	$(0.1 \pm 0.3)10^{-6}$		

different sources:

- Low energy neutrons induced by fission and (α,n) reactions due to uranium and thorium activities in the surrounding rock and concrete.
- Low energy neutrons induced by fission in the shielding material and the setup.
- High energy neutrons induced by muon interactions in the rock. These neutrons could do spallation reactions in the experimental shielding and produce additional neutrons.
- High energy neutrons induced by muon interactions in the shielding material (especially lead).

A simulation of the different contributions and the influence of different shielding materials has been done. It has been shown that the neutron flux, in the relevant energy range, in the hall is actually depending on the humidity of the concrete layer in the laboratory: the flux is higher when the concrete is dry compared to when it is wet [Wul04b]. Conservative estimates, using dry concrete, of the recoil spectra induced by neutrons of different origins in a $CaWO_4$ detector are presented in figure 2.1 [Wul04a].
The CRESST experiment is housed in the three-story building (Fig. 2.2) now located in Hall A. The first phase was realized in the Hall B. Clean conditions,

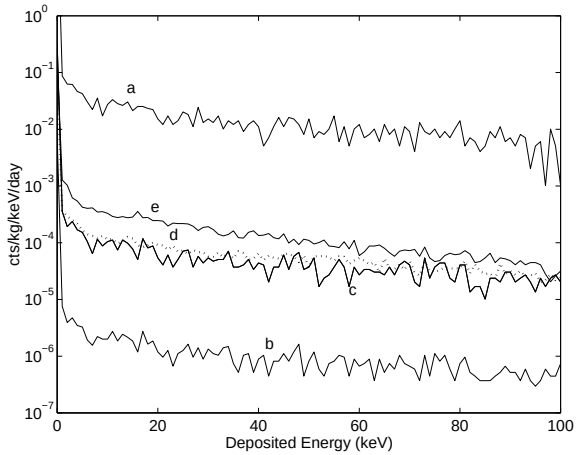

Figure 2.1: Simulated recoil spectra in a $CaWO_4$ detector induced by neutrons of different origins: (a) low energy neutrons from the rock/concrete, no neutron moderator, (b) low energy neutrons from the rock/concrete after being moderated by 50cm polyethylene, (c) low energy neutrons from fission reactions of 0.1 ppb ^{238}U in the lead shield, (d) high energy neutrons induced by muons in the rock and (e) high energy neutrons induced by muons in the experimental setup. (Figure from [Wul04a]).

while mounting the detectors, are provided in a class 100 clean room, placed at the ground floor. The cryostat is housed at the ground floor and is accessible from the second floor so that the maintenance can be done without entering the clean room. A Faraday cage extending over the first two floors encloses the clean room and the top plate of the cryostat to eliminate external electromagnetic interferences. The gas handling and pumping system necessary for the cryostat as well as the data taking system are placed outside the Faraday cage. On the third floor the computing room for on-line control of the experiment as well as a chemistry laboratory and a laminar flow area are located. The flow area is a room with a laminar ventilation in which detectors are prepared before being mounted in the cryostat.

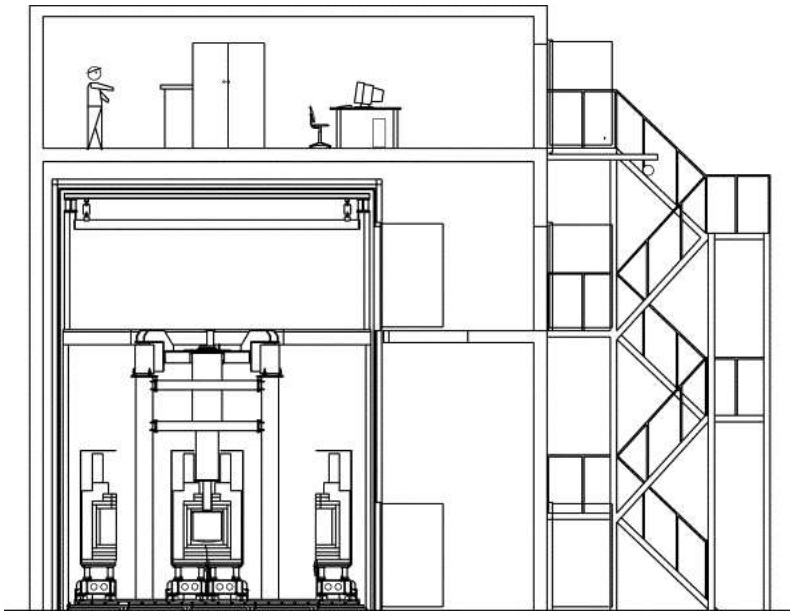

Figure 2.2: Schematic view of CRESST hut

2.1.2 Cryostat

The CRESST cryostat has been specially designed with a low background cold - box housing for the detectors well separated from a commercial ^{3}He/^{4}He dilution refrigerator (Oxford instruments). The cooling power of the cryostat is then transferred to the detectors via a 1.5 meter copper cold finger (for details see [Büh96]). The cold - box, shown in Fig. 2.3 consists of five radiation shields of copper which surround the experimental volume and the cold finger: a room temperature vacuum can; a liquid nitrogen (77K) thermal shield; a liquid helium (4K) shield; 600 mK and finally 80 mK inner radiation shield. The cold finger is connected to the mixing chamber and reaches at its bottom a base temperature

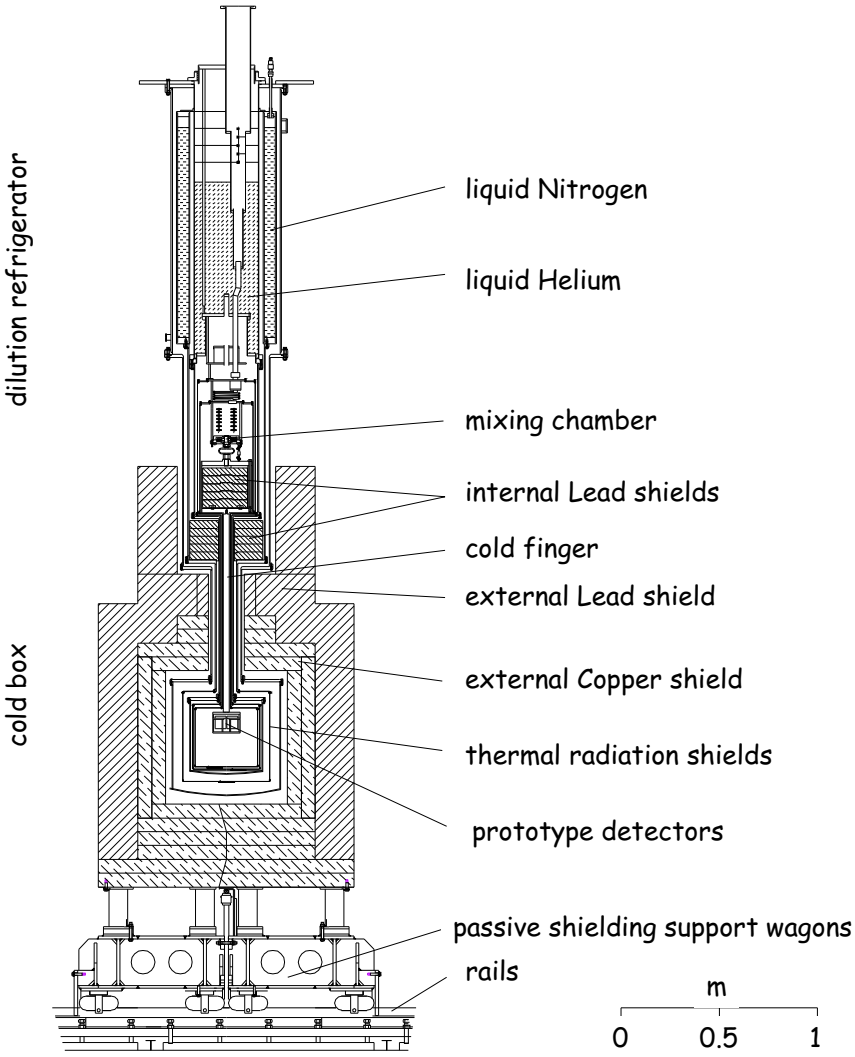

Figure 2.3: Schematic view of the CRESST cryostat and its passive shielding

of about 5 mK. Very radio-pure copper (NOSV[2]) is used for the cold finger and the shields. Finally, low-radioactivity lead is used for the vacuum seals instead of usual indium which contains radioactive ^{115}In with 96% isotopic abundance. The cryostat is hanging from a wooden plate which rests on air dampers to reduce interferences from vibrations.

2.1.3 The passive shielding

Figure 2.3 shows a schematic view of the cryostat and the passive shielding. In the upper part the dewars for liquid helium and nitrogen are shown. A lead

[2]High purity copper (99.99% Cu) with a electrical conductivity of $58.6\,\mathrm{m}/\,\Omega\,\mathrm{mm}^2$.

shield rests in between the dilution refrigerator and the cold box. The copper shielding is placed between the lead and the cold-box.
Lead is a high Z material and it has a high cross section for photo-electric absorption and muon capture compared to the lighter elements. Its low cross-section for neutron capture reduces the level of radio-isotopes which may be activated cosmogenically. It is therefore a highly effective material for γ shielding. On the other hand, due to the photo-electric absorption, Pb K-shell X-rays with energies of 72.8, 75.0, 89.4 and 84.7 keV may be emitted. Additionally, it is a difficult procedure (and hence very expensive) to produce lead with a low ^{210}Pb concentration. Its β decay with a lifetime of 22.3 years and 63.5 keV transition energy is followed by a β decay of ^{210}Bi to ^{210}Po with a half life of 5.013 days and a transition energy of 1162.7 keV. This chain ends with an α decay of ^{210}Po to ^{206}Pb with a lifetime of 138.376 days and a transition energy of 5407.46 keV [Ale98]. ^{210}Bi energetic beta particles contribute to the background by inducing Bremsstrahlung radiation and characteristic lead X-rays.
An inner layer of very radio-pure material is then added inside the lead shield, to absorb this radiation. This layer is usually made of very pure lead or copper. Despite of the lower Z copper has the advantage that it can be produced with a high purity level [Heu95]. As copper has a considerable neutron capture cross-section it is necessary to store it underground immediately after it is produced.
The CRESST shielding is composed of 14 cm of radio-pure copper directly enclosing the cold-box, followed by 20 cm of Boliden lead with a ^{210}Pb content of 35 Bq/kg and a total mass of 24 tons. To block the line of sight of the detectors to the upper part of the cryostat, Plombum lead with a ^{210}Pb content of 3.6 Bq/kg is used. Finally, the entire shielding is enclosed in an air-tight aluminium container which is constantly flushed with N_2 gas at a slight overpressure in order to prevent radon from penetrating the shielding.
The 50 cm polyethylene neutron moderator together with the muon veto will be installed outside the radon box for the final setup of the CRESST Phase II.

2.2 The CRESST detectors

The most crucial part of the detector module for the CRESST experiment is a superconducting thermometer. Cryogenic detectors have a low energy threshold and an excellent energy resolution. Additionally, cryogenic detectors detect almost the full energy deposition independent of the type of interaction. This combination gives a very low energy threshold for the detection of nuclear recoils that would result from WIMP interactions. The main limitation, as described above, comes from the residual radioactive background. Therefore, a dramatic improvement in sensitivity can be expected if the detector can discriminate between electron recoils (α, β, γ events) and nuclear recoils (WIMP and neutron events). Furthermore, a discrimination between the signals coming from WIMPs

and the ones from neutrons would give additionally a significant rise in sensitivity.
A general description of cryogenic detectors is given below, as well as a more detailed description of the components of the CRESST detection system.

2.2.1 Basic principles of cryogenic detectors

The low temperature detector consists of three basic parts: an absorber, a thermometer and a coupling to the heat sink (Fig. 2.4). An interaction in the absorber deposits an energy $\triangle E$ and leads to a temperature rise $\triangle T$ measured by the thermometer. The energy flows out of the system via the thermal coupling to the heat sink and the system relaxes back to the equilibrium state. In a very simplified model of the calorimeter, the relation

$$\triangle T = \frac{\triangle E}{C}, \tag{2.1}$$

holds, where C is the heat capacity of the absorber.

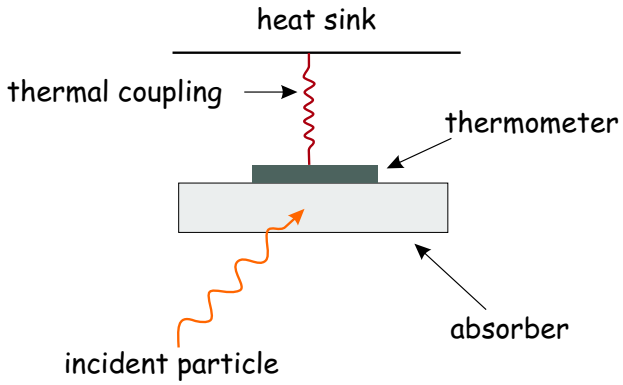

Figure 2.4: Schematic view of calorimetric detector

In dielectric materials the heat capacity at low temperatures is dominated by the phonon system for which $C \sim (T/\Theta_D)^3$, where Θ_D is the Debye temperature. At mK temperatures this T^3 dependance renders the heat capacity of the absorber very small and results in a measurable rise of the temperature following a particle interaction. In this simplified model, the temperature rise instantaneously follows the energy deposition. The system then relaxes back exponentially to its equilibrium temperature via the thermal link to the heat sink that is kept at a constant temperature. The relaxation time is

$$\tau = \frac{C}{G}, \tag{2.2}$$

where G is the thermal coupling strength to the heath bath. In reality, this model is not sufficient to describe the behavior of the detectors. The rise time is not infinitely fast and the decay is usually not a simple exponential. A detailed description of a theoretical model for the signal evolution for low temperature calorimeters is given in [Prö95]. The interaction in the absorber produces high frequency phonons. They do not thermalize in the absorber but, after being reflected many times at the free crystal surface, are finally absorbed by the free electrons in the thermometer. At mK temperatures the thermometer is practically thermally decoupled from the absorber due to the weakness of the electron phonon thermal coupling $\propto T^5$ in the thermometer. Therefore, only the thermometer is heated up by the interaction.

2.2.2 The absorber

The absorber of a detector for a low event rate experiment such as CRESST must satisfy several criteria. The most important criterion is that the material used for its production contains the minimal amounts of radioactive impurities. Another important property of the absorber is the melting temperature of the material. The thermometers which are detecting signals are tungsten (W) films that are evaporated on to the absorber. Since, evaporation takes place at $\sim 500°C$ the melting point of the absorber should be high enough to prevent inter - diffusion with the tungsten film.
CRESST Phase I employed sapphire crystals as absorber. This material has a high Debye temperature (θ_D=1040.8K) and a high melting point (T_{melt}=2310K) and hence allows to make very sensitive detectors with a low energy threshold. Sapphire (Al_2O_3) contains only stable isotopes ^{16}O (99.76% isotopic abundance), ^{17}O (0.04%), ^{18}O (0.2%) for the oxygen and 100% ^{27}Al for the aluminium.
CRESST Phase II uses a scintillating crystal ($CaWO_4$) as absorber. In this case, a small amount of the deposited energy is converted into scintillation light. Since, nuclear recoil events release less light than electron interactions one can identify the type of interaction via operating a cryogenic detector in coincidence with a light detector. Examination of the properties of this absorber and their optimization for the CRESST Phase II experiment are one of the main goals of the work presented in this thesis.

2.2.3 The thermometer

The temperature rise which follows an energy deposition in the absorber is measured via a **S**uperconducting **P**hase-Transition **T**hermometer (**SPT**). CRESST SPTs are thin superconducting tungsten films evaporated onto the surface of the absorber. Typical dimensions are: a thickness of 0.5÷2 kÅ and an area of about 50 mm^2. As illustrated in Fig. 2.5, within the transition of tungsten from normal

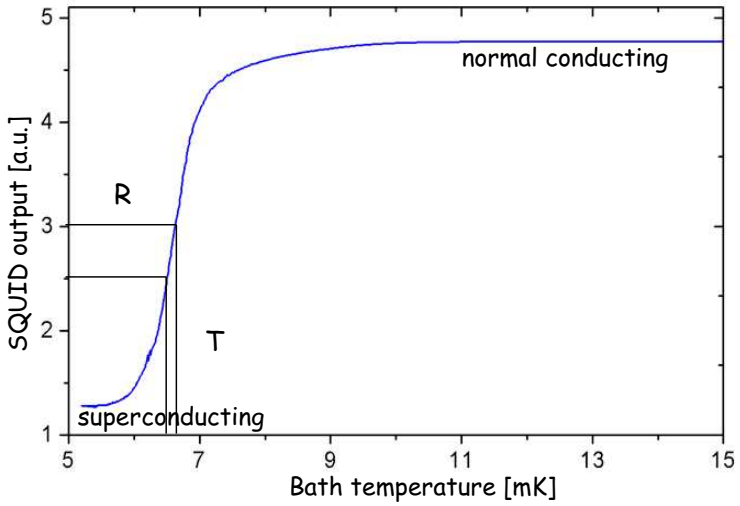

Figure 2.5: Typical measured transition curve of a tungsten film.

to the superconducting phase a small rise in temperature results in a relatively large rise in resistance and can be exploited to make an extremely sensitive thermometer. Typical transition widths[3] are ∼1 mK while the detector is stabilized within a few μK. Since the detector performance depends on the shape of the transition curve at the operating point it can vary significantly between different films. The width of the transition defines the dynamic range while the slope of the curve gives the sensitivity - the steeper the curve the more sensitive is the detector to a small energy deposition. The sensitivity also depends on the read-out current (see section 2.3): for high currents the sensitivity increases but this effect is limited by critical current and self heating effects in the film.
The heat capacity of the thermometer is a crucial parameter for CRESST detectors which are mostly sensitive to non-thermal phonons and can be optimized by changing area and thickness of the film. Optimization of the thermometers is not the main topic of this thesis and here only the final solutions for detectors will be presented. Details can be found elsewhere [Pet05].

2.3 The readout system

The resistance change of a low impedance phase transition thermometer is measured via a SQUID readout scheme. As illustrated in Fig. 2.6, a constant current

[3]For higher current, transition curve broadens due to a critical current effect. The typical width of 1 mK applies only for low currents (≤ 1 μA).

I_0 branches between the tungsten thermometer and a shunt resistor in series with the input coil of the SQUID. For the CRESST experiment a 50 mΩ shunt resistor is used and a typical normal conductivity resistance of the thermometer is $\sim 300\,\mathrm{m\Omega}$. The current through the SQUID branch is given by

$$I_s = I_0 \frac{R_f(T)}{R_f(T) + R_s}\,, \tag{2.3}$$

where
I_s - steady current through the input coil,
I_0 - total current applied,
R_f - film resistance,
R_s - shunt resistance.

Any change in resistance R_f will cause a change of the branching of the applied constant current I_0. Thus, the increase of the current I_s due to an increase of R_f resulting from an energy deposition, changes the magnetic flux coupled to the SQUID by the input coil. SQUIDS are devices which are very sensitive to any

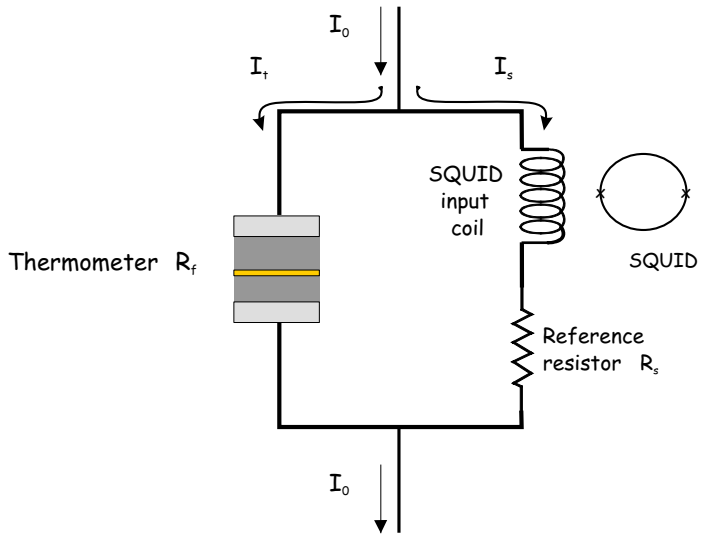

Figure 2.6: Readout circuit (see text).

change of magnetic flux penetrating their input loop: the input coil transforms the current into a magnetic flux Φ and this flux is then coupled into a SQUID loop (superconducting ring with two Josephson junctions).
The SQUIDs used for CRESST are commercially available DC-SQUIDs which are mounted in the liquid He bath. The shunt resistors are thermally coupled to the mixing chamber to reduce the Johnson noise and electrical connections from SQUIDs to the detectors are twisted pairs of superconducting wires.

The absorbers rest thermally insulated in their copper housing which are thermally and electrically insulated from the copper base plate inside of the cold-box. Each holder is thermally coupled to the mixing chamber (through the base plate of the holding system) via a copper wire to have a relaxation time of a few hundred seconds. This design acts as a low pass filter for temperature fluctuations of the mixing chamber. Detector holder is serving as the heat bath temperature reference for each detector. Thermal contact between the detector and the

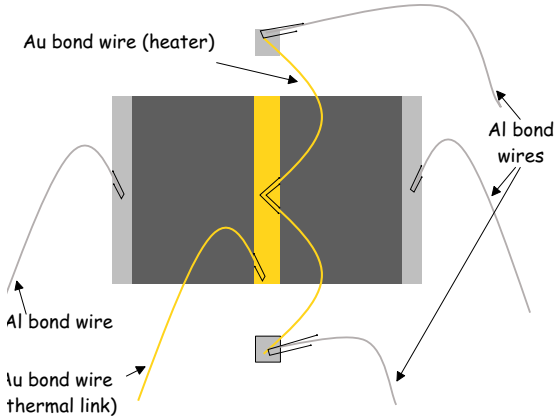

Figure 2.7: Connection scheme of the W-SPT. Al bond wires are used for electrical contacts. Au bond wire is used for the thermal link.

holder is provided by 20 μm Au wires bonded between the thermometer and the copper holder (see Fig. 2.7). Superconducting Al wires are connecting the thermometer to the external readout circuit. Screwed contacts are used instead of common solder joints to avoid usage of radioactive solder tin. Finally, Au wire bonded between small contact pads (in figure 2.7 the little squares next to the thermometer) and the Au pad in the center of the thermometer serve as a heater to control the temperature of the detector and to inject the electrical heater test pulses. External connection with a heater module to the two small Al pads are used to apply a controlled voltage across the gold wire. Test pulses are generated by a commercial tail pulse generator.
The gold bond wire that is establishing the thermal connection works also as a ground connection of the readout circuit. The SQUID output signal leaves the Faraday cage through a 50 kHz low-pass fed through filter and is split into a trigger signal and the signal itself. For every triggered event the transient digitizer data is written to disk for off-line analysis.
Voltage signals from the data acquisition system to control the operating temperature of each detector are fed through filters into the Faraday cage. The control system is decoupled from the ground of the acquisition system via differential amplifiers.

2.4 Detector operation

Normal operation of the cryogenic detectors starts with a recording of the transition curves. As mentioned in Chap. 2.2.3 the performance of the detector depends to a large extent on the shape of the transition curve. Once the operating points have been chosen, each detector needs to be stabilized at this point independently. In order to achieve long term stability and a full understanding of the detector performance one needs to know the detector response function at any time. Therefore, heater pulses with a shape adjusted to create pulses similar to those of a particle interaction are sent at regular time intervals. Besides monitoring the stability and the energy calibration, heater pulses provide a measure of the trigger efficiency close to the threshold of each detector. A higher number of heater test pulses is injected near the detector threshold. They are used for characterization of the trigger efficiency and a determination of the off-line threshold since the sensitivity of a detector to low mass WIMPs strongly depends on the achieved threshold (see Chap. 1.4.3). Normal operation proceeds to the calibration run where commonly a ^{57}Co source is used. ^{57}Co has a half life of 270.9 days and decays by electron capture to the stable isotope ^{57}Fe. Its decay is characterized by several γ lines of which only 122 keV (85.6% branching ratio) and 136 keV (10.68%) can penetrate the cold box. A source is inserted via a removable plug in a channel machined through the bottom of the passive shielding. This way the source can be inserted at any time without opening of the shielding or disturbing in any sense the setup. Together with the source, the heater pulses are then used to determine the detector response curve over the whole dynamic range (for details see [Coz03]). Once the response function is known, the energy of any particle pulse can be determined. In a Dark Matter run the calibration with a source is always done after all operating conditions have been settled. Heat pulses are always injected, both with and without source, during the whole run. Any time a slight change is implemented a new calibration is carried out. Usually, the calibration is repeated at the end of the run to confirm the stability of detector operation.

2.5 Basic elements of data analysis

The data analysis for the CRESST experiment is performed off-line. Pulses exceeding a given threshold amplitude, are digitized and recorded on disk. When more than one detector is operated, pulses occurring within half of the post trigger region of the first acquired pulse are also recorded, together with a delay information. A method to correctly evaluate the pulse height of the recorded pulses, which takes into account the nonlinear detector response has been developed for the CRESST Phase I [Coz03]. The method used to analyze the CRESST Phase I results relies exclusively on pulse shape discrimination (PSD)

and removal of coincident events. The procedure elaborated for the sapphire detectors makes use of "template fits". In general, this technique consists of selecting a set of pulses, for example from a calibration source, which are then averaged. The baseline is then subtracted and the averaged signal is divided by its amplitude to arrive at the template for fitting all measured pulses. This method gives not only a pulse height information but also the onset channel and a mean square deviation. For each fitted pulse the deviation of its shape to that of the template is calculated and the value of the square root of the mean squared deviation, the RMS value, is obtained. To extract Dark Matter limits a very conservative approach has been adopted: both a software threshold and a RMS cut have been applied such that the retention efficiency was 100% over the whole range.

2.6 CRESST Phase I

The detectors employed in the CRESST Phase I used 262 g sapphire (Al_2O_3) absorbers and tungsten (W) thermometers operating near 15 mK. Due to the optimized design, and because of non-thermalization of the phonons, with a use of active thermal feedback, an energy resolution of 133 eV (FWHM) has been achieved for 1.5 keV X-rays [Mei00].

2.6.1 Limitations of the CRESST Phase I

The detectors used were four sapphire crystals arranged on a square array equally spaced 15 mm apart. Each crystal had a mass of 262 g and measured $40\times40\times41$ mm^3. CRESST Phase I upper limits for the WIMP scattering cross section as a function of a WIMP mass have been obtained by comparing the measured spectrum with a theoretical event rate. The details for the calculation of the expected WIMP scattering recoil spectrum are given in [Ang02] where an isolated WIMP halo model has been assumed using a truncated Maxwell velocity distribution. To compare the results to those of experiments using other target nuclei the resulting WIMP-nucleus cross section have been converted into a WIMP-proton cross section.

In Fig. 2.8 the obtained 90% CL upper limits on the cross section for the spin-dependent WIMP interaction on Al are shown. As a comparison, equivalent WIMP-proton cross section limits of EDELWEISS, DAMA, and UKDMC experiment are given. As can be observed, the CRESST limit improves existing results for low-mass WIMPs. In fact the very low energy threshold of 600 eV achieved in CRESST Phase I enabled us to explore WIMP masses down to 1 GeV. While for the spin-dependent interaction the only contribution comes from ^{27}Al nuclei which have spin 5/2 and a 100% isotopic abundance for spin-independent

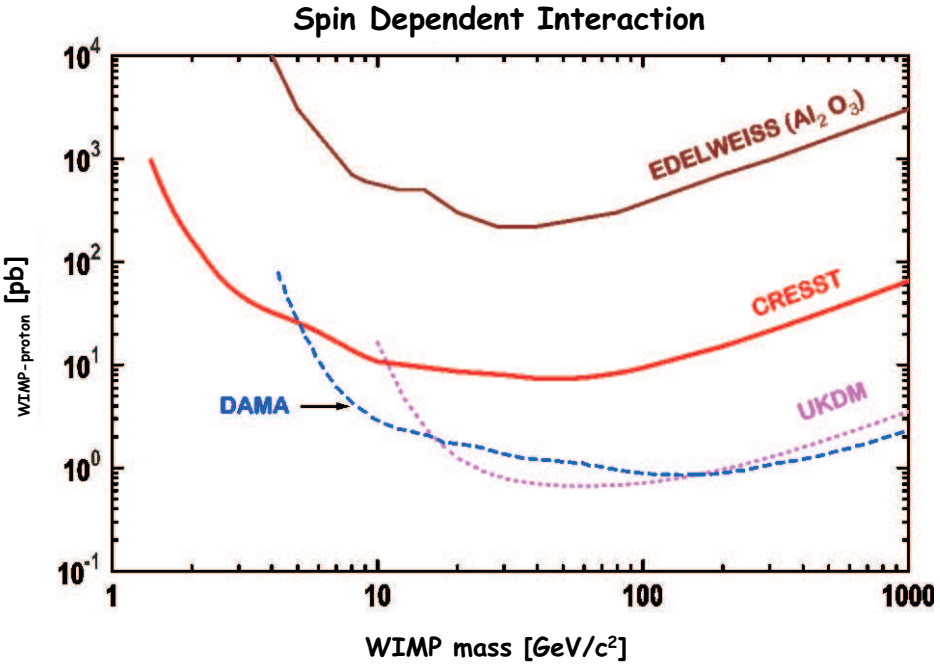

Figure 2.8: Equivalent WIMP-proton cross section limits for a spin-dependent interaction as a function of WIMP mass. For comparison also limits of EDELWEISS, DAMA and UKDMC experiments are shown [Ang02].

interaction both Al and O nuclei contribute. Even thought, due to the A^2 dependence of the cross section (section 1.4.1) the spin-independent channel is disfavored for a target with light nuclei, as sapphire. CRESST Phase I, as shown in Fig. 2.9, improved existing limits for WIMP masses below 5 GeV due to its low energy threshold.

Passive techniques of background reduction - deep underground site, efficient shielding against environmental radioactivity and the use of radio pure materials inside the shielding - is of course imperative in WIMP Dark Matter searches. However, there is a remaining background dominated by β and γ emissions from sources inside the shielding which limits the sensitivity of the search. As β and γ interactions produce electron recoils and WIMPs and neutrons nuclear recoils, dramatic improvement in sensitivity can be achieved if one could distinguish between electron and nuclear recoils. Additionally, if one chooses an absorber with a large atomic number it gives a significant improvement in sensitivity in the spin-independent channel. This is the basic idea used in CRESST Phase II.

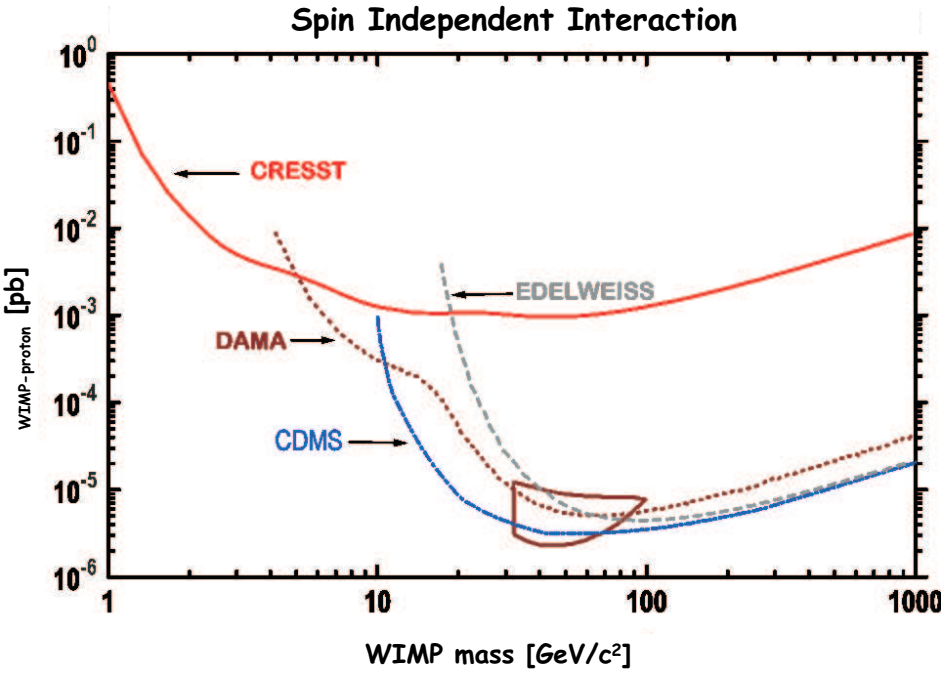

Figure 2.9: Equivalent WIMP-proton cross section limits, at 90% CL, for a spin-independent interaction as a function of WIMP mass. For comparison limits from EDELWEISS, CDMS, and DAMA experiments are shown [Ang02].

2.7 CRESST Phase II: Idea

The CRESST experiment in its second phase is employing a background rejection technique using the scintillating crystal as absorber and detecting the light signal simultaneously with the phonon signal. In this case, a particle interaction is exciting mainly phonons but a small fraction of the energy, typically $< 2\,\%$, is converted into light. Since nuclear recoils which result from WIMP or neutron interaction are producing less light than electron interactions one can identify the type of interaction by operating the phonon detector in coincidence with a light detector. This method allows an event by event discrimination of background and thereby improves the sensitivity of the Dark Matter search. A target material with a large atomic number A was chosen to profit from the A^2 dependence of the scattering cross section for WIMPs with spin-independent interaction. Combined with the strong background rejection this results in a considerably improved WIMP sensitivity compared to CRESST Phase I.
In addition to improving limits on Dark Matter, it is important to have means for the positive verification of a Dark Matter signal as well as for the elucidation of its nature. Once a Dark Matter signal is suspected, it can be verified by CRESST Phase II via the following effects:

1. Varying the mass of the target nucleus leads to a definite shift in the recoil energy spectrum and the observed rates.

2. An annual modulation of the spectral shape and rate can be used for the verification of Dark Matter signal.

3. Difference in the strength of the spin-dependent interaction, in case of different target materials, can be used as a source of information about the nature of Dark Matter particles.

Extensive studies of the scintillating properties of $CaWO_4$ have been performed in this work because they are critically entering the efficiency of the background suppression. The results will be presented in Chapter 5.
In this section the proof-of-principle experiment will be presented as well as some details about the detector module developed for the CRESST Phase II. Finally, the projected sensitivity of CRESST Phase II will be reported.

2.7.1 The proof-of-principle experiment

As a first step the light output of several different scintillating crystals (BGO ($Bi_4Ge_3O_{12}$), BaF_2, $PbWO_4$ and $CaWO_4$) was studied at milikelvin temperatures (see Table 2.3 [Meu99]).

Table 2.3: Equivalent energies of the light detected for the measured scintillators at a working temperatures of 12 mK [Meu99]

Crystal	Detected light energy [keV] for 5.5 MeV α	Detected light energy [eV] for 60 keV γ
$CaWO_4$	5.2	210
BGO	8.4	200
$PbWO_4$	1.9	$\cdots$
BaF_2	2.1	$\cdots$

$CaWO_4$ was chosen for CRESST Phase II due to its relatively high light output and in order to take advantage of the large scalar cross section due to the high value of A^2 of tungsten (as described in section 1.4.1). Another selection criterion was the radiopurity of the crystals. Depending on manufacturer $CaWO_4$ showed good radiopurity levels measured with germanium spectroscopy.
A first proof-of-principle detector module was made from a 6 g ($20\times10\times5mm^3$) $CaWO_4$ crystal and a small sapphire light detector[4]. The result is shown, as

[4]Small additional cryogenic calorimeter optimized for light detection

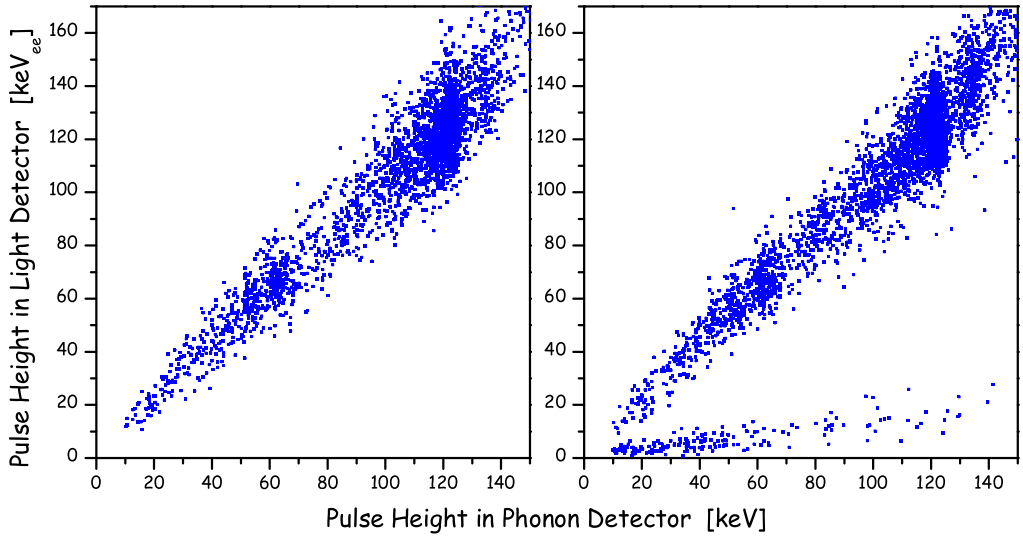

Figure 2.10: Scatter plot of the pulse height in the light detector vs. the pulse height in the phonon detector for the proof-of-principle module. The crystal was irradiated with 122 and 136 keV photons from ^{57}Co source together with ^{90}Sr β source (left picture) and then adding an Am-Be neutron source (right picture) [Meu99]. The pulse height in the light detector is converted to energy using the calibration of the phonon detector.

a scatter plot of the pulse height in the light detector versus the pulse height in the phonon detector, in Fig. 2.10. The phonon detector measures the total energy deposited in the absorber, independent of the interaction, while the light detector distinguishes electron and nuclear recoils. The measured quenching factor[5] is 7.4 for neutrons and 3.6 for alpha particles. A rejection factor of 98% was demonstrated down to 10 keV, allowing a clear separation of the electron from the nuclear recoil band down to 10 keV [Meu99].

2.7.2 Detector module

The detector module for CRESST Phase II is shown schematically in figure 2.11. Each module consists of a cylindrical $CaWO_4$ absorber crystal ($\varnothing = 40\,\mathrm{mm}$, $\mathrm{h} = 40\,\mathrm{mm}$) with a W-SPT deposited on one surface (phonon detector) and a silicon substrate (either $30 \times 30 \times 0.4\,\mathrm{mm}^3$ or $\varnothing = 40\,\mathrm{mm}^2$) again with a W-SPT deposited onto its surface (light detector). To minimize light losses the whole

[5]The quenching factor is defined as the ratio of light yield of electron interactions to light yield of nuclear recoils of the same energy.

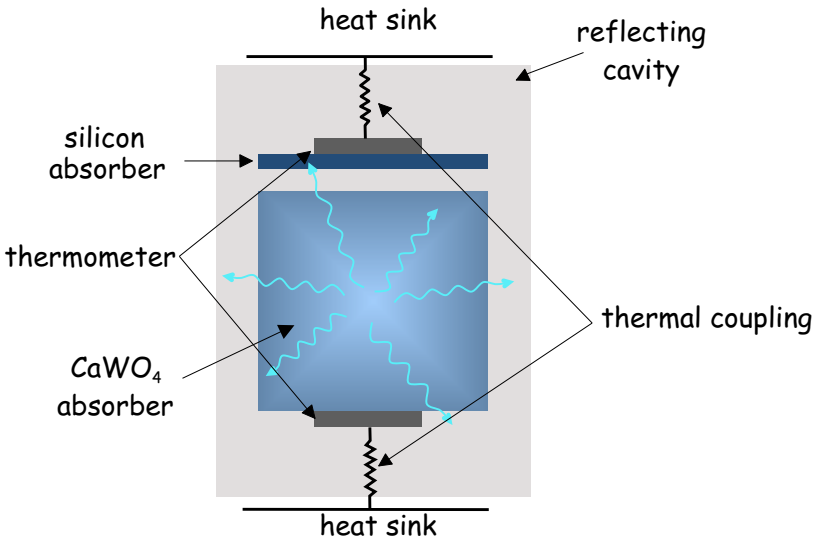

Figure 2.11: Schematic view of the CRESST Phase II detector arrangement.

module is enclosed in a reflector cavity.

Phonon detector

Compared to sapphire crystals, $CaWO_4$ has a few drawbacks. Tungsten films evaporated directly onto its surface showed transition temperatures at 40 - 50 mK. An intermediate diffusion barrier of SiO_2 between the crystal surface and the tungsten film had to be added to lower transition temperatures to $\simeq 7$ mK [Ang04]. Another drawback is the lower speed of sound. From the Debye temperature of $\theta_D = 228.4$ K [Glu73] one can estimate a factor of 4.2 smaller speed of sound than in sapphire. We have obtained good energy resolution: $\Delta E = 1$ keV for 46 keV γ-rays; $\Delta E = 13$ keV for 1.17 MeV $\gamma's$, and 100 % trigger efficiency for 2 keV heat pulses.

Light detector

As only a small portion of the energy is converted into light, a new design of light detector[6] was made to increase the sensitivity of the light detector (Fig. 2.12). Additionally, the thermal coupling of the light detectors to the heat bath, and thus the detector´s integration time had to be adjusted for the long decay time of the scintillator [Pet04]. We have obtained an energy resolution of about $2\,keV_{ee}$ at zero energy [7] [Pet05].

[6]The thermometer was equipped with a phonon collector to increase its sensitivity.

[7]Data from the ^{232}Th calibration were used to extract the energy dependence of the resolution. The resolution in the light channel was modelled by a power series for energies between

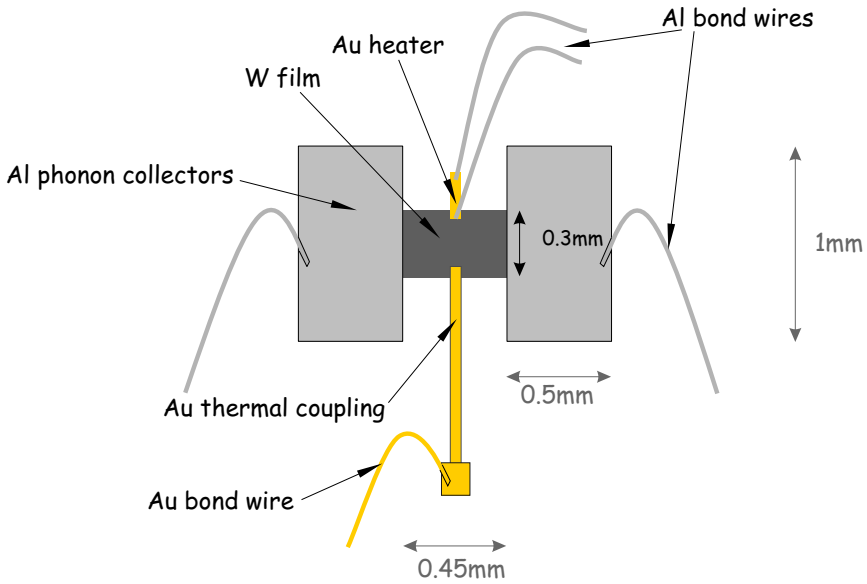

Figure 2.12: Schematic view of the light detector geometry. To increase the detector sensitivity the thermometer heat capacity can be reduced by decreasing its area. In a design where the thermometer alone provides the collecting area, the sensitivity gain is limited by the efficiency of the phonon collection process whose time constant is inversely proportional to the collecting area. To overcome this limit a very small tungsten thermometer is combined with a phonon collector film of moderate size made of a superconductor with a much higher transition temperature.

2.7.3 Projected sensitivity of CRESST Phase II

CRESST Phase II plans to operate 33 modules (using 66 SQUID read out channels) with a total absorber mass of $\sim$10 kg. A neutron moderator (50 cm polyethylene) and a muon veto will be added to the existing passive shielding. The projected sensitivity of CRESST Phase II for a 10 kg $CaWO_4$ detector and 3 years of operation is shown in Fig. 2.13.

zero and 300 keV. The electronic noise of the light detector and hence its energy resolution when extrapolated to zero energy is about 2 keV (FWHM) [Pet05].

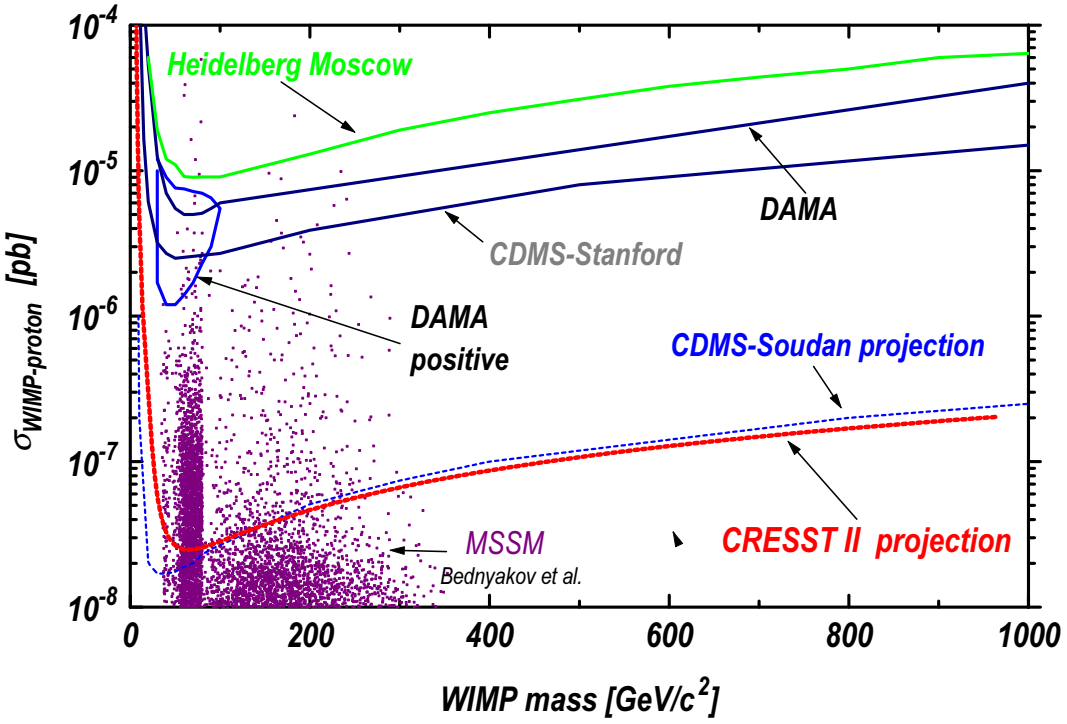

Figure 2.13: WIMP-nucleon cross section limits (90 % CL) for spin-independent interactions as a function of the WIMP mass, expected for a 10 kg $CaWO_4$ detector with a background rejection of 99.7 % above a threshold of 15 keV and 3 years of measurement time in the CRESST setup in Gran Sasso. For comparison the measured limit from the Heidelberg-Moscow ^{76}Ge experiment [Bau98], the DAMA NaI limits [Ber99] and contour for positive evidence [Ber00], the CDMS Stanford limit [Abu00] and the expectation for CDMS Soudan [Abr02] are also shown. The scatter plot shows the expectations for WIMP-neutralinos calculated in the MSSM framework (with non-universal scalar mass unification) [Bed97]. Picture taken form the proposal of the CRESST Phase II.

Chapter 3

The Scintillating $CaWO_4$ Crystals

As mentioned in the previous chapter, a combined detection of phonon and scintillation light will be used for background suppression in Phase II of the CRESST experiment. As the scintillation properties of the absorber define the separation threshold (see section 2.7.1) and are therefore limiting the experimental sensitivity, the scintillation properties of $CaWO_4$ crystals have been studied extensively in this work.
This chapter introduces the basics of the scintillation mechanism in inorganic scintillators, with emphasis on the properties of $CaWO_4$ crystals.

3.1 The basics processes

Luminescence phenomena i.e. the emission of light (visible or UV) following the absorption of energy in the material, are widely observed in nature. A luminescent material is also known as scintillator. Scintillation is used for the detection of various kinds of ionizing radiation. The scintillation process can be represented as a sequence of the following stages:

1. Absorption of the ionizing radiation and creation of primary electron-hole (e-h) pairs,
2. Relaxation of the primary excitations, i.e. production of numerous secondary electrons, holes, photons, plasmons and other electronic excitations,
3. Thermalization of the low-energy secondary electrons (holes) resulting in an energy spectrum limited by the band gap energy E_g,
4. Energy transfer from the electrons and holes (or e-h pairs) to the luminescence centers and their excitation,
5. Light emission from the luminescence centers.

3.2 Creation of the electron-hole pairs

3.2.1 Absorption of the incident radiation

The first stage of the scintillation process, the interaction of incident quanta or particles with matter and the creation of primary electronic excitations, is well studied. Therefore, only a brief look at some general considerations will be presented here. From the point of view of its interaction with matter and its absorbtion by a scintillator, radiation can be divided into three groups: (1) electromagnetic radiation, (2) charged particles and (3) neutral particles.

Electromagnetic radiation

Gamma quanta interact mainly with electrons. Electromagnetic radiation is absorbed or scattered in a single event. The intensity J_0 of a collimated beam of X-rays or gamma rays incident on an absorbing layer of thickness x, is reduced to the transmitted intensity J according to

$$J = J_0\, exp(-\mu x), \tag{3.1}$$

where μ is the linear absorption or attenuation coefficient of the material. The absorption coefficient depends on the electron density, n_e, and the absorption cross-section, σ, of an atom as

$$\mu = -\frac{dJ}{Jdx} = \frac{n_e\,\sigma}{Z}, \tag{3.2}$$

where Z is the atomic number of the material.
High energy photons interact with matter by three processes: photoelectric effect, Compton effect and pair ($e^+ e^-$) production. Correspondingly, the total cross-section, σ, can se divided into three parts

$$\sigma = \sigma_{ph} + \sigma_c + \sigma_{pp}\,. \tag{3.3}$$

Here σ_{ph} denotes a cross-section for the photoelectric effect, σ_c, for the Compton effect and σ_{pp} for pair production.
In the photoelectric effect, the photon is absorbed by an atom and subsequently an electron (photoelectron) of one of the shells is ejected. The photoelectric effect is possible only for bound electrons when a part of the photon momentum is passed to the atom. The probability decreases with photon energy, E_γ, and increases with the binding energy, E_b, and atomic number Z. The cross-section σ_{ph} is characterized by the following dependence on Z and E_γ

$$\sigma_{ph} \propto \frac{Z^5}{E_\gamma^{7/2}} \qquad for\ E_\gamma/E_b \geq 1, \tag{3.4}$$

$$\sigma_{ph} \propto \frac{Z^5}{E_\gamma} \qquad for\ E_\gamma/E_b \gg 1,$$

Thus, the photoelectric effect plays a leading role for heavy elements with large Z and γ-energies below $1.1\,MeV$.
In the Compton effect, the photon interacts with an atomic electron to which a part of the energy is transferred. The result is a Compton scattered photon with energy E'_γ and a Compton electron with the energy E_γ - E'_γ. This electron can produce a number of secondary electrons and finally scintillation. From the conservation of energy and momentum one can derive

$$E'_\gamma \;=\; \frac{E_\gamma}{1 \,+\, \dfrac{E_\gamma}{m_e\, c^{\,2}}\,(1 \,-\, cos\,\theta)}, \tag{3.5}$$

where θ is the angle between the direction of the original and the scattered photon, m_e the electron mass and c the velocity of light. The cross section of Compton scattering σ_c decreases with E_γ and increases with Z as

$$\sigma_c \;\propto\; \frac{Z}{E_\gamma}\,. \tag{3.6}$$

Compton effect plays a leading role for the medium energies and materials of low Z.
The electron-positron pair production becomes possible if the energy of the incident photons exceeds $2\,m_e\,c^2$. This process occurs mainly in the Coulomb field of the nucleus. Near the threshold the cross section of the pair production σ_{pp} is given by

$$\sigma_{pp} \;\propto\; Z^2\, ln2\, E_\gamma\,. \tag{3.7}$$

At very high energy of the incident photons ($5\,GeV$), the probability of pair production reaches the maximal value and does not grow further. The pair production process is the dominant process for high energy gammas.

Charged particles

A charged particle in its passage through matter dissipates its kinetic energy in a succession of inelastic collisions with the constituent electrons, resulting in excitation and ionization of atoms. The stopping power of matter is defined as the energy dE_{ion} lost by a charged particle within a length dx or as a specific energy loss dE_{ion}/dx. The main ionization losses of a particle with charge z, mass m and velocity v are determined by the well-known Bethe-Bloch formula

$$-\,\frac{dE_{ion}}{dx} \;=\; \frac{4\pi \cdot N_A\, z^2 \cdot e^4}{m\, v^{\,2}} \;\cdot\; \frac{Z}{A} \;\cdot\; \left[ln\left(\frac{2\,m\,v^{\,2}}{\overline{I}(1 \,-\, \beta^{\,2})}\right) \,-\, \beta^2 \right], \tag{3.8}$$

where $\beta = v/c$; x is the path length [in Mass/Area] of the particle in matter; Z and A are the atomic and mass number of the matter, respectively; N_A is the

Avogadro number and $\overline{I}$ is mean ionization potential of the matter. $\overline{I}$ is usually determined experimentally but $\overline{I} = 13.5\,\mathrm{Z}\,(\mathrm{eV})$ can be used for an estimate. From equation 3.8 it is clear that the energy loss of heavy charged particles (like protons and α particles) is z^2 times higher than the energy loss of an electron of the same velocity. Therefore, when solids are irradiated with heavy charged ions the complete ionized region of matter appears along their path and is defined as the track of a particle. Low energy electrons, protons, α particles and heavy ions are weakly penetrating particles. The light output of scintillators generally decreases with increasing ionization density.

Neutrons

Neutrons interact with the nuclei of the target material, by which they are either absorbed or scattered. The result may be a nuclear reaction, elastic and inelastic scattering. Here, only elastic scattering is considered. The cross section of the elastic scattering of a neutron, σ_n, at low energies is almost constant and can be expressed as

$$\sigma_n\,[cm^2] = 4\pi\,\left(1.4 \cdot 10^{-13}\,A^{1/3}\right)^2. \tag{3.9}$$

From the kinematics of the collision one gets the energy of the recoil nucleus as

$$E_r \;=\; \frac{4\,AE_n}{(A\,+\,1)^2}\,cos^{\,2}\alpha, \tag{3.10}$$

where α is the recoil angle in the laboratory system, and E_n the initial kinetic energy of the neutron. For head-on collision with $\alpha = 0$, the recoil nucleus receives the maximum energy

$$E_r \;=\; \frac{4\,A}{(A\,+\,1)^2}\,E_n \;\approx\; \frac{4}{A}\,E_n \qquad\qquad (for A \gg 1). \tag{3.11}$$

The recoil nucleus dissipates its kinetic energy in a succession of inelastic collisions with the constituent electrons, resulting in excitation and ionization of atoms and at very low energies in non-ionizing collisions with other nuclei.

3.2.2 Relaxation of the primary electrons and holes

X-rays or gamma quanta of intermediate energy interacting with a scintillator will be absorbed by the photoelectric effect producing a hole in an inner shell of an atom and a free or quasifree electron (primary hole/electron). The second stage of the scintillation process is more complicated and is strongly material dependent. The relaxation is accomplished differently for the hole and the electron. An atom with an ionized inner shell can relax either radiatively by emitting a photon, X-ray fluorescence or non-radiatively by generating a secondary electron (Auger

effect). The Auger electron can again loose its energy by scattering off electrons or emitting phonons. An incoming electron moving through a solid will ionize atoms causing an avalanche of electrons and holes until the resulting products are no longer able to cause further ionization.

3.2.3 Thermalization of the low-energy secondaries

As soon as the generated electrons (and photons) are unable to produce further ionization i.e. when their energy falls below the ionization threshold they start to produce phonons. The effect is known as electron-phonon relaxation or thermalization stage. In the process of thermalization the electrons move down to the bottom of the conduction band and the holes move to the top of the valence band.

3.3 Excitation and emission of luminescence centers

The fourth stage is called the migration stage as the electronic excitations migrate to transfer energy to the centers that are emitting light i.e. to the so-called luminescence centers. Electron-hole recombination at the luminescence center and excitonic types (excitonic mechanism) of energy transfer are possible. In the case of e-h type, the luminescence center is excited by a consecutive capture of electron (hole) and hole (electron). As the number of created low energy (valence) excitons[1] is small compared to the number of pairs of free electrons and holes, the excitonic mechanism of the energy transfer occurs less often. Energy losses in the migration stage depend on the spatial separation of electrons and holes relative to the luminescence centers. Various impurities and lattice defects play a role as electron and hole traps in inorganic crystals[2]. Many ionic crystals (as $CaWO_4$) exhibit an interesting phenomenon of localization of a valence hole in the regular lattice, known as self-trapping. In the process of thermalization a hole reaches the top of the valence band and binds to a distinct anion forming a Self Trapped Exciton (STE), a so-called V_k center. The excited STE can emit a photon and the resulting emission is called excitonic emission.
The final stage of the scintillation process is the emission of luminescence centers, which is well studied. Two general types of luminescence mechanisms are distinguished: intrinsic and extrinsic. The intrinsic luminescence is related to the emission of STEs. The extrinsic luminescence is a result of electronic transitions of an activator ion (like Tl in NaI:Tl).

[1] Bound electron-hole pair

[2] For example anion vacancies in ionic crystals act as effective capture centers for electrons.

3.4 The scintillation process in $CaWO_4$

The intrinsic luminescence in $CaWO_4$ crystals arises from the annihilation of self-trapped excitons (STE), which form excited WO_4^{2-} complexes. Two main types of intrinsic electronic excitations can be distinguished in $CaWO_4$ crystals: one is the transfer of an electron from the oxygen to the tungsten ion, the other is the transfer of an electron from the oxygen to the Ca^{2+} ion. Electronic excitations of the first type can be considered as various excited states of an oxyanion[3] [Gra75]. The electronic excitation of the second type is analogous to the direct transition in CaO [Lus94] and has a transition energy of 7 eV (180 nm). In $CaWO_4$ crystals the main intrinsic luminescence of relaxed STE is observed at about 2.9 eV (428 nm). The same electronic excitation can be directly created by absorption of photons with energies from 5.5 to 7.0 eV (180-225 nm). Photons of an energy grater than 7 eV create e-h pairs which also give rise to intrinsic luminescence in the recombination process. In real crystals with impurities and defects, various extrinsic luminescence bands can be observed from the recombination of e-h pairs at electron traps located near defect oxyanions. In particular, emission bands at 2.2-2.4 eV (520-565 nm) arise from the recombination of e-h pairs near oxygen vacancies [Böh80]. The presence of Pb^{2+} ions with low-laying energy levels shifts the emission of $CaWO_4$ to longer wavelengths relative to undoped $CaWO_4$ [Gra76].

3.5 Quenching mechanisms

The energy system of any molecule can be represented by a potential energy diagram. Although, the exact shapes of these potentials are known for only a few simple molecules, the general form is similar to that shown in Fig. 3.1-left for a diatomic molecule OA. The interatomic distance is represented along the X-axis and the energy along the Y-axis. The curve aAa' determines the vibration amplitudes of atom A relative to atom O for all vibrational energies of the neutral molecule in the electronic ground state. A molecule in thermal equilibrium at room temperature will possess only a few quanta of vibrational energy, represented by the two levels near A. The upper curve bBb' similarly represents the vibrations of a molecule in an excited electronic state. The two levels near B represent the normal vibrational states when the excited molecule is in thermal equilibrium. The minimum of the potential B is displaced to the right of A due to the increase in bond length. The absorption of a photon by the molecule can cause a transition from the ground state aAa' to bBb'. Such a transition will occur along a vertical line on the diagram, since the electronic change is more rapid than the atomic movements (*Franck-Condon* principle). The tran-

[3] oxygen anion

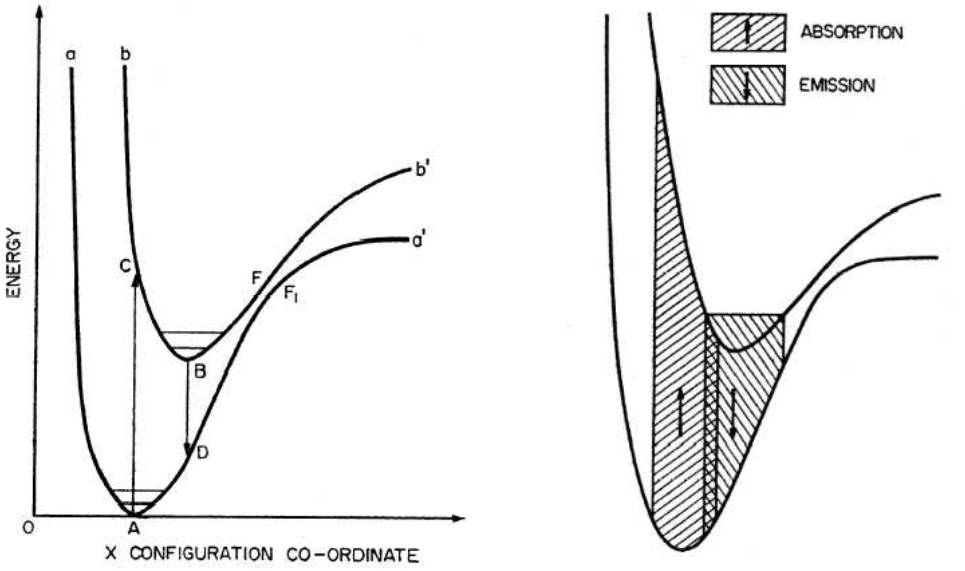

Figure 3.1: Luminescence process in the configurational coordinate diagram.
Left: Potential energy diagram of luminescence center. Right: The absorption and the luminescence emission showing the origin of the overlap of the absorption and emission spectra [Bir64].

sition from A to C raises the molecule into the excited electronic level bBb'. If C is above the limit b' dissociation will occur, otherwise the molecule will be in a high vibrational level of bBb'. It will dissipate its excess vibrational energy rapidly as heat and fall to the point B. If the molecule is sufficiently stable, it may return to the ground-state along the line BD, under emission of scintillation light. The scintillation mean life time is long compared to the period of the molecular vibrations, and hence radiative transition only occurs in molecules in which the energy is not readily dissipated in other ways. The general nature of the emission and absorption spectra can be understood from a consideration of the potential diagram redrawn in Fig. 3.1-right. The absorption spectrum, corresponding to the transition form the ground state to the first excited state, is due to transitions form the first few vibrational levels of A up to bBb'. The emission spectrum, corresponding to the reverse process, is due to transitions from the first vibrational levels of B down to aAa'. Due to the displacement of B towards longer interatomic distances (to the right of A), the emission spectrum is shifted to the long wavelength side of the absorption spectrum, though there is usually a certain overlap. Additional intense absorption bands occur at shorter wavelengths, due to transitions into the second and higher electronic states.

If an excited electron reaches F, the transition F - F_1 can proceed by phonon creation without the emission of a photon. This mode of decay is called quenching and competes with the scintillation process and therefore reduces the intensity of the emitted light.

Four different sources of the quenching are known:

1. **Thermal quenching**
   The widths of absorption and emission spectra depend on the population of states in the respective minima A and B. At higher temperatures the absorption and emission bands broaden, increasing the overlap (see figure 3.1-right) and the fraction of luminescence photons lost due to self-absorption[4].

2. **Impurity quenching**
   As the impurity content is increasing the intensity of emitted light is decreasing mainly due to the decrease in transmittance of the crystal. Additionally, some of the electronic excitations can be lost via an interaction with the impurity ions.

3. **Concentration quenching**
   In the case of doped scintillators, the scintillation intensity depends on the activator concentration, having a maximum for a certain concentration.

4. **Ionization quenching**
   The light output of the scintillators depends on the ionization density. When the specific energy loss is large, the dense ionized ions lead to overlapping excitations and a reduced light emission is observed. For lightly ionizing particles, e.g. electrons, the spacing between successive ionizations is several molecular distances, so the interaction between the ionization sites is negligible.

The quenching of light output from charged particles in inorganic scintillators has been associated with the specific energy loss, dE/dx, of the ion. Assuming that, in the absence of quenching, the differential light yield, dL/dx, is proportional to the energy loss

$$\frac{dL}{dx} = S\,\frac{dE}{dx}\,, \tag{3.12}$$

where S is the scintillation efficiency, Birks [Bir64] proposed that dL/dx, in the case of quenching, has the form

$$\frac{dL}{dx} = \frac{S\,\frac{dE}{dx}}{1 + kB\,\frac{dE}{dx}}\,, \tag{3.13}$$

[4]Being a cryogenic experiment CRESST is not effected by this effect.

where B the *Birks' constant* and k a quenching parameter. Equation 3.13 is commonly referred to as $Birks'\ formula$. For γ irradiation, dE/dx is small for sufficiently large energies and then according to equation 3.13 the incremental light output per unit energy loss is constant

$$\left.\frac{dL}{dE}\right|_{\gamma} = S\,. \tag{3.14}$$

In this case the light output is then linearly related to the initial particle energy $L = S\,E$. For alpha particles dE/dx is large and $Birks'\ formula$ becomes

$$\left.\frac{dL}{dx}\right|_{\alpha} \simeq \frac{S}{kB}\,. \tag{3.15}$$

The appropriate value of kB can therefore be determinated by taking the ratio of these two responses

$$kB = \left.\frac{dL}{dE}\right|_{\gamma} \Big/ \left.\frac{dL}{dx}\right|_{\alpha}\,. \tag{3.16}$$

Different authors are suggesting other extended versions of $Birks'\ formula$ where one or more additional fitting parameters are added in order to obtain better agrement with experimental data [Smi68] [Pap99].
The effect of different radiation on the scintillation efficiency of a scintillator is often expressed in terms of a *quenching factor*, defined as the ratio of scintillation yield per unit energy loss of gamma rays and other radiation. Commonly, one compares the light response for γ-ray to that one of α particles of the same energy (γ/α - ratio).
In Dark Matter search experiments usually one defines the *quenching factor* as the ratio of light yield of electron interactions to light yield of nuclear recoils of the same energy. Theoretical estimates of the quenching factor are provided by the model of Lindhard et al. [Lin63] but experimental measurements have to be performed to verify the validity of this theory at the given energies and for the nuclei of interest for Dark Matter search.

3.6 Characteristics of inorganic scintillators

In this section some of the general properties of inorganic scintillators are discussed with emphasis on the properties of $CaWO_4$ relevant for the use in the CRESST experiment.

3.6.1 Light yield

The essential feature of any scintillator is an effective conversion of ionizing radiation into visible light. The final number of emitted photons depends on each

stage of the scintillation process. Moreover, the determination of the absolute scintillation yield requires an accounting of the light collection efficiency and the quantum efficiency of the photosensor. As the determination of both efficiencies introduces errors the absolute scintillation yield typically has an uncertainty of no less than 5 %.
The light yield defines the discrimination threshold in the CRESST experiment and is therefore one of the critical parameters. Nominally, for $CaWO_4$ a light yield of 6000 photons/MeV for γ -rays is determined [Der92], but as it will be shown in Chapter 5 relatively large sample to sample variations are observed.

3.6.2 Duration of a scintillation pulse

In most of the scintillators, the intensity of the emission $J(t)$ (in photons/s) rises instantaneously and in scintillators with one type of luminescent center decays exponentially with decay time constant τ

$$J(t) \;=\; J(0)\, exp\left(-\frac{t}{\tau}\right), \tag{3.17}$$

where J(0) is the initial intensity. The light yield of the scintillator is then

$$L_R \;=\; \frac{1}{E_\gamma}\int_0^\infty J(t)dt \;=\; \frac{J(0)\cdot\tau}{E_\gamma}\,. \tag{3.18}$$

In case of a finite rise time τ_R the intensity of emission is defined as

$$J(t) \;=\; \frac{N}{\tau \;-\; \tau_R}\left[exp\left(-\frac{t}{\tau}\right) \;-\; exp\left(-\frac{t}{\tau_R}\right)\right], \tag{3.19}$$

where N is number of photons emitted. Decay times for $CaWO_4$ have been measured numerous times. For the main emission band a decay time of 6 μs has been reported [Der92] at 300 K. Different impurities give rise to additional decay time components. Lowering the temperature leads to prolonged decay times. At 77 K for the main emission a decay time of 17.4 μs has been determined. Emission due to oxygen vacancies has 220 μs decay time at 77 K [Gra82]. Being a rare event search CRESST is not affected by a long decay time. As mentioned before, the light detector used in CRESST Phase II is optimized for the light collection from $CaWO_4$ and therefore its integration time is adjusted to the $CaWO_4$ decay time.

3.6.3 Afterglow

A scintillator can display a delayed luminescence (order of tens of microseconds and above) which is called afterglow. The origin of this effect is phosphorescence arising in the crystal due to the thermal release of carriers from traps. The intensity, spectral composition and the decay time of the afterglow depend on the purity of the raw material, crystal growing conditions, heat treatments etc.

3.6.4 Temperature dependence of the response

The temperature dependence of the light yield is determined by the change of the probability of nonradiative transitions with temperature.
An important criterion for the choice of the scintillator for CRESST was the light yield at low temperatures. The scintillation efficiency of $CaWO_4$ increases with cooling. The temperature dependence consists of a flat part at lower temperatures and an adjoining S-shaped part in the upper temperature region[5]. An increase of up to $\sim$ 60 % has been observed with strong sample-to-sample variations [Kee02].

3.6.5 Optical properties

The main optical characteristics of a scintillator are the index of refraction and the transmissivity. The scintillator should be transparent for its own emitted light. The light can be absorbed by impurities and defects, as well as by the host crystal itself. The level of impurity absorption depends on the concentration of non-intentional impurities and point defects. The transmission can be reduced also due to bulk elastic scattering. The transmission of the material is then determined by a sum of two effects: absorption and scattering. The high energy edge of the crystal transmission is typically at about 0.8-0.85 E_g[6].
Another important characteristic of a scintillator is its index of refraction n. A small index of refraction is desired as in case of a high index light trapping due to total internal reflection is more likely.
$CaWO_4$ has a high index of refraction $n = 1.93$, which requires an additional treatment of the crystal surface to increase the light collection efficiency. Results concerning the transmissivity and light collection of large $CaWO_4$ single crystals will be presented in section 5.1.2.

[5]The temperature position of the inflection point is typically between 200 K and 250 K and shows strong sample to sample variation.

[6]where E_g is band gap of the crystal

Chapter 4

Measurement techniques

For the examination of the properties of $CaWO_4$ scintillating crystals various techniques were used in this thesis. The methods to study the scintillation efficiency will be described in this chapter. Also the main features of existing setups used for transmission and luminescence measurements are presented. Finally, a new technique developed for the determination of the quenching factors for nuclear recoils of oxygen, calcium and tungsten in $CaWO_4$ crystals is described.

4.1 Measurement of scintillator light output at room temperature

As large $CaWO_4$ crystals are not readily commercially available in a quality required for a WIMP cryodetector, a strong R&D effort was necessary to improve crystal qualities by providing feedback to the various manufactures. For that purpose we have assembled a setup for comparative measurements of the light yield of cylindrical ($\varnothing = 40\,\mathrm{mm}$; $\mathrm{h} = 40\,\mathrm{mm}$) $CaWO_4$ crystals (Fig. 4.1). The light was detected using a Photonis green extended (XP3461B) photomultiplier tube (PMT) with a base modified to integrate the light over $400\,\mu\mathrm{s}$. The signal was fed into a differential amplifier followed by a commercial research amplifier (Ortec 450). After shaping the signal was fed into a multichannel buffer (Ortec 926) and the resulting pulse height spectra were read out using the Ortec MAESTRO software. For most measurements, the crystal was kept in the plastic holder facing the PMT without any optical coupling[1]. The holder allows the usage of different reflector materials and quick and simple exchange of the crystals. Commonly, for comparison measurements a polymeric high reflectivity foil VM2000 [3M] was used[2]. ^{137}Cs (661.6 keV) and ^{60}Co (1.17 and 1.33 MeV)

[1] Coupling materials may contain radioactive contaminants and are hard to be removed from the surface, therefore whenever possible, their usage was avoided.

[2] Results concerning the properties of this foil will be presented in section 5.2.2 .

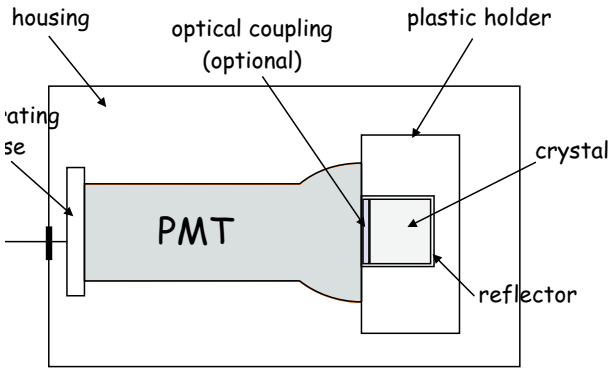

Figure 4.1: Scheme of the setup used for the room temperature measurement of the light yield of the $CaWO_4$ crystals for the CRESST Phase II experiment. The components are discussed in the text.

γ sources were used for irradiation. One of the crystals, with a relatively high light yield, was used as a standard to which the light response of other crystals was normalized.

4.2 Transmission measurement

Transmission measurements were performed at room temperature using a Perkin Elmer Lambda 19 spectrometer at the Technical University of Munich in Garching. The transmission spectra were taken in the visible range from 250 nm to 700 nm in 1 nm steps with a spectrometer slit of 1 nm and a screening speed of 60 nm per minute. A special holder (see figure 4.2) was prepared to allow the measurement of the transmittance along the radius of the crystal.

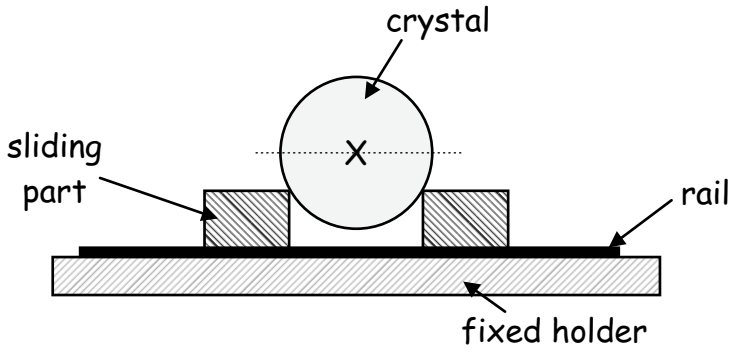

Figure 4.2: Schematic cross-section of the holder used for the transmission measurements. $\times$ points to the beam position and the doted line represents alternative positions selected for the measurement.

4.3 Luminescence measurements

For a better understanding of the impurity content and its effects on the total light yield, the luminescence, under X-ray, UV and VUV excitation, of small samples taken from the ingots was studied.

X-ray excited luminescence

The samples were measured in the temperature range of 77 - 500 K, using the facility at Durham University in Great Britain, under continuous irradiation with X-rays (W-anticathode; V = 30 kV; I = 20 mA). The samples were mounted on the copper holder of a liquid nitrogen cryostat. The temperature was measured by a copper/constantan thermocouple and controlled using a heater with an accuracy of $\pm$ 1 K. The luminescence spectra were analyzed using a grating monochromator and a Hamamatsu R2949 photomultiplier.

UV excited luminescence

The UV excited luminescence measurements were done at the University of Tartu, Estonia, at liquid helium temperature under irradiation by UV light from a DDS-400 deuterium discharge lamp through a double - quartz monochromator DMR-4. The samples were mounted on the copper holder of a helium bath cryostat. The luminescence spectra were measured using a photomultiplier tube EMI9863.

VUV excited luminescence

Luminescence studies of $CaWO_4$ samples under monochromatized vacuum-ultraviolet (VUV) excitation, in the 8 - 300 K temperature range, were made at the SUPERLUMI experimental station [Zim91], located in HASYLAB (Hamburger Synchrotronstrahlungslabor) at DESY (Deutsches Elektronen-Synchrotron). The samples were mounted on the copper holder of a helium flow cryostat. The temperature was controlled to an accuracy of $\pm$ 0.5 K. The excitation spectra were normalized to equal quantum intensities of the synchrotron radiation falling onto a crystal. The primary monochromator causes an energy dependence of the VUV intensity. Therefore, the excitation (and reflection) spectra have to be corrected for the incident photon flux. A reference standard of known absolute fluorescence efficiency, sodium salicylate (emission spectrum peaked at 420 nm with a width of about 80 nm), was used for the normalization. The SUPERLUMI primary monochromator is equipped with a MgF_2 coated aluminium grating and a platinum grating with working ranges of 65 - 330 nm and 30 - 300 nm, respectively. The analysis of the ultraviolet, visible and infrared luminescence at SUPERLUMI is done with a 30 cm monochromator-spectrograph ARC SpectraPro-308.

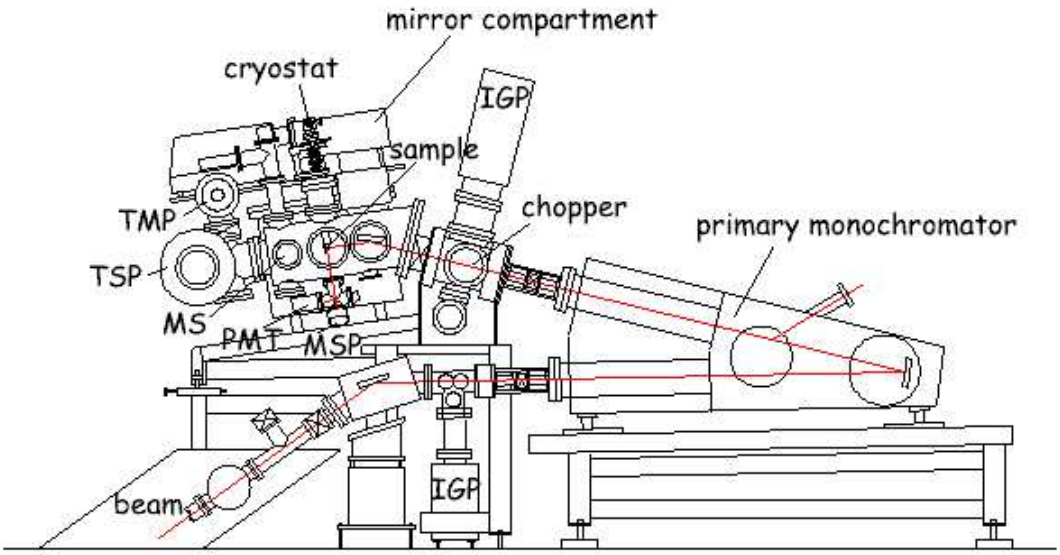

Figure 4.3: Scheme of the SUPERLUMI experimental station. MSP: Micro-Sphere-Plate, PMT: Photo-Multiplier-Tube, IGT: Ion-Getter-Pump, TMP: Turbo-Molecular-Pump, TSP: Titan-Sublimation-Pump, MS: Mass-Spectrometer.

The monochromator has two exit ports, one of them equipped with a photomultiplier (Hamamatsu R6358P) and the other with a LN_2-cooled two-dimensional CCD-camera. For the reflectivity measurements (with a Valvo XP2230B PMT), VUV light reflected from the sample is converted into fast broadband emission peaking at 420 nm using a semitransparent sodium salicylate layer. For details on SUPERLUMI see reference [Zim91].

4.4 Quenching factor measurements

Nuclear recoil quenching factor measurements have been performed on scintillation detectors such as NaI [Spo94][Tov98], CaF_2(Eu) [Tov00], CsI(Tl) [Hor92] in neutron scattering experiments.
We have developed a new technique for the measurement of quenching factors of different nuclear recoils in scintillating targets. Instead of measuring the light produced by the recoil nuclei of the target material as in the neutron scattering experiments, this technique is based on the measurement of light produced by different ions impinging into a crystal. As this work was done in the framework of the CRESST experiment, $CaWO_4$ was used as a target material. Ions with fixed kinetic energy are produced by a time-of-flight mass spectrometer (TOF-MS) with a Laser Desorption / Ionization ion source (LDI). The light is detected with a photodetector. A ^{55}Fe source was used for reference measurements.

This method has several advantages compared to traditional neutron scattering experiments. The main advantage is that it is a simple "table-top" experiment. Measurements can be performed within a short period of time with an easily adjustable energy and a profuse choice of nuclei. A possible limitation may be surface effects if the light output for energy depositions close to the crystal surface were different from that for bulk depositions. Therefore, the technique can be used in principle for any (solid) scintillation material, which does not suffer from a surface degradation of the surface efficiency.
In this section a description of the TOF-MS and the ion source used for these measurements is presented. The procedure for the room temperature measurement is then explained followed by a description of the low temperature setup.

4.4.1 Linear time-of-flight mass spectrometer - TOF-MS

In an electric potential difference U ions of charge state z will gain the kinetic energy

$$zeU \;=\; E_{pot} \;=\; E_{kin} \;=\; \frac{mv^2}{2}\,, \tag{4.1}$$

where m and v are the mass and the velocity of the ions, respectively. The ions with a defined kinetic energy then travel a time of flight distance of D (of about 3 m) before reaching the detector (commonly a Micro Channel Plate (MCP)). According to equation 4.1 light ions will fly faster then heavy ions. The square of the flight time is proportional to m/z. Neglecting the time-of-flight of the ions in the ion source, the flight time t is

$$t \;=\; D\sqrt{\frac{1}{2eU}\,\frac{m}{z}}\,. \tag{4.2}$$

4.4.2 Mass spectrometer with a LDI ion source

Figure 4.4 shows the scheme of the time-of-flight mass spectrometer with a LDI ion source used for this measurement. The instrument was built for the mass spectrometry of heavy bio-molecules using cryogenic detectors [Chr04].
The spectrometer is split into two vacuum chambers connected with a small gate valve. The LDI source is housed inside the small vacuum chamber while all other components are in the main vacuum chamber. This allows to vent just the small compartment for the exchange of the target, with minimal interruption ($\simeq$ 20 min) of the operation.
The target material is placed onto a stainless steel holder on top of a stick which is inserted along the ion beam axis from the back side of the LDI source. The stick can be rotated and moved transversely. Six different target materials can be mounted on the target holder simultaneously. Silver epoxy is used to fix the materials (Fig. 4.5).

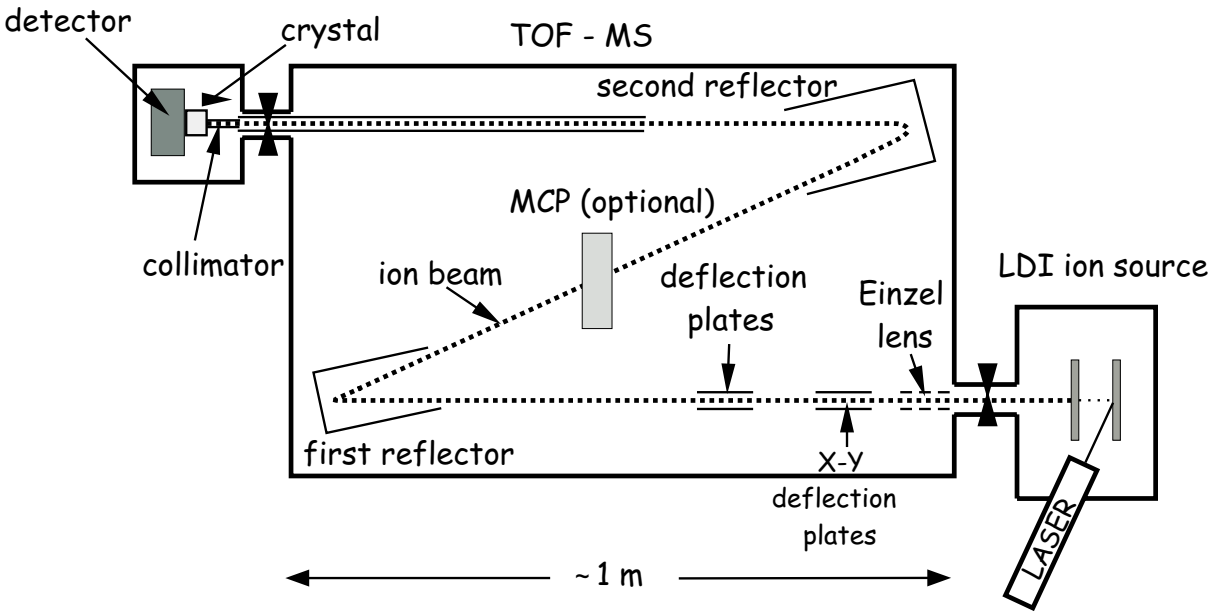

Figure 4.4: Scheme of TOF-MS.

A shot from the pulsed UV laser of 337 nm wavelength desorbs and ionizes the atoms (molecules). The shot duration is in the order of nanoseconds. The laser power can be controlled with a dielectric attenuator and the beam is focused on the sample disc with a lens of 200 mm focal length. At the sample target the laser power density is typically 10^6 - 10^7 W/cm^2. The laser shot is used as a trigger for the time-of-flight measurement. The maximum acceleration voltage of the LDI ion source is 18 keV. The ion beam is focused using an Einzel lens and deflected in the electric field of X-Y deflection plates.
The MS is instrumented with an additional ion deflector acting as a beam filter. It consists of a pair of plates the electric field of which is turned on when the

Figure 4.5: Target holder with six different materials.

laser shot is fired. It deflects all ions out of the beam path until the electric field is switched off. Therefore, all lighter ions preceding the beam are deflected. The high voltage is then switched off to allow the passage of the desired ions and then is switched on again in order to block higher mass ions following the beam. This method allows a selection of ions with a certain mass to pass and form the ion beam. The time-of-flight part used for the quenching factor measurements consists of two ion mirrors. The first one is used to tune the focus onto the detector plane while the second ion mirror reflects the ion beam with little influence on the ion focus. For details see [Chr04]. Between the two reflectors an additional movable MCP can be inserted into the ion path at any moment of the operation. It was used to determine the time-of-flight of certain ions as well as for alignment purposes.
At the beam outlet of the main vacuum chamber a gate valve with a clearance of 50 mm is mounted. Either the room temperature setup or the cryostat with its cooled snout may be mounted there.
For the operation of the mass spectrometer the proper set of parameters has to be found in order to focus the ion beam onto the detector. The values that have been determined with a MCP mounted at the outlet of the spectrometer are presented in the table 4.1

Table 4.1: Settings of the mass spectrometer ion optics used in this work.

Acceleration voltage	18 kV
Excitation voltage	13 kV
Mid grid voltage (Reflector ♯1)	16.4 kV
End grid voltage (Reflector ♯1)	23 kV
Reflector ♯2 grid voltage	20 kV
Beam deflection voltage horizontal	191 V
Beam deflection voltage vertical	70 V
Ion lens voltage	9.6 kV (changeable)

4.4.3 MCP measurements

The Micro Channel Plate (Burle) mounted between the two reflectors of the main vacuum chamber was used to select target materials and to determine the deflection plate time constants and the time of flight for each ion species. The operating voltage was 2.58 kV. The parameters used for the mass spectrometer ion optics are presented in Table 4.1.
The laser pulse was used as a start trigger and the signals of the MCP for the

time-of-flight measurement were read out using a PC based transient digitizer. Due to the position of the MCP, the measured time-of-flight is roughly half of the one at the outlet of the mass spectrometer. The time constants for the ion deflection plate have been determined by the following procedure. Starting values for C [3] and D [4] were chosen so that all ions are passing through and reach the MCP (0 ns and 30 μs respectively). Afterwards, values for C and D were set such that only the desired ions could pass (see figure 5.42).

4.4.4 Room temperature set-up

The room temperature setup consists of a small crystal viewed by a photomultiplier tube, placed in a housing that is mounted at the outlet of the mass spectrometer (Fig. 4.6). The $CaWO_4$ crystal ($5\times5\times5\,mm^3$) is placed in a teflon reflector holder. A collimator hole ($\varnothing = 1$ mm, length $= 8$ mm) turned to the mass spectrometer outlet is drilled in the teflon holder. In order to reduce the

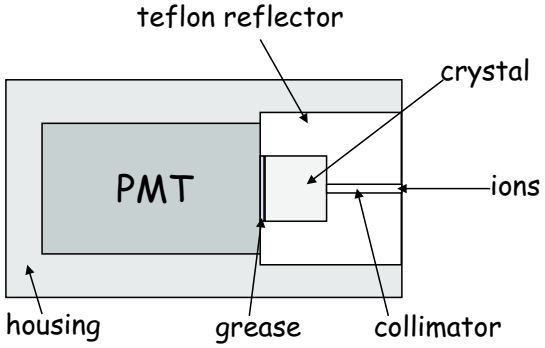

Figure 4.6: Scheme of setup used for the room temperature measurements of quenching factors (not to scale). The components are discussed in the text.

effect of trapped light in the crystal, the crystal surface facing the photomultiplier tube (PMT) is roughened. Additionally, a thin layer of silicon grease is placed between the crystal and the PMT for optical coupling. The PMT used for the measurements is an Electron Tubes 9124B selected for a low rate of dark counts. A preamplifier followed by a fast digitizer (Fast ComTec - TRP250/500; 500 MHz) is used for the read out of the PMT signal. The data acquisition is triggered by the laser signal. For each laser shot photons are counted online by counting the number of voltage pulses exceeding a given threshold amplitude in a defined period, after the arrival of the ion type of interest (see figure 4.7). In order to eliminate ringings from being counted that are appearing after the pulses, an additional positive threshold is applied to generate 12 ns inhibition period after each event. The number of registered photons for each shot is then

[3] time from the laser shot till the electric field is switched off
[4] time after which the electric field is switched on again

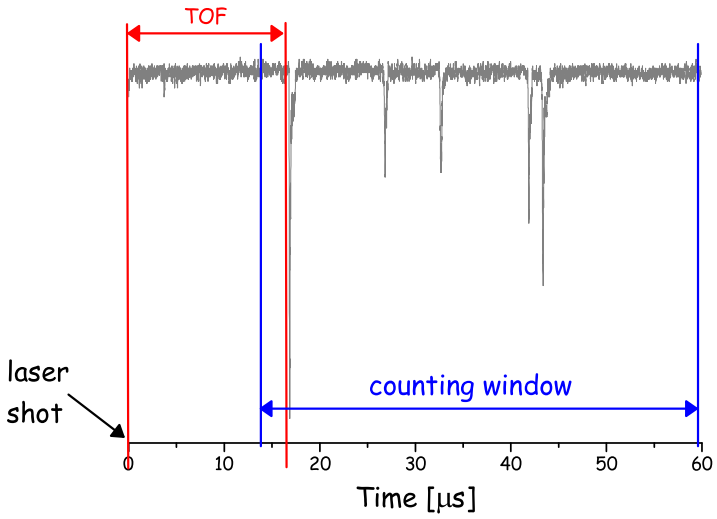

Figure 4.7: The photomultiplier signal from one laser shot. The transient digitizer is triggered by the laser signal to trigger the data acquisition. After the time-of-flight the ion hits the crystal. In the figure voltage pulses from single photons created by the ion are shown. To reduce the background contribution due to the dark counts of the photomultiplier profit of known time-of-flight for the selection of the counting window is made. The duration for the counting window was kept the same during all measurements. The counting of the photons is then performed as explained in the text.

recorded into a histogram and written to disk. Additionally, for each registered photon its arrival time is recorded. Therefore, a second histogram is produced using this information giving the light curve of the scintillator and the time-of-flight of the ions (See figure 5.44).
The reference measurement for the quenching factor is made with 5.9 keV X-rays from a ^{55}Fe source. The radioactive source can be installed in front of the collimator without any change of setup geometry. To trigger the data taking the signal from the PMT is used. The photon counting is performed the same way as with the ions.

4.4.5 Low temperature set-up

To further investigate quenching factors at low temperatures which is of particular importance for CRESST Phase II a setup was assembled that can be used inside of the He bath cryostat which can be mounted at the outlet of the mass spectrometer. The goal was to measure quenching factors at liquid helium temperature.

The detection efficiency of the more sensitive bialcali photomultiplier tubes is dramatically decreasing with cooling to temperatures below 200 K [Ich93]. On the other hand multialcali photomultiplier tubes, that could be cooled down to liquid nitrogen temperatures without significant decrease of sensitivity, are less sensitive compared to bialcali ones [Ich93]. Therefore, the decision was made to use a large area silicone Avalanche Photo - Diode (APD). APDs can be used, in so-called Geiger mode for single photon counting [Kin97]. In this mode the APD is biased above its break down voltage and the absorption of a photon initiates an avalanche breakdown, which can easily be detected. Advantages of APDs over PMTs are the large quantum efficiency, smaller size and a lower bias voltage. Disadvantages are a limited active area and a larger number of dark counts. Cooling down APDs to liquid nitrogen temperature significantly reduces the amount of dark counts and therefore allows detection of low level light with low background rate [Yan03]. APDs are not effective below the carrier freeze out temperature (≈ 40 K for Si) [Yan03].
Figure 4.8 shows a scheme of the low temperature setup. A $CaWO_4$ crystal ($5\times5\times5\,mm^3$) is placed in a teflon reflector. In order to increase the light collection efficiency the side oriented to the light detector is roughened. Teflon screws are used to hold the crystal at the fixed position and to provide thermal contact. The teflon reflector is kept in a copper housing which is thermally anchored to the 4 K bath via a copper wire ($\varnothing = 0.8$ mm). A collimator hole ($\varnothing = 1$ mm, length $= 8$ mm) is aligned to the mass spectrometer outlet (see Fig. 4.8). A ruthenium-oxide thermometer placed at the copper holder is used for monitoring the temperature of the crystal. During the whole measurement time the temperature was stable at 6.22 ± 0.02 K.
For light detection a Hamamatsu photonics windowless silicon avalanche photodiode S8664-50N ($\varnothing = 5$ mm), is used. The APD is placed in a copper holder which is thermally anchored via a copper wire ($\varnothing = 0.8$ mm) to the 77 K bath. The active area of the APD is aligned with the crystal at a distance of < 2 mm. To stabilize the temperature of the APD at 94.40 ± 0.05 K a four point measurement of the platinum resistor, placed on the copper holder, and a heater controlled via an AC resistance bridge (LR 700) is used. The break down voltage of the APD at that temperature is 295 V and the operational voltage used for the measurements is 336 V. The signal from the APD is transported to room temperature using semi-rigid co-axial cable thermally anchored at the 77 K plate (Fig. 4.8). The passive circuit that is used for read out, is placed outside of the cryostat. The APD is connected to the power supply through a series resistor. If the current through the diode is zero, the voltage across the diode equals V_{bias}, which is larger than the breakdown voltage. If the diode breaks down, the series resistor reduces the voltage across the APD, which then quenches the avalanche. After the breakdown is quenched, the diode is recharged through the resistor. Like in the room temperature setup the signal passes the preamplifier before being

recorded by the digitizer. Even at this low operating temperature, the number of dark counts is higher compared to the room temperature photomultiplier measurement. In order to reduce the number of dark counts, an online pulse height discrimination technique is applied, as the voltage signals coming from the scintillation produced in the crystal are significantly smaller in amplitude compared to the dark counts. The photon counting is performed online by counting the number of voltage pulses with an amplitude between two given thresholds in a defined period of time for each laser shot. Records containing dark counts are fully rejected. In order to eliminate ringings that are appearing after the pulses, inhibition time of 24 ns is applied after each registered pulse. The number of registered photons for each shot is then recorded into a histogram and written to disk. The light curve histogram is produced in the same way as in the room temperature measurements.

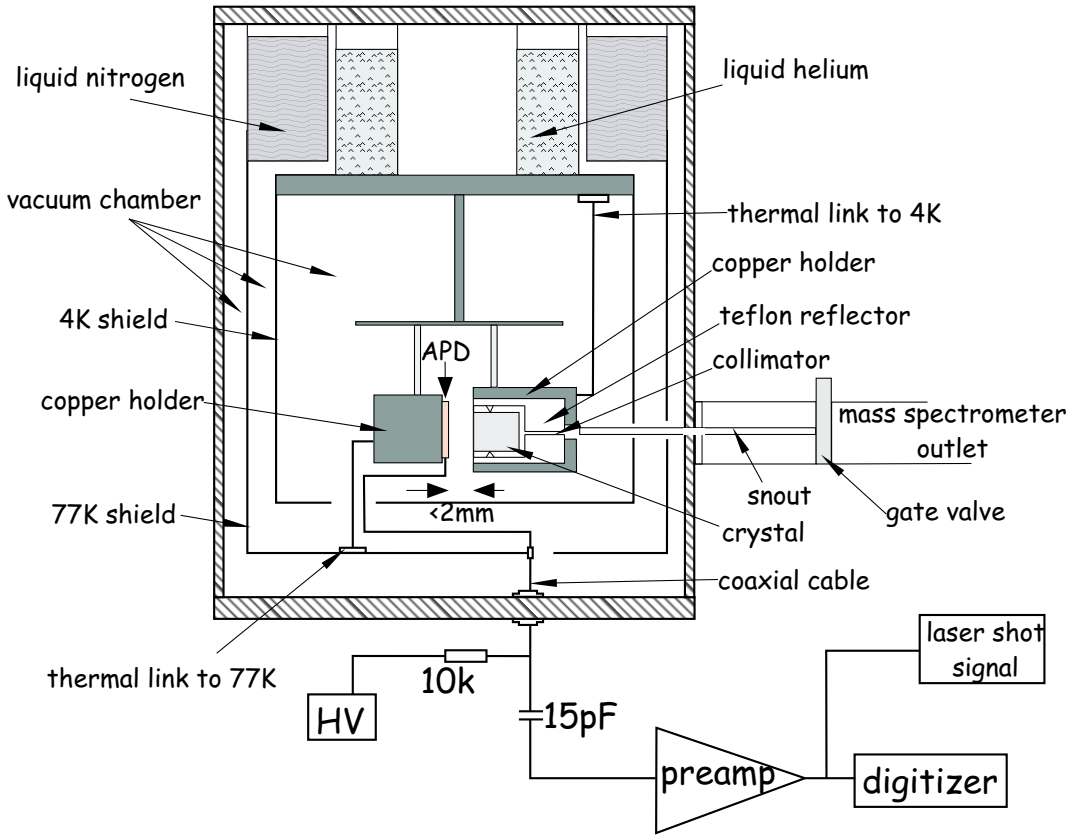

Figure 4.8: The scheme of the setup used for low temperature measurements of the quenching factors (not to scale). The components are discussed in the text.

Chapter 5

Results

As described in Chapter 2 the scintillation properties of the absorber are of crucial importance for the background rejection efficiency of direct Dark Matter searches based on phonon-light detection. Therefore, an extensive study of all aspects related to the emission and detection of scintillation light of $CaWO_4$ has been carried out. Additionally, an absorber to be used in low-background cryogenic experiments needs to satisfy the criteria named in section 2.2.2. The main goal of the work presented in this thesis was the characterization of the properties of $CaWO_4$ scintillating crystals which are of interest for the use in the CRESST Phase II experiment. Special attention was given to those characteristics which had to be improved in order to satisfy the requirements of sensitive Dark Matter search.
Crystals from four different sources were studied:

1. Pozdnjakov, Ukraine - crystals labelled using male names (Ukrainian crystals);

2. General Physics Institute, Moscow, Russia - crystals labelled using female names (Russian crystals);

3. KARAT company, Lviv, Ukraine - crystals labelled KN, where N is a number (Karat crystals);

4. Shanghai Institute of Ceramics, Chinese Academy of Science - crystals labelled ChN, where N is a number (Chinese crystals).

All crystals were grown by the Czochralski method. The observed quality variations are mainly due to differences in the purity of the raw material and crystal growing conditions as it will be shown later. All examined crystals have a cylindrical shape with a diameter of $\simeq 40\,\mathrm{mm}$ and a hight of $\simeq 40\,\mathrm{mm}$.
In this chapter results of investigations into non-intended impurities in the crystals, are presented. Special attention was given to the measurement of the radioactive impurity content. Furthermore, results from measurements using the

facilities described in Chapter 4, are given. They were performed in order to improve the understanding of the influence of different parameters on the light yield of $CaWO_4$ and the light collection efficiency of the setup. Finally, results obtained using the novel technique to determinate quenching factors, that has been developed in our laboratory (see section 4.4), are presented.

5.1 Properties of the crystals

Calcium tungstate (scheelite), $CaWO_4$, is a naturally occurring luminescent mineral that can also be produced synthetically. Its scheelite structure is characterized by the tetragonal space group $I4_1/a$ or C_{4h}^6 (listed as No. 88 in [Hah87]). In this structure, the primitive unit has two ABO_4 units (where A = Ca; B = W). The A and B sites have S_4 point symmetry, and the crystal has an inversion center. The O sites have only a trivial point symmetry and they are arranged in approximately tetrahedral coordination around each B site. The crystal structure has been described as highly ionic with $A^{+\alpha}$ cations and tetrahedral $BO_4^{-\alpha}$ anions where $\alpha \simeq 2$. The $BO_4^{-\alpha}$ anions are themselves highly ionic with formal charges of $B^{+\beta}$ and $O^{-\gamma}$, where $4\gamma - \beta \equiv \alpha$.

Figure 5.1: $CaWO_4$, ingot as grown.

All crystals used in this work were grown by the Czochralski method: A seed crystal is attached to a rod, which is rotated slowly. It is dipped into a melt kept at a temperature slightly above the melting point. A temperature gradient is introduced by cooling the rod and slowly pulling it out of the melt. The surrounding atmosphere is cooler than the melt. Decreasing the speed with which the crystal is pulled, reduces the number of crystals defects but decreases the purification from unintended impurities in the melt. After crystal growing is finished the ingots (Fig. 5.1) are usually annealed (400°C - 500°C) to reduce stress and allow mechanical processing.
$CaWO_4$ is an optically anisotropic crystal. Figure 5.2 depicts the propagation of

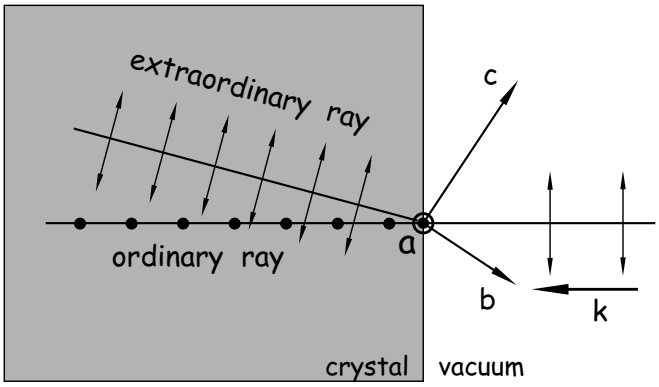

Figure 5.2: Propagation of the ordinary ray and the extraordinary ray in a scheelite crystal for the incident light coming perpendicular to the crystal surface. The b and c axes and the vector **k** are in the same plane, while the a axis is perpendicular to this plane. The electric vector of the extraordinary ray is in the $b\,c$ plane, while that of the ordinary ray is perpendicular to this plane.

light incident perpendicularly on a surface of a uniaxial crystal such as scheelite, where the optical axis (c axis) is at an angle θ with the normal to the crystal surface (**k** axis). Inside the crystal the light is split into two rays of light of orthogonal linear polarization. An "extraordinary" ray with the electric vector parallel to the plane which contains the wave vector **k** and the c axis propagates with a velocity different from that of an "ordinary" ray with electric vector normal to this plane. As the crystal is rotated about the axis **k**, the ordinary ray remains stationary, and the extraordinary ray traces a circle about the other (see Fig. 5.3).
Optical anisotropy is usually quantified by the birefringence defined as $\Delta n = n_e - n_o$ where n_o is the refractive index for the ordinary ray and n_e for the extraordinary ray. More generally, an anisotropic dielectric material has a dielectric constant that is a rank 2 tensor (3 by 3 matrix). A birefringent material corresponds to the special case of a real symmetric dielectric tensor with eigenvalues of n_o, n_o and n_e along the three orthogonal principle axes of polarization. $CaWO_4$ has a refractive index between 1.918 - 1.937 and therefore a maximum birefringence of 0.019.
Crystal orientation was checked by a Laue X-ray diffractometer. Representative images are shown in figure 5.4. Ukrainian and Chinese crystals as well as the crystals from the second delivery by Karat have their optical axis aligned parallel with their physical axis, while Russian and Karat crystals from the first delivery have a disorientation of $\simeq 17^\circ$ and $\simeq 24^\circ$ respectively.
Double imaging (see Fig. 5.3) was not observed in the oriented crystals (c axis parallel to the physical axis).

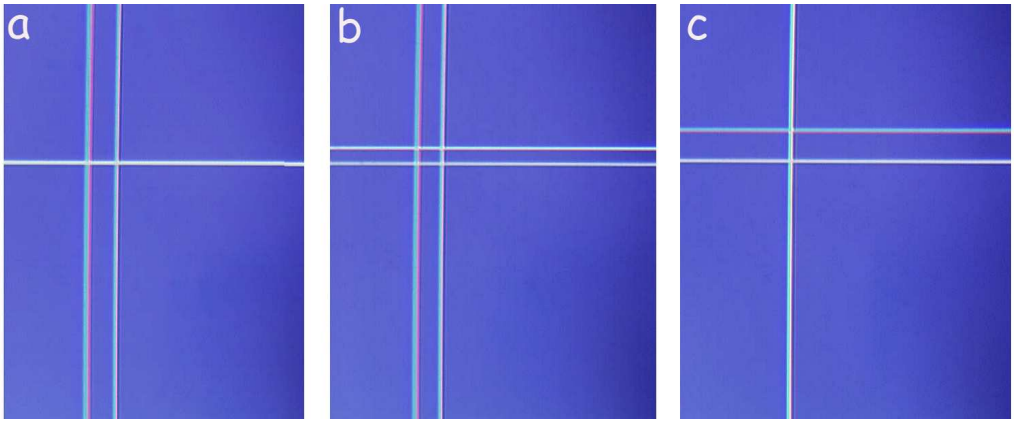

Figure 5.3: A simple demonstration of the birefringence (double imaging) of $CaWO_4$ can be achieved by viewing crossed lines through the crystal. In the initial position (a) the horizontal line can be seen as a sharp line while the vertical is doubled. Rotation of the crystal, by an angle $< 90°$ both lines are doubled (b). Finally, rotation of the crystal by 90° with respect to the initial position gives a swapped picture of the lines (c).

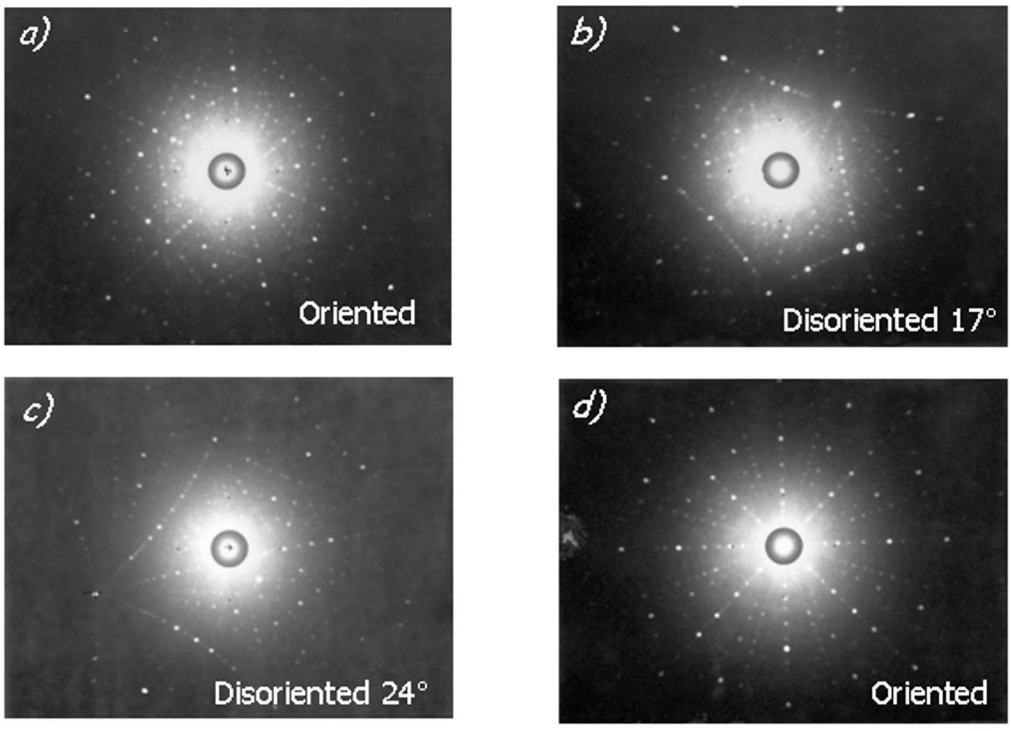

Figure 5.4: Typical X-ray Laue patterns of shaped crystals: a) Ukrainian (Boris); b) Russian (Berta); c) Karat (K02) and d) Chinese crystal (Ch01).

5.1.1 Purity of the crystals

As already mentioned, radiopurity of detector materials in a low background experiment is imperative. Additionally, the light yield of the scintillator can be significantly reduced due to presence of different chemical impurities. Therefore, the purity of the raw material, from different suppliers (to be used for crystal growing), as well as the purity of the grown crystals, was checked using different standard techniques. These include HPGe (High Purity Germanium) γ - spectroscopy and ICP-MS (Inductively Coupled Plasma Mass Spectroscopy). Finally, contaminations from the natural radioactive decay chains and other α - unstable isotopes, as well as low energy gamma activity (below 100 keV), have been identified by α - spectroscopy with high sensitivity using the test runs in the Gran Sasso setup. Tables containing detailed results of the HPGe and ICP-MS

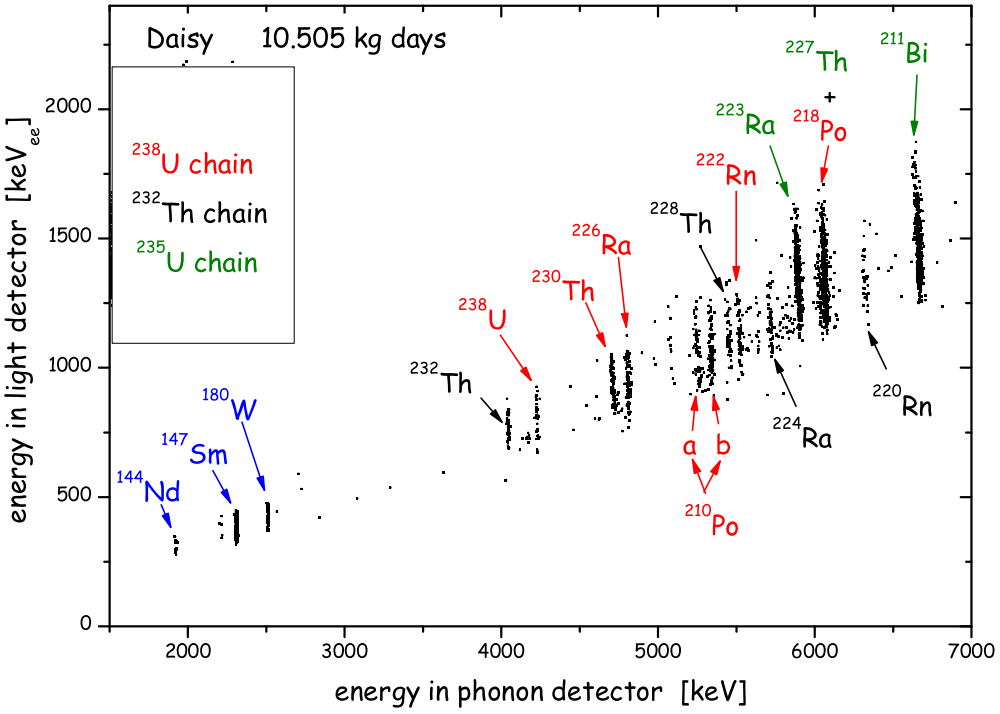

Figure 5.5: Scatter plot of the α region of one of the Russian crystals (Daisy). A contamination of ^{226}Ra of 106±10 μBq/kg has been identified. In the case of ^{210}Po an internal (b) contamination (of 115±10 μBq/kg) and external (surface) (a) contamination (of 22±3 μBq) can be distinguished due to the reduced energy deposition because of the daughter nuclei leaving the crystal surface.

measurements of both, the powders and the crystals, are presented in Appendices A and B respectively. Here the main conclusions are drawn.
As $CaWO_4$ crystals are usually grown from the melt of a mixture of $CaCO_3$ and WO_3 powders, both powders were examined using the HPGe and the ICP-MS techniques. Although one would expect the WO_3 powder to contain more radioactive impurities, due to heavy mass constituents, the results showed a different behavior. $CaCO_3$ powders measured with the HPGe detectors showed significantly higher contamination (up to a few Bq / kg) with ^{238}U chain elements whereas the activity of the WO_3 powder was below the detection limit.
Once the quality of the raw material is shown to be satisfactory, the HPGe measurement of the grown crystals as well as the ICP-MS study of the small samples from the ingots are performed.
In the case of the Russian and the Chinese crystals the amount of the internal radioactive impurities was generally (exceptions see Table A.3) below the detection sensitivities of the HPGe. A significant amount of ^{176}Lu was detected in the Chinese crystals (12 mBq/kg). Elements of the ^{238}U natural chain were detected in both Ukrainian and Karat crystals with activities up to 100 mBq/kg.

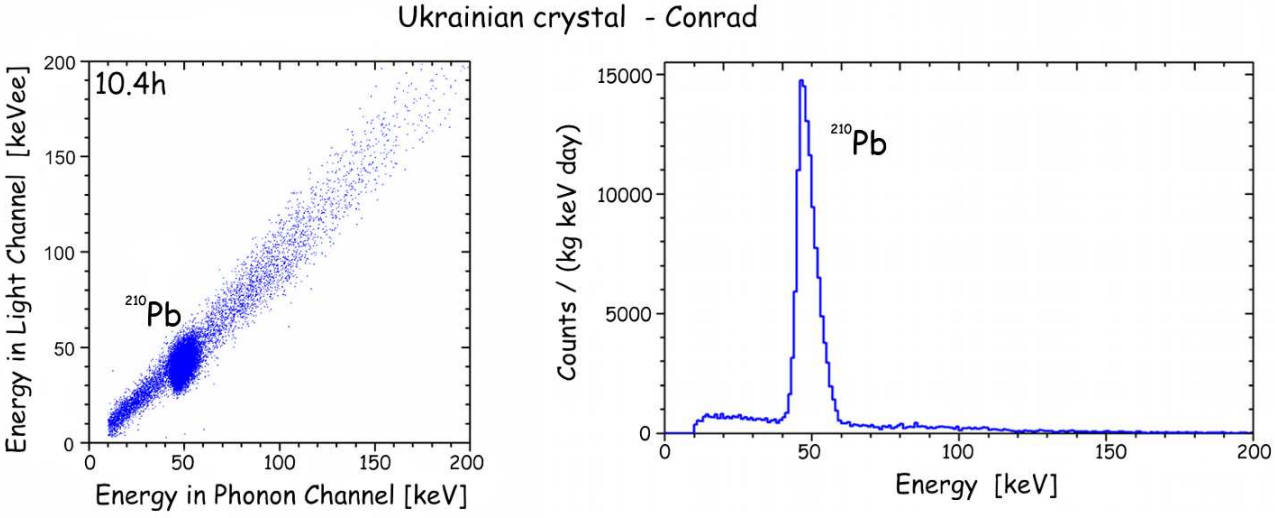

Figure 5.6: ^{210}Pb peak measured on one of Ukrainian crystals (Conrad). Left: Scatter-plot of the 10.4 h measurement showing a prominent ^{210}Pb peak. Right: The 46 keV gamma emission line is broadened and shifted to the right side by the 17 keV end point beta spectrum.

Due to the high Z value of $CaWO_4$ low energy gamma emitters could not be detected with good sensitivities using Ge γ spectroscopy. Taking advantage of the powerful discrimination of the CRESST Phase II detectors, a contamination from the natural decay chains and other α -unstable isotopes have been identified by their α -decays with a sensitivity of $\sim 1\,\mu$Bq/kg [Coz04]. Up to now

only crystals from the Russian and the Ukrainian supplier were operated as detectors in the Gran Sasso setup. The amount of internal radioactive impurities of the crystals from the Russian supplier (Fig. 5.5) turned out to be reasonably low (~ 5 electron recoils/(kg keV day) at E $<$ 100keV). An α-contamination with ^{147}Sm (E = 2.4MeV), and a contamination of $\simeq 35\,\mu Bq/kg$ of ^{238}U; $\simeq 45\,\mu Bq/kg$ of ^{232}Th from the natural decay chains was observed. The elements of the ^{238}U chain are not in secular equilibrium. The contribution from the upper part of the Uranium chain, above ^{226}Ra is rather small. As ^{226}Ra has a half-life of 1620 years and all daughter nuclei down to ^{210}Pb a much shorter lifetime, an equilibrium state is reached quickly and thus all daughters have the same decay rate as ^{226}Ra. ^{210}Pb has a half-life of 22 years and therefore the lower part of the chain below ^{210}Pb is absent as expected for a contamination with ^{238}U chain activity which occurred recently, i.e. much less than 22 y ago. For the crystals from the Ukrainian supplier an overall count rate of up to 1 Hz [1] above 10 keV was measured. The spectrum in the case of these crystals is dominated by the ^{210}Pb decay features (Fig. 5.6). ^{210}Pb is a β-unstable isotope and decays to ^{210}Bi with a Q - value of 63 keV. The beta spectrum has an end point at 17 keV and 63 keV with 84 % and 16 % branching ratio, respectively. Therefore, the decay is accompanied by a 46 keV gamma line. A contamination of $\simeq 1.2$ Bq/kg of ^{210}Pb was detected. The identification of other impurities in these crystals was not possible due to the substantial pile-up present during the whole operation time. Non-radioactive chemical contaminations of crystals were studied by ICP-MS. For these analyse small pieces of the crystal ingots were ground up and dissolved in a HNO_3+HF mixture. Significant levels of rare earth element impurities were present in the Russian crystals (Y, Nd, Gd and Er, all $>$ 1ppm). A samarium contamination was detected in samples from all providers (~ 20 ppb for Ukrainian, ~ 80 ppb for Russian sample). Tellurium and lutecium contaminations were detected in the samples of Chinese origin (see Table B.5).

5.1.2 Transmission of the crystals

Big $CaWO_4$ single crystals were not commercially available. The first samples of crystals of desired shape that were delivered had a slight coloring and often had reduced transparency. Inclusions were also frequently present. Optimization of the crystal growth parameters finally yielded highly transparent and colorless crystals as the ones shown in figure 5.7.
As the transmission of a crystal is determined by the purity of the raw materials and the crystal growing conditions, transmission measurements of randomly selected crystals were done in order to compare the quality of the crystals from different producers and to check the reproducibility of the quality of the crystals.

[1] about 0.25 Hz are due to alpha contaminations and ~ 0.7 Hz arise from gamma and beta interactions

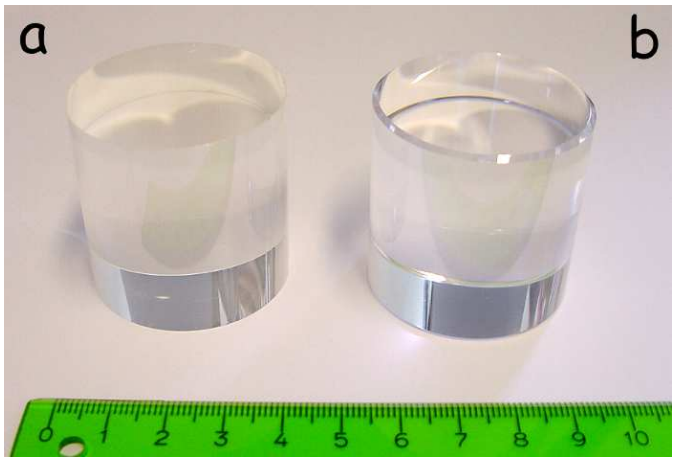

Figure 5.7: $CaWO_4$ crystals ($\varnothing = 40\,mm$; $h = 40\,mm$). Karat sample - K10 (a) and Russian sample - Rita (b).

Figure 5.8 shows the optical transmission as a function of wavelength of the crystals of different origin. A representative example is chosen for each crystal grower. Almost all measured samples from the Russian provider had a high

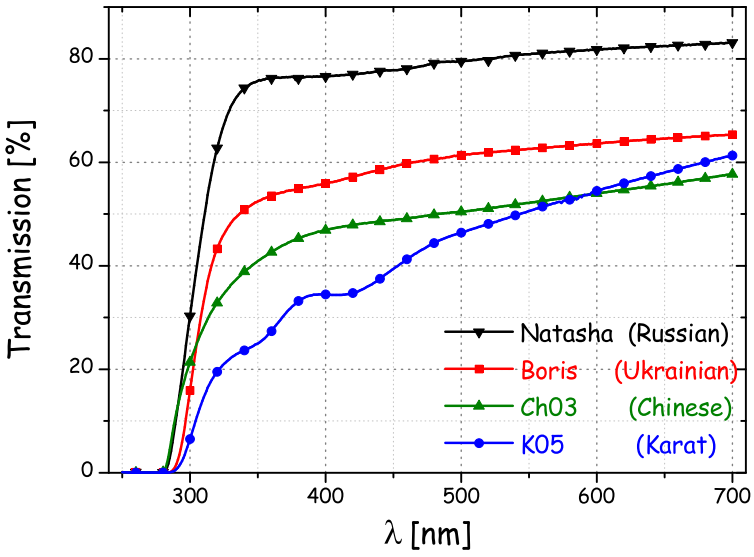

Figure 5.8: Comparison of the optical transmission of the crystals from different producers. For each crystal grower a representative example is presented. Maximum transmission due to the Fresnel refraction is $\simeq$83%.

transmissivity (> 70 % for the wavelengths above 350 nm). The measurements of the Ukrainian crystals showed significant variations in the transmission spectra (from below 15 % to above 50 % for wavelengths above 350 nm). These results are not unexpected since samples from this provider have obvious differences in their color varying from almost fully grey colored ones to transparent ones. Chinese crystals are without obvious coloring but the presence of small inclusions is noticeable in all samples. Finally, Karat crystals have a pronounced absorption in the region 320 - 450 nm due to their yellow color. However, the last delivery from this provider supplied us with colorless crystals (see K10 in Fig. 5.7a).
The vanishing transmission around 300 nm, present in all crystals, is due to the intrinsic absorption. It corresponds to the excitation of electrons from the filled valence band to the excitonic levels below the conduction band and with increasing energy these valence band electrons finally reach the conduction band.
Studies showed that Gd^{3+}, Dy^{3+}, Nb^{5+} doping improves the transmittance of $PbWO_4$ crystals in the short wavelength region, while Nb^{5+} doping makes the absorption cut-off sharper [Hua03]. As $CaWO_4$ crystals have the same crystal structure (scheelite) as $PbWO_4$, rare earth contamination present in the case of the Russian crystals could be an explanation for their higher transmission, especially below 450 nm.

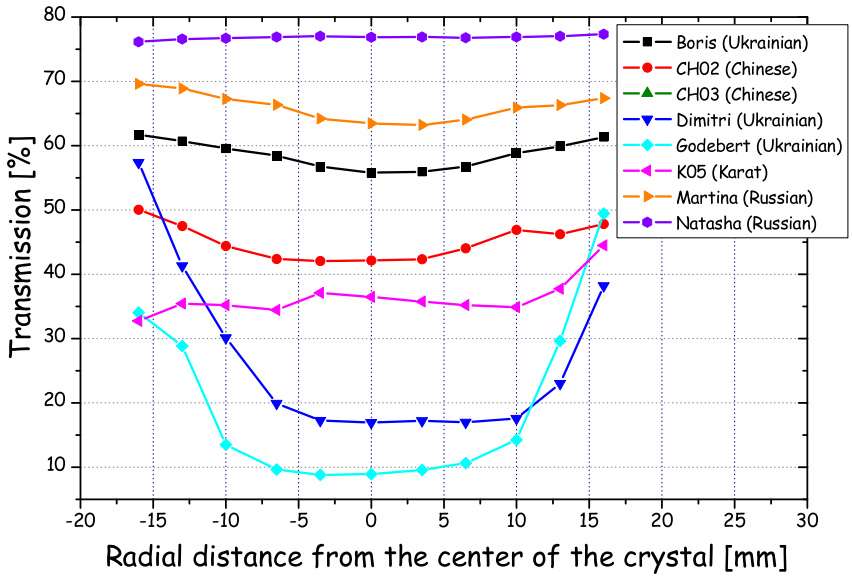

Figure 5.9: Change of the longitudinal optical transmission of the crystals along the radius of the crystal. On the X - axis the distance from the center of the crystal and on the Y - axis the measured optical transmission at 420 nm are plotted.

To check the uniformity and homogeneity of the optical characteristics of the crystals longitudinal measurements of the transmittance at 420 nm for several positions along their radius, were performed. Figure 5.9 shows some illustrative examples. In more than 60% of the measured crystals the central part of the crystal showed a lower transmittance. In the case of some of the Ukrainian crystals (like Godebert and Dimitri) this effect is highly pronounced. For the Russian crystals a significant improvement has been achieved. In the last five crystals a position dependance of the transmission was not observed (Crystal Natasha shown in Fig. 5.9).
A closer inspection of the shape of the transmission curves of the Russian crystals confirms their contamination with rare earths (see figure 5.10). Sharp absorption lines at 370 and 523 nm and one with a lower intensity at 655 nm can be ascribed to the transition from the $^4I_{15/2}$ ground state of Er^{3+} to higher 4f states, $^4G_{11/2}$,$^2H_{11/2}$ and $^4F_{9/2}$ respectively [Die68]. In the transmission spectrum of the

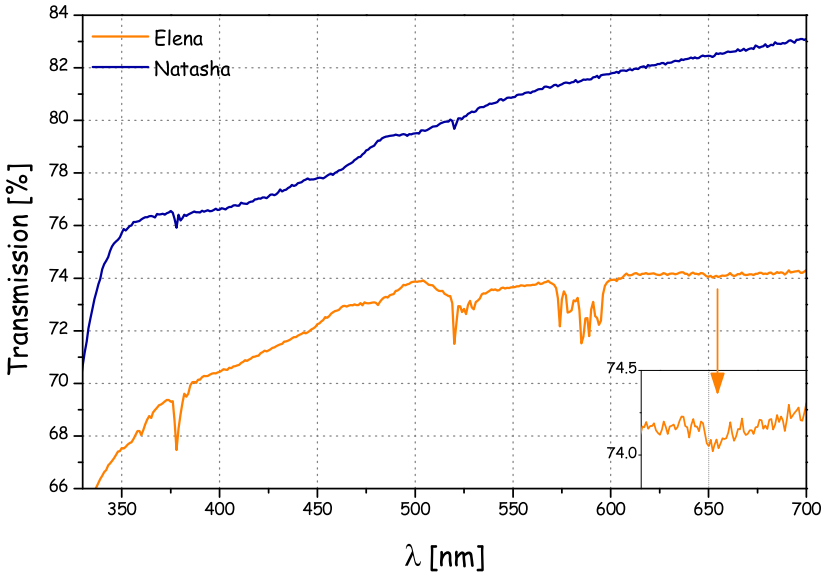

Figure 5.10: Enlarged parts of the optical transmission spectra of the two Russian crystals showing the presence of the rare earth impurities. Absorption lines at 380 nm and 523 nm are the fingerprints of the Er^{3+} contamination. In the case of the crystal named Elena an additional contamination due to Nd^{3+} is visible (526, and 583 nm).

crystal Elena additional absorption lines at 526, 583 nm are present. These are most probably due to $4f^3$ - $4f^3$ transition of Nd^{3+} ion (transitions from $^4I_{9/2}$ to $^2K_{13/2}$+$^4G_{7/2}$+$^4G_{9/2}$ and $^4G_{5/2}$+$^2G_{7/2}$ respectively) [Die68]. The recess between

400 and 450 nm in case of this crystal is presumably due to a Y^{3+} contamination. The ICP-MS analysis of a sample from this crystal showed in addition to Er, Nd and Y, a contamination with Gd of about 1 ppm (Appendix B, table B.2). Trivalent Gd has a singular position among all rare earth ions since it has no infrared or visible absorption or fluorescence, therefore contamination with this ion cannot be confirmed here.

5.1.3 Luminescence measurements

In order to better understand the differences in the luminescence properties of the crystals of different origin, a comparative study of their emission under different excitations was performed. Only a sample from the Ukrainian supplier (Conrad) and a sample from the Russian supplier (Berta) have been studied under X-ray and VUV excitation as crystals from the other two suppliers were available only after these measurements had been performed. A sample of Chinese origin (Ch01) was studied along with these two samples under UV excitation. All samples were cut to $5\times5\times1\,mm^3$ with all but the back surface (5×5 mm^2) optically polished. The back surface was kept rough in order to avoid reflections. Technical descriptions of the setups used are presented in the section 4.3.

UV excited luminescence

As stated in section 3.4 the following emission bands of interest have been reported for $CaWO_4$ crystals:

- 2.85 eV (435 nm) - the main (intrinsic) emission, excitons at the regular $[WO_4^{2-}]$ oxyanions,
- 2.35 eV (528 nm) - the emission of the centers of the WO_3 family (oxygen-vacancy related centers),
- 2.65 eV (468 nm) - at 77 K Pb^{2+} perturbed $[WO_4^{2-}]$ oxyanions.

These emission bands can be selectively excited:

- the excitation at 5 eV (250 nm) gives the main (intrinsic) emission,
- the excitation at 4.2-4.3 eV (290-295 nm) gives the emission of the oxygen-vacancy related centers,
- the excitation at 4.5-4.6 eV (270-275 nm) at 77 K gives the emission due to Pb^{2+} perturbed $[WO_4^{2-}]$ oxyanions.

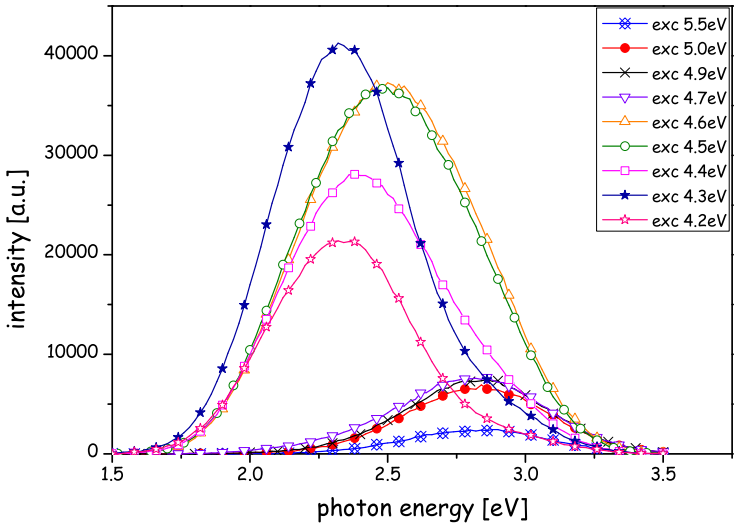

Figure 5.11: Emission spectra of the Ukrainian sample (Conrad) under different excitation energies measured at LHe temperature. Excitation at 5 eV gives the main intrinsic emission.

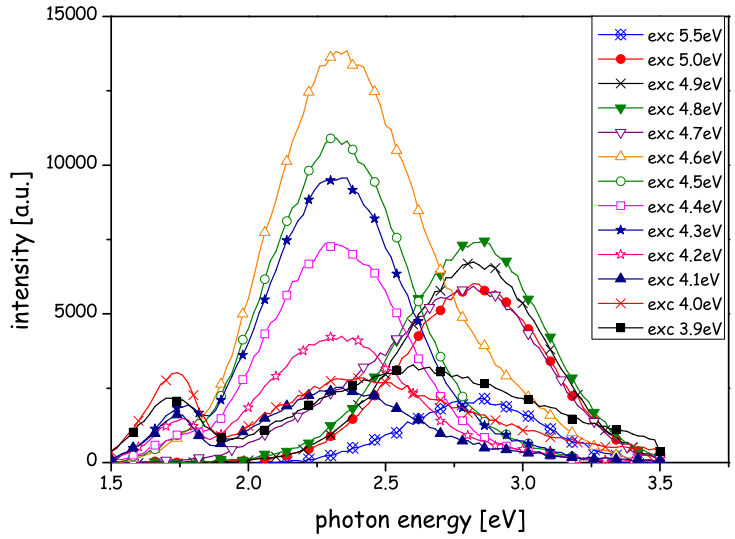

Figure 5.12: Emission spectra of the Russian sample (Berta) under different excitation energies measured at LHe temperature. Excitation at 5 eV gives the main intrinsic emission.

Series of spectra have been measured at LHe temperature, under the same experimental conditions at different excitation energies. Therefore, data of different crystals can be compared with each other. The excitation at 5 eV (which gives the main emission) was used as a reference.

Crystal Conrad (Ukrainian): In figure 5.11 the emission spectra of this crystal under different excitation energies are presented. The crystal obviously contains many oxygen vacancies, as the intensity of the 2.35 eV emission excited at 4.2-4.3 eV is large with respect to other two crystals (see Fig. 5.12 and Fig. 5.13). The emission band peaking at 2.5 eV is most efficiently excited near 4.5-4.6 eV and therefore is related to Pb^{2+}. This shows that this crystal contains a significant amount of lead.

Crystal Berta (Russian): From figure 5.12 it is clear that this sample contains much less or no lead (practically only 2.35 eV can be excited at 4.6 eV), but it has a significant number of oxygen vacancies. Beside that, it has a emission band in the red peaking at 1.7 eV, which is most probably related to a contamination by molybdenum. This emission can be most purely excited around 4.0 eV. The nature of the 2.65 eV emission excited at the same energies is not yet understood.

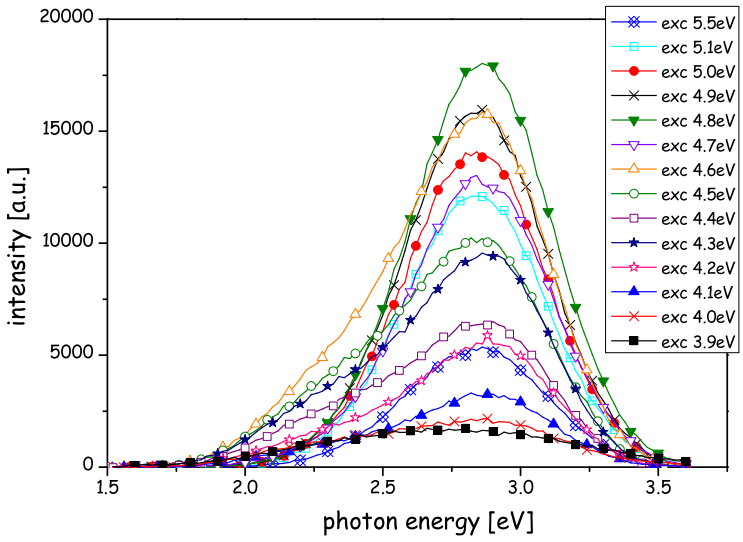

Figure 5.13: Emission spectra of the Chinese sample (Ch01) under different excitation energies measured at LHe temperature. Excitation at 5 eV gives the main intrinsic emission.

Crystal Ch01 (Chinese): This sample has a surprisingly low number of oxygen vacancies (near twice as low as in the crystal Berta), but it contains some centers, possibly impurities, whose emission spectrum looks like that of the main emission (see Fig. 5.13). This extrinsic emission can be excited in the whole energy region in particular at 4.6-3.9 eV, where the main emission is definitely not excited.

As illustrated, these measurements can be used for the examination of the properties of the crystals but still there is no absolute confidence about the total amount of certain impurities (especially lead). This is mainly due to the overlap of various emission bands at lower energies with respect to the main $CaWO_4$ emission at 2.85 eV. Only a comparison of the decay kinetics of samples with known doping of certain impurities with non-doped ones could give definite answer. Such measurements are planned in the near future.

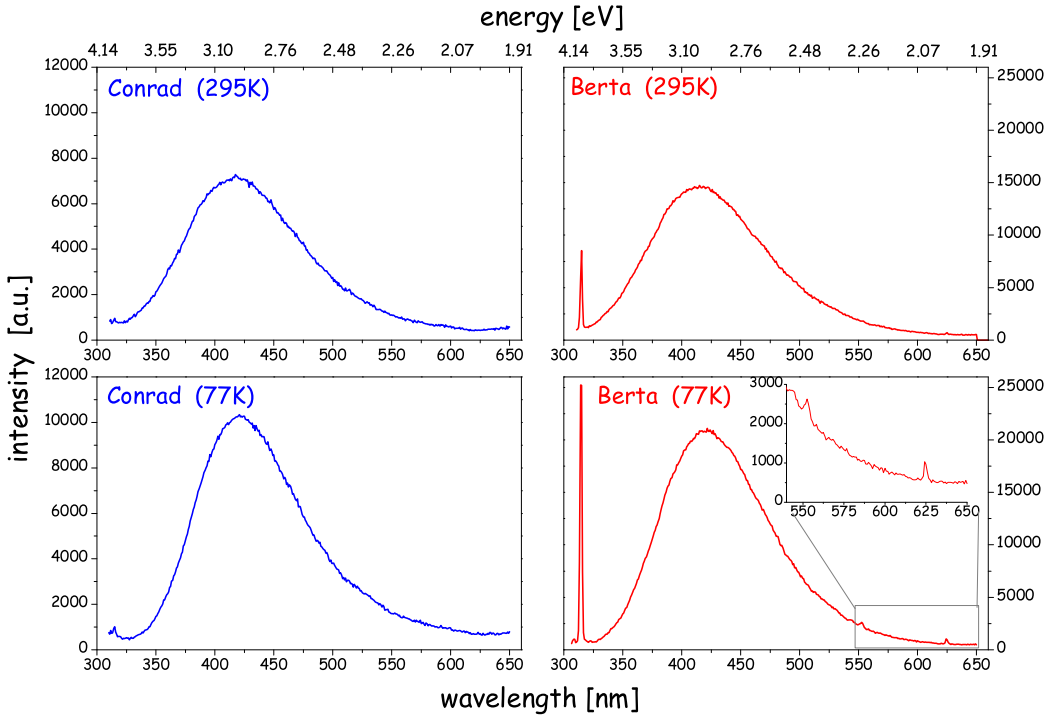

Figure 5.14: X-ray excited luminescence spectra of two $CaWO_4$ samples measured at 295 K (top) and 77 K (bottom). Left: Conrad (Ukrainian); Right: Berta (Russian).

X-ray excited luminescence

In the emission spectra of the sample from the Ukrainian supplier (**Conrad**) a broad band that is characteristic for the intrinsic emission of the tungstate [WO_4^{2-}] group was observed (Figure 5.14 - left). The broadening of the emission peak to the right can be explained by the presence of extrinsic emission.
The luminescence spectrum of the sample from the Russian supplier (**Berta**) showed additional line emissions due to the notorious contamination by rare-earth ions. The strong line at 313 nm ($\sim 3\,\%$ of total light yield at 77 K) in figure 5.14 - right corresponds to the $^6P_{7/2}$-$^8S_{7/2}$ transition of Gd^{3+} [Bla94]. Two other lines at 560 nm and 625 nm are most likely due to a radiative intraconfiguration transition of Er^{3+} and Eu^{3+} or Sm^{3+} ions, respectively. These conclusions are consistent with the data from the ICP-MS analysis (Appendix B.2).
As illustrated, measurements of X-ray excited luminescence can be used for the examination of the rare earth impurity content in the $CaWO_4$ crystals.

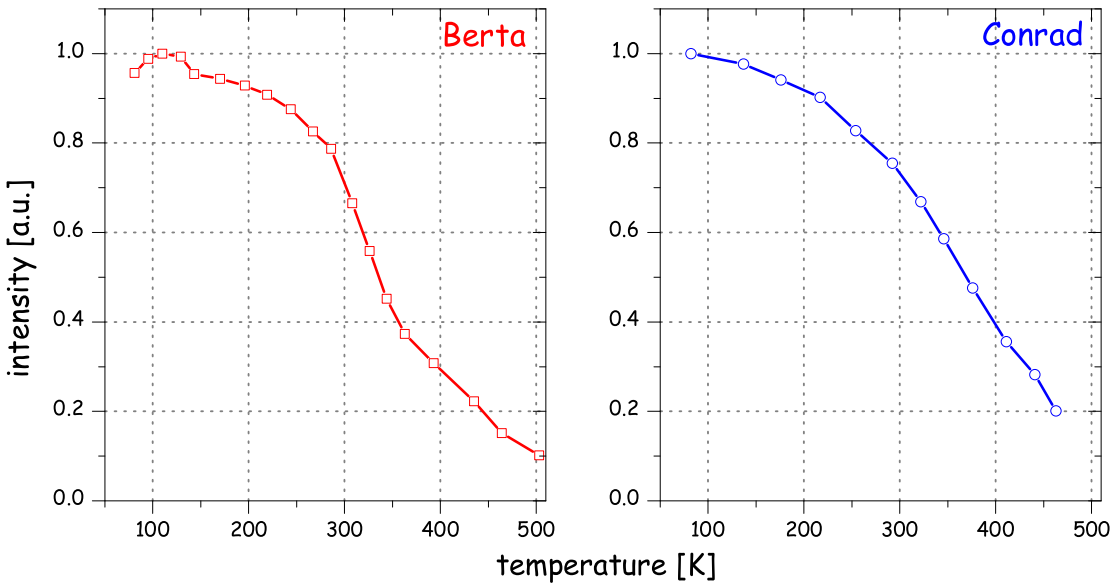

Figure 5.15: Temperature dependence of the integrated luminescence yield for X-ray excitation of two $CaWO_4$ samples. Left:Berta (Russian); Right:Conrad (Ukrainian).

A comparison of the temperature dependence of the integrated luminescence yield for X-ray excitation is shown in figure 5.15. The total light yield is temperature dependent increasing by more than 30% when cooling from room to liquid nitrogen temperature.

VUV excited luminescence

Further investigation of the temperature dependance of the light yield was done under VUV excitation. The emission spectra presented in Figure 5.16 were measured with the excitation energy fixed at $\simeq$30 eV ($\lambda_{exc} = 40\,nm$) for each measurement.

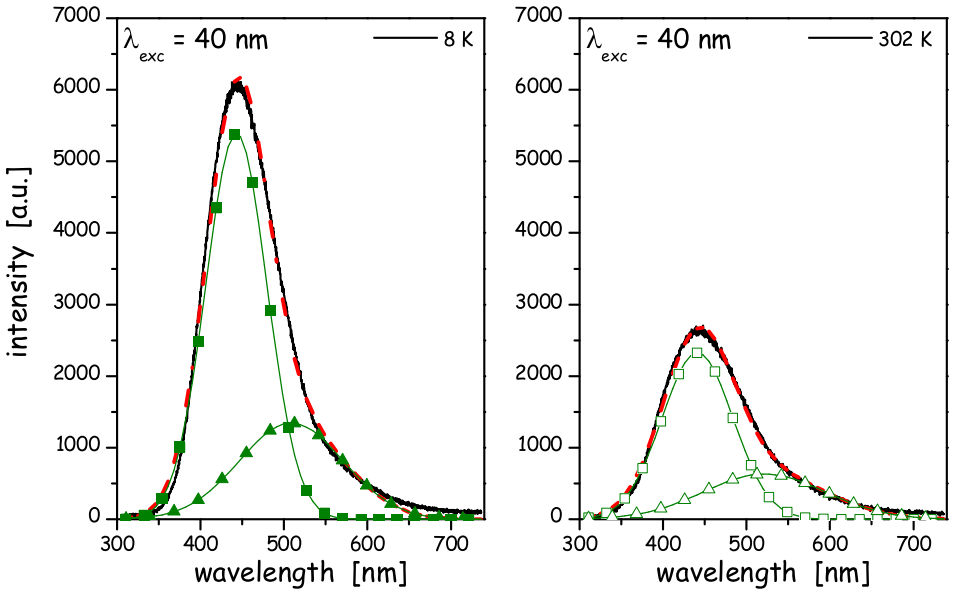

Figure 5.16: VUV excited emission spectra of the Ukrainian sample (Conrad). The black lines represent raw data measured at 300 K (right) and 8 K (left). Both spectra are deconvoluted using two Gauss distributions (dashed lines). □ - identifies intrinsic emission and △ - the extrinsic one. Closed symbols refer to the 8 K and open ones to the 300 K measurement.

As shown in figure 5.16, a temperature increase leads to a broadening of the emission bands and a decrease of the emission intensity. As previously mentioned, it is believed that $CaWO_4$ has a composite luminescence, i.e. in addition to the intrinsic also an extrinsic component can often be observed. To test this model and examine the behavior of the components with a change of the temperature a decomposition analysis was performed. Two-Gaussian decomposition of the $CaWO_4$ luminescence is widely accepted ([Gra75], [Nag98], [Kol02]) and was considered to be the most appropriate for the analysis in this work. The results of the deconvolution analysis are summarized in figure 5.17.
The absolute intensity of both emissions is increasing with decreasing temperature. The peak position of the intrinsic emission band almost coincides with the

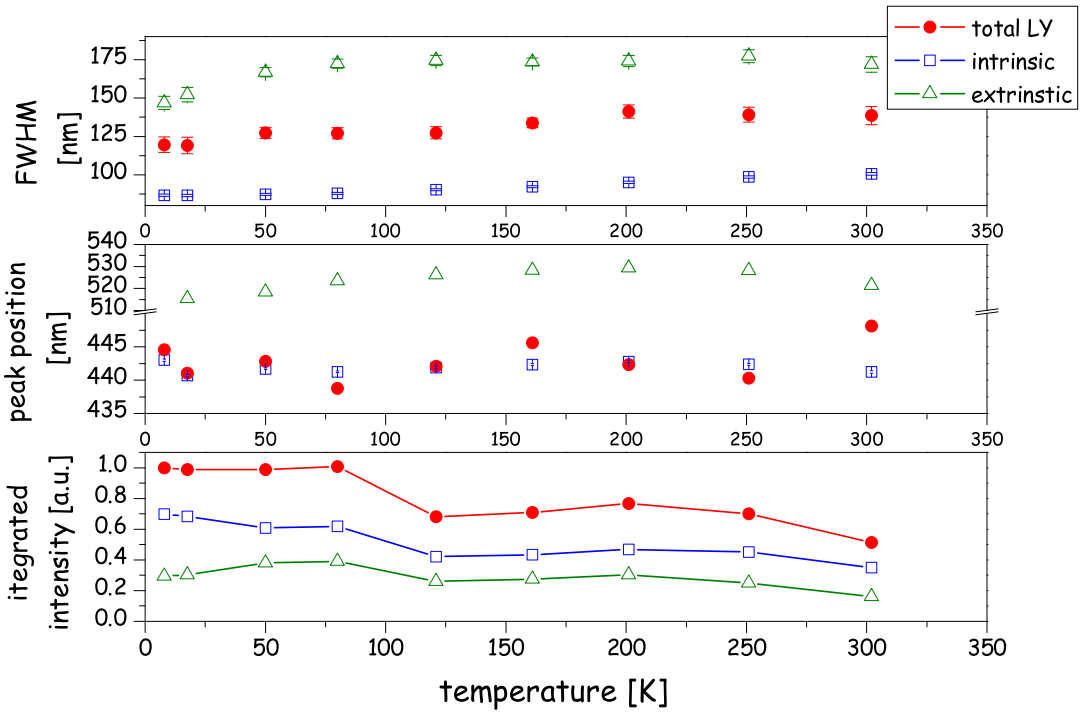

Figure 5.17: Temperature dependence of the integrated luminescence yield (bottom), the peak position (middle) and the full width half maximum - FWHM (top) under VUV excitation of a $CaWO_4$ sample (Conrad). For labels see legend.

maximum of the luminesce spectrum. Due to a strong overlap of the individual Gaussians the uncertainty resulting from the deconvolution procedure does not allow a conclusion on a possible variation of the position of the extrinsic emission peak with temperature. However, as this band gives a small (less than 30 percent) contribution to the total emission intensity, the effect on the shape of the luminescence spectrum is minor.
Figure 5.18 depicts the emission spectra of both measured samples. It shows that no obvious differences can be seen in the shape of the spectra.

Excitation spectra

For the measurement of the excitation spectra, the emitted photon energy is kept constant and corresponding curves display luminescence intensity as a function of exciting photon energy.
In figure 5.19 the excitation spectra of the 420 nm emission measured at 300 K and 8 K are presented for the crystal of Russian (**Berta**) and Ukrainian (**Conrad**)

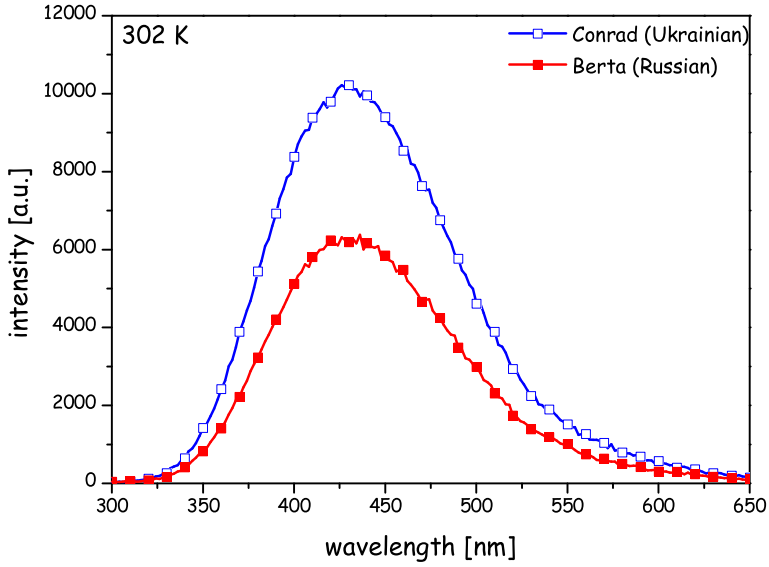

Figure 5.18: Emission spectra of the Ukrainian sample (open symbols) and the Russian sample (closed symbols) under VUV excitation (40 nm) measured at 300 K.

origin.
A low luminescence intensity in the region of 9-14 eV, observed in the excitation spectra of both samples, is the result of insufficient purity of the surfaces [Nag98]. Electronic excitations in the energy region of 5-7 eV are most effective for the emission of self-trapped excitons at 2.85 eV. The recombination emission of $CaWO_4$ is effectively excited by photons of an energy greater then 7 eV. In the region of 13-14 eV the emission in both samples is excited by single e-h pairs [Nag98]. In the region 14.5 -21 eV the intensity increases. This increase occurs in the same region as the rise of the fundamental reflection (absorption) and it is most probably related to the multiplication of electronic excitations [Nag98].

Reflectivity spectra

In the case of the reflection spectra measurements, the sodium salicylate luminescence excited by the VUV light reflected from the sample is measured instead of direct reflection. The axes of the reflection channel and of the exciting beam are at an angle of 35°. The reflectivity spectrum displays the intensity of the reflected light as a function of photon energy of excitation.
For both samples the reflection spectra for the intrinsic emission, measured at both 300 K and 8 K in the region of 4-20 eV, are presented in figure 5.20. The reflection maximum at 5.9 eV undoubtedly is caused by the creation of molecular

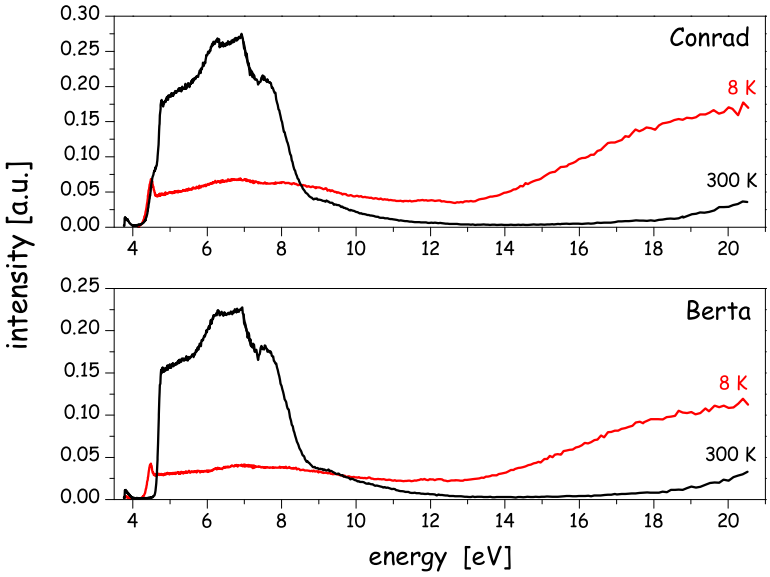

Figure 5.19: Excitation spectra of the intrinsic luminescence at $\lambda = 420$ nm measured at 300 K and 8 K. Top: sample Berta (Russian); Bottom: sample Conrad (Ukrainian).

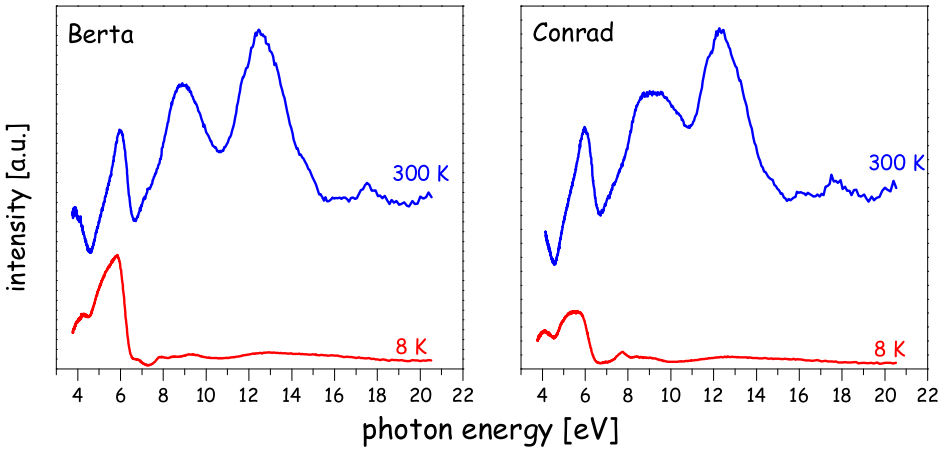

Figure 5.20: Reflection spectra of the intrinsic luminescence measured at 300 K and 8 K. Left: sample Berta (Russian); Right: sample Conrad (Ukrainian).

excitons [Gra75]. This peak is accompanied by two groups of bands, each group containing three broad main reflection maxima which strongly overlap. These peaks can be attributed to the transitions within the WO_4^{2-} molecular anion as reported in the table 5.1 [Gra75].

Table 5.1: Assignment of the measured reflectivity peaks with electronic transitions within the oxyanion WO_4^{2-} [Gra75].

Transition	WO_4^{2-} [eV]
$t_1 \rightarrow 2e\,(^1A_1 \rightarrow^1 T_2)$	5.9
$t_1 \rightarrow 4t_2\,(^1A_1 \rightarrow^1 T_1)$	7.6
$t_1 \rightarrow 4t_2\,(^1A_1 \rightarrow^1 T_2)$	8.3
$3t_2 \rightarrow 4t_2\,(^1A_1 \rightarrow^1 T_2)$	9.4
$2t_2 \rightarrow 2e\,(^1A_1 \rightarrow^1 T_1)$	11.7
$2t_2 \rightarrow 2e\,(^1A_1 \rightarrow^1 T_2)$	12.3

5.1.4 Scintillation properties

A simple photomultiplier tube (PMT) setup described in section 4.1 and sketched in Fig. 4.1 was used in order to compare the scintillation properties of the crystals. In figures 5.21 - 5.25 the pulse height normalized to the response of one of the Ukrainian crystals (Boris) versus the resolution of the ^{137}Cs line is plotted. The energy resolution R is defined in terms of the full width at half maximum (FWHM) of the peak (H_0) rather than its standard deviation. For a Gaussian shape, FWHM is 2.35 times the value of the standard deviation. The statistical broadening of the peak usually dominates other potential sources for resolution loss. In this case the variation of the resolution with gamma ray energy can be expressed as:

$$R \equiv \frac{FWHM}{H_0} = k \cdot \frac{\sqrt{E}}{E} = \frac{k}{\sqrt{E}}; \tag{5.1}$$

where k is a constant of proportionality. The crystals have been measured as delivered before any mechanical or thermal treatment. In order not to contaminate the crystal surface no optical coupling was used except if it is explicitly noted. The first four graphs correspond to crystals from different producers while the last summarizes all measured crystals.
The first delivery of the crystals from the Ukrainian source contained three crystals with both good resolution and high light output (Alexej III, Boris and Conrad). The other two crystals contained a significant amount of inclusions in the central part of the crystal. The second delivery consisted of low quality crystals.

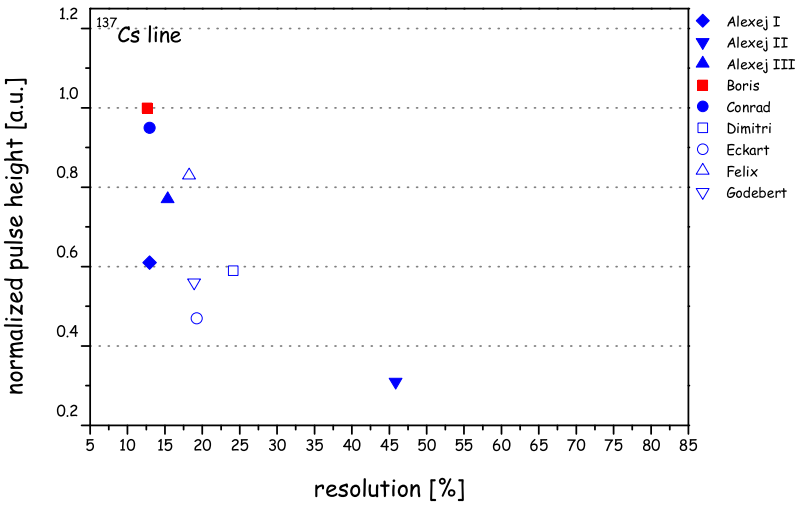

Figure 5.21: Scintillation properties (light yield, energy resolution) of the crystals from the Ukrainian source. Closed symbols correspond to the first, open ones to the second delivery of crystals.

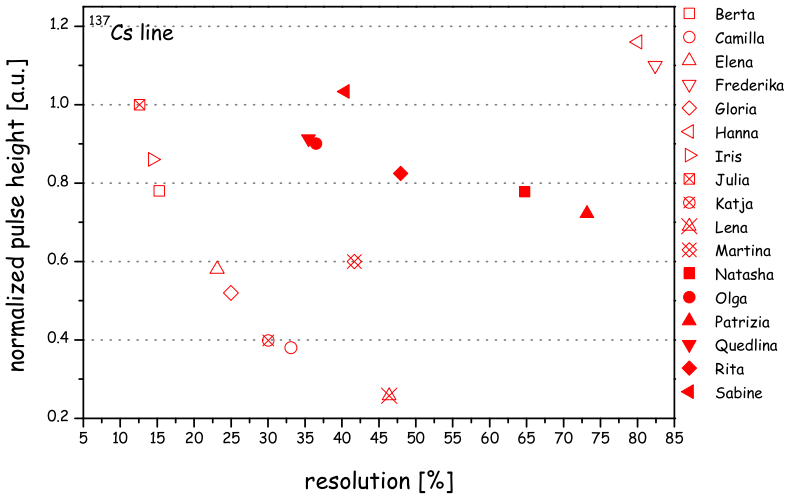

Figure 5.22: Scintillation properties (light yield, energy resolution) of the Russian crystals delivered in 2002 (open symbols), in 2003 (crossed symbols) and in 2004 (solid symbols).

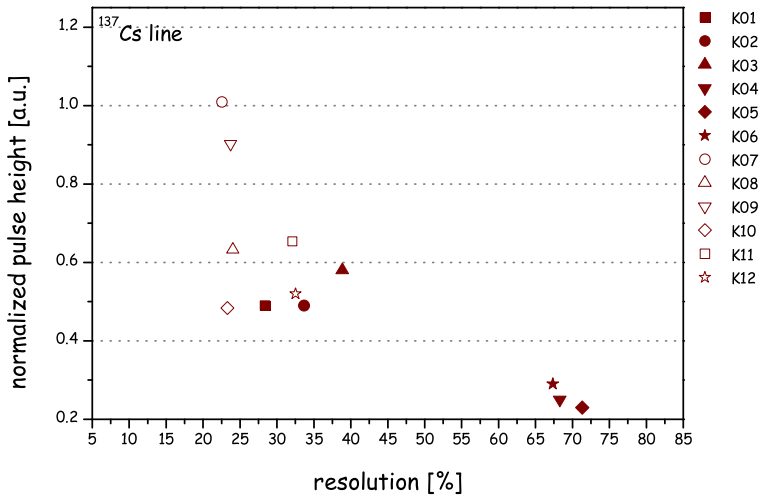

Figure 5.23: Scintillation properties (light yield, energy resolution) of the crystals from the Karat company. Closed symbols correspond to the first, open ones to the second delivery of crystals.

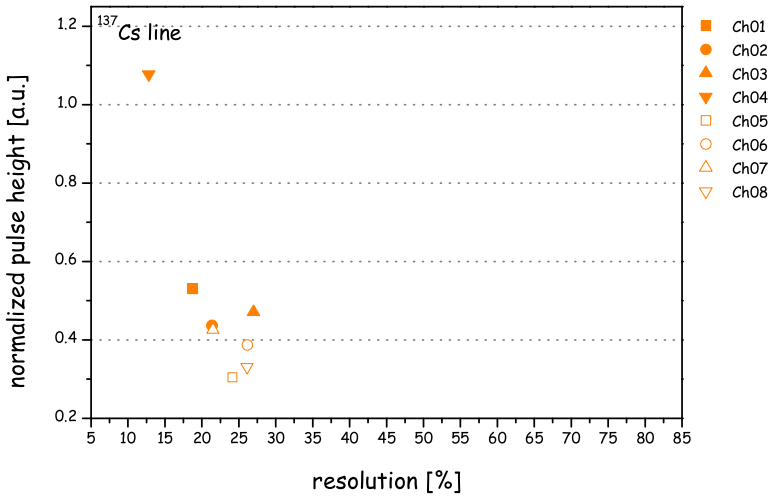

Figure 5.24: Scintillation properties (light yield, energy resolution) of the Chinese crystals. Closed symbols correspond to the first, open ones to the second delivery of crystals.

All of them were slightly colored with visible defects in the central region. Moreover, the radiopurity of these crystals was bad (see section 5.1.1). As there was no possibility to influence the crystal growing process, the decision was made to discard this crystal grower.
The quality of the Russian crystals significantly improved with time. All crystals of the last delivery had high scintillation light yields (see Fig. 5.22) and rather similar properties. Otherwise the bad resolution of some of these crystals due to a slightly different shape (chamfering of the edges) will be discussed latter.

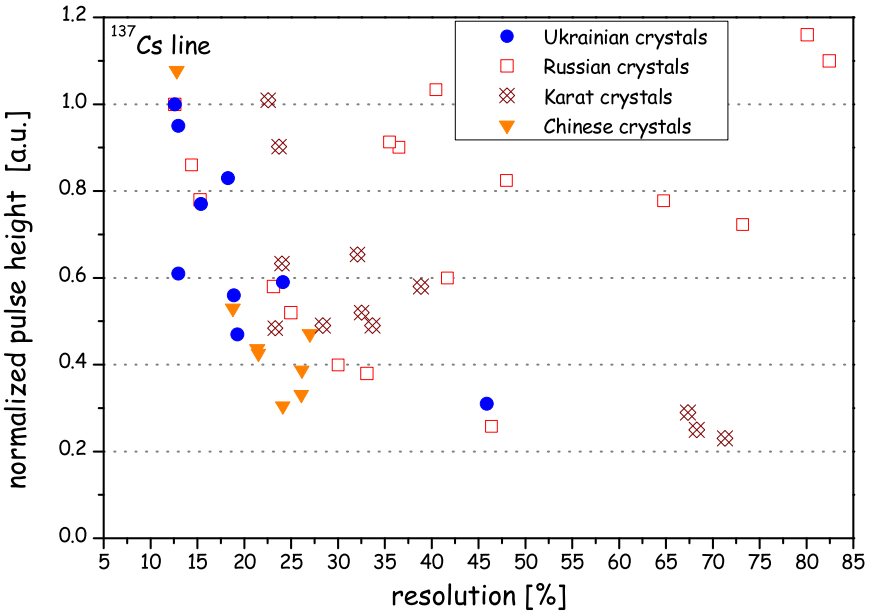

Figure 5.25: The scintillation quality of the crystals from different producers. On the X-axis the resolution of the ^{137}Cs line is plotted while on the Y-axis normalized light pulse height of the line is given.

Significant improvement of the scintillation response of the Karat crystals have been achieved by providing the company with high quality raw material and by after-growth annealing (see figure 5.23 second delivery). The first delivery from this company consisted of crystals of pronounced yellow color while in the next iteration colorless crystals have been produced.

The improvement of the quality of the crystals coming from China is still ongoing and preliminary results from the first two crystal deliveries are presented in figure 5.24.

The Ukrainian crystal Boris was used to check the linearity of the scintillation response. ^{241}Am (59.6 keV), ^{137}Cs (661.7 keV), ^{22}Na (511 and 1274.5 keV) and

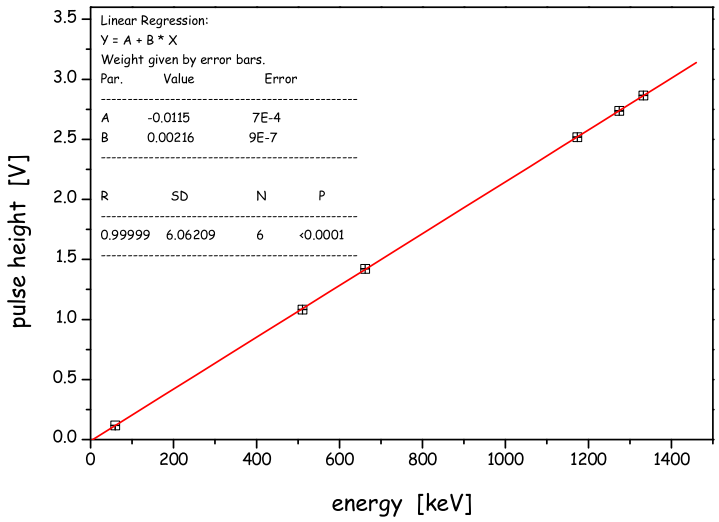

Figure 5.26: Linearity of the scintillation response of the big (Ø=40 mm, h=40 mm) $CaWO_4$ single crystal (Boris). On the X-axis energy of the γ-rays used for the irradiation is presented while on the Y-axis the measured pulse height is plotted.

^{60}Co (1.173 and 1.332 MeV) γ-sources were used for the irradiation and the result is presented in figure 5.26. Perfect linearity is observed in the region from 60 keV up to 1.33 MeV.
The energy resolution should be inversely proportional to the square root of the gamma-ray energy (see equation 5.1). The logarithm of two sides of equation 5.1 gives:

$$\ln R \;=\; \ln k - \frac{1}{2}\ln E; \tag{5.2}$$

Therefore, a plot of $\ln R$ versus $\ln E$ should be a straight line with slope of $-1/2$. Figure 5.27 shows a plot of experimentally determined resolution values for crystal Boris as a function of the gamma-ray energy. The corresponding linear fit gives a slope value of -0.48 ± 0.01 in good agreement with a purely statistical broadening.

In order to increase the light collection efficiency and to compare the response of the big $CaWO_4$ crystal with that of a commercial NaI(Tl) crystal, an immersion oil [2] was used for the optical coupling of the crystal to the PMT. Figure 5.28 shows spectra measured with these two crystals. As can be seen, the resolution obtained for this particular sample of $CaWO_4$ is comparable with the NaI(Tl)

[2] of refraction index 1.6

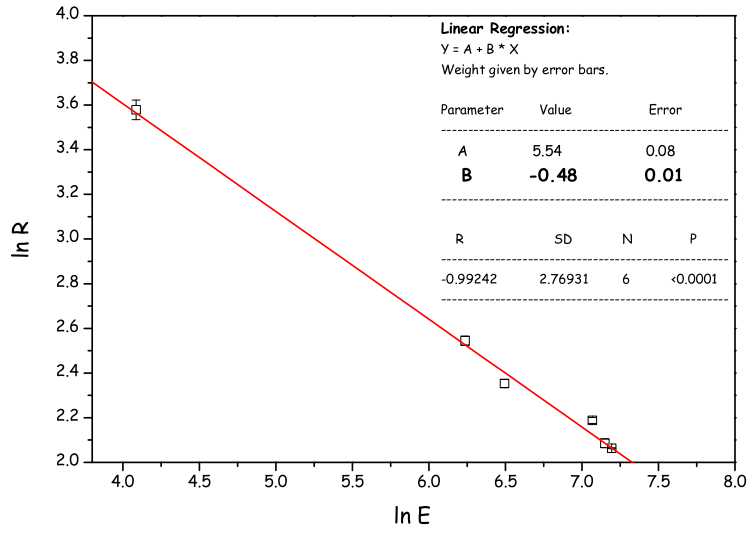

Figure 5.27: Dependence of the resolution of γ-lines on their energy measured with a $CaWO_4$ (crystal Boris). The linear fit gives a slope of -0.48 ± 0.01.

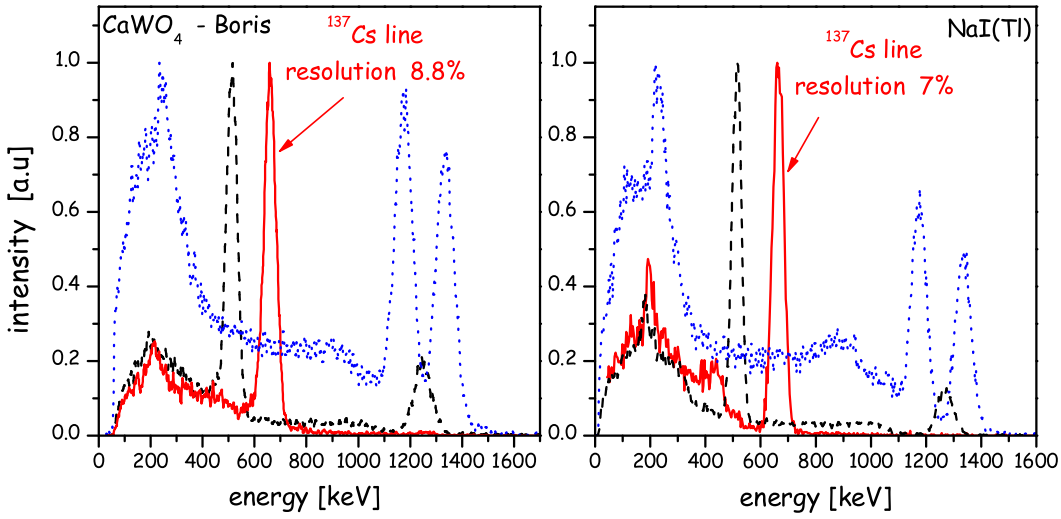

Figure 5.28: Gamma ray spectra of ^{137}Cs (full line), ^{22}Na (dashed line), and ^{60}Co (dotted line) measured with $CaWO_4$ (left) and with a NaI(Tl) crystal (right) of approximately the same size and shape.

resolution.

The peak-to-Compton ratio is usually defined as the ratio of the counts in the highest bin of the photopeak to the counts in a typical channel of the Compton continuum associated with that peak[3]. The ratio is conventionally quoted for the 662 keV or the 1332 keV gamma line of ^{137}Cs and ^{60}Co, respectively, and is a measure of the combined effects of detector energy resolution and photofraction. Because of its high effective Z value, the photofraction for the gamma-ray absorption is high for $CaWO_4$ which results in a very good peak-to-Compton ratio. The measured value of the peak-to-Compton ratio for this sample of $CaWO_4$ is 9.7 while a value of 6.6 was measured with the NaI(Tl) crystal. Unfortunately,

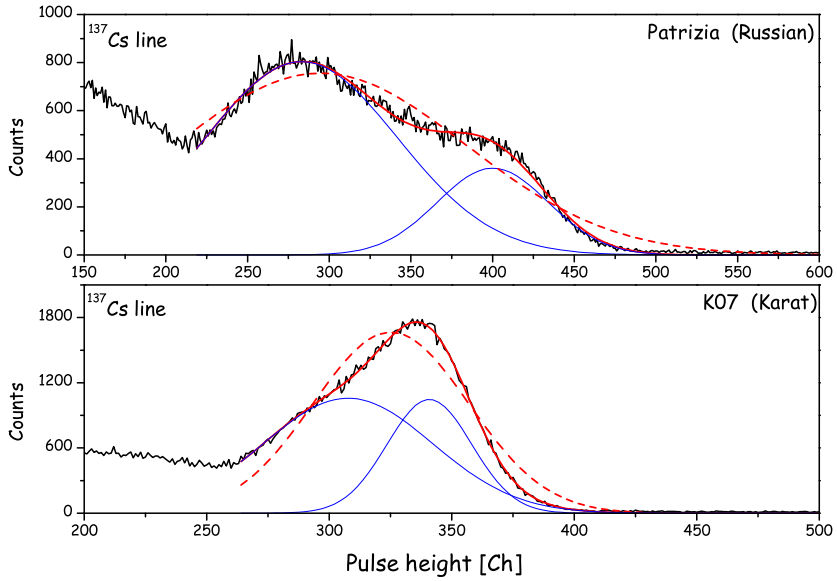

Figure 5.29: Doublet structure of ^{137}Cs line recorded with one of the Russian crystals (Patrizia) and one of the Karat crystals (K07).

not all of the $CaWO_4$ samples, measured up to now, showed such good scintillation properties. The largest surprise came from some of the Russian and Karat crystals which, although having high light yields, showed extremely poor resolution. The 662 keV ^{137}Cs gamma lines from two representative examples are shown in figure 5.29. It is evident from this figure that the decomposition

[3]This sample of the continuum is to be taken in the relatively flat portion of the distribution lying just to the left of the rise toward the Compton edge. Officially, this region is precisely defined, in ANSI/IEEE standards, for the HPGe detectors as the interval between 358 to 382 keV for the 662 keV gamma rays from ^{137}Cs.

into two Gaussians gives a much better fit to the measurement than the fit to a single Gaussian as would be expected. This effect can be partially explained with geometrical trapping of light inside of the crystal as will be shown later (see section 5.2.1).

5.1.5 Annealing of the $CaWO_4$ crystals

After-growth heat treatment of crystals can have a significant influence on their scintillation properties. In order to understand differences between the properties of crystals of different origin also their treatment after being grown was compared. A low temperature (300° - 500° C) annealing is usually performed

Figure 5.30: Photoelasticity photos of four $CaWO_4$ crystals using white light. From left to right, photos of Boris (Ukrainian), Rita (Russian), K08 (Karat), and Ch08 (Chinese) are shown.

to reduce stress inside the ingot and therefore prevent breaking of the crystals during cutting and polishing. This process was used for the production of all but the Chinese crystals. The presence of the fringe patterns on the photoelasticity images of Karat and Chinese crystals indicates residual stress inside the crystals[4] (see Figure 5.30). The fact that the Chinese crystal was not annealed might be an explanation for residual stress. In the case of the Karat crystals the annealing procedure was applied and a possible explanation for the residual stress might be a high non-uniformity of the temperature distribution within the crystal during the annealing process.
Russian crystals delivered in the year 2004 as well as some earlier ones were after being cut from ingots and shaped again annealed at higher temperatures (1100° C) in air in order to fill oxygen vacancies. As these crystals showed a favorable quality, possible improvement of the crystal quality through the annealing procedure was tested. Special care was taken to prevent implantation of impurities during that process. Therefore, the annealing procedure was done in

[4]Photoelasticity is a method of examining transparent polymer models of structures etc. to isolate stress concentrations and other weak zones. The object is placed between crossed circular polarizing filters and force is applied. The technique also enables residual stress to be shown in transparent objects.

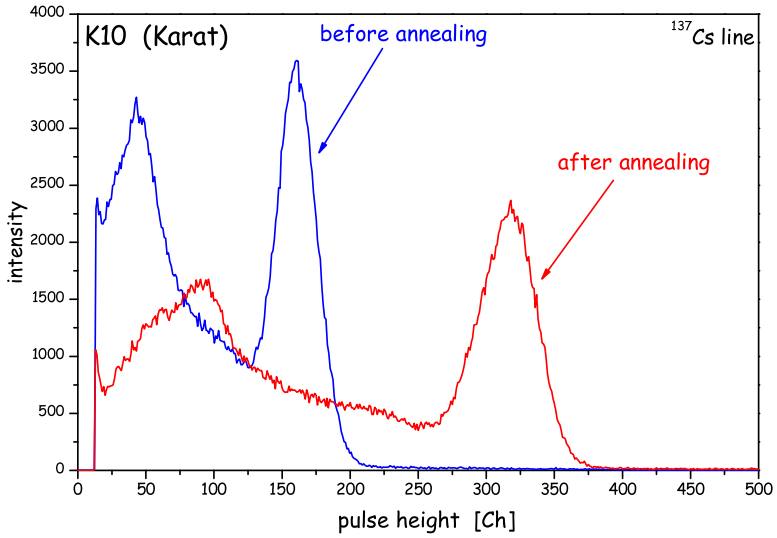

Figure 5.31: ^{137}Cs spectra measured before and after applying the annealing procedure described in the text to one of the Karat crystals (K10).

oxygen flow. The crystal was slowly warmed up to 1150° C and kept at this temperature for 5 days before being cooled down back to room temperature within two days. Karat crystal K10 was used for this test. This crystal had a normalized pulse height[5] of less then 0.50 (see figure 5.23). ^{137}Cs spectra of this crystal before and after annealing are shown in figure 5.31. The residual stress could be slightly reduced but still proved to be present. The annealing procedure is still under optimization in order to get a higher uniformity of temperature. But as seen in Fig. 5.31 it can significantly improve the response of the scintillating $CaWO_4$ crystals (pulse height doubled and resolution improved from $\simeq 30\%$ to $\simeq 20\%$).

5.2 Light collection and detector module optimization

Two effects arise in scintillation detectors that can lead to a reduced light collection: optical self-absorption within the scintillator and losses at the scintillator surfaces. Self-absorption is usually not a significant loss mechanism in the case of colorless crystals. Therefore, the uniformity of the light collection normally depends primarily on the conditions at the scintillator surface.

[5]The pulse height is normalized to the response of the Ukrainian crystal Boris.

The light collection conditions affect the energy resolution of a scintillator in two distinct ways. First, the statistical broadening will increase as the number of scintillation photons that contribute to the measured pulse is reduced. Second, the uniformity of the light collection determines the variation of the signal amplitude as the position of the radiation interaction is varied throughout the scintillator. Position dependence of light collection produces additional broadening.
Only a fraction of the emitted light will be finally detected by the light detector. The first limiting factor is the total internal reflection at the crystal surface which leads to light trapping. For $CaWO_4$ with its high index of refraction light trapping is very important. A second factor is the light collection efficiency which is determined by the geometry and efficiency of the reflector system and the absorption efficiency of the light detector. The third factor is the efficiency of the light detector to convert absorbed light into a measurable signal.

5.2.1 Light trapping

To study the effect of trapped light due to total internal reflection at the crystal surface the following procedure was applied to the examined $CaWO_4$ crystals.

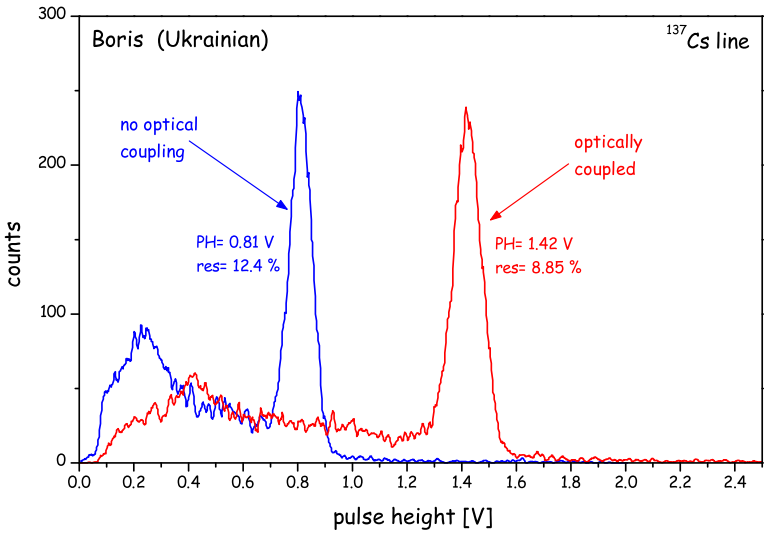

Figure 5.32: Comparison of ^{137}Cs spectra measured without optical coupling and with a immersion oil used to optically couple the crystal to the PM tube.

A sample was measured twice, first without any optical coupling, while a second measurement was made using immersion oil for optical coupling of the crystal to the PMT. The geometry of the rest of the setup was kept unchanged. Figure

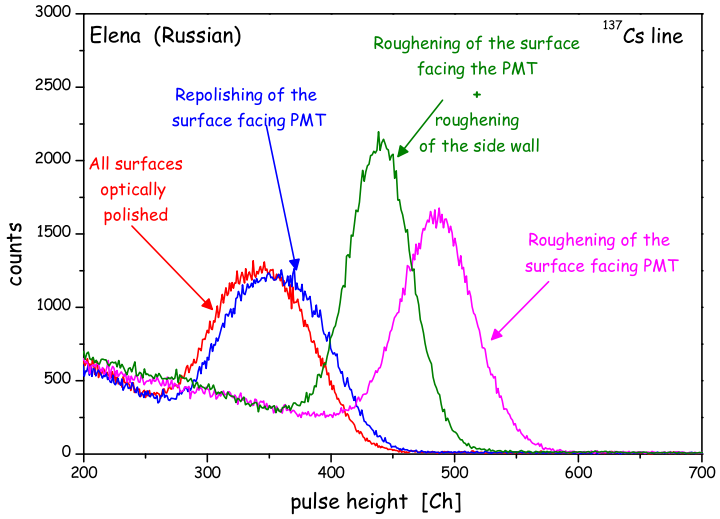

Figure 5.33: The effect of roughening of the crystal surface on the light collection efficiency demonstrated by the pulse height spectrum of ^{137}Cs.

5.32 shows an increase of more than 70% in the pulse height and improvement of the resolution from 12.4% to 8.8% in the case of the optically coupled crystal. For the CRESST Phase II detector modules optical coupling is not an option, instead to minimize the effect of light trapping the crystal surfaces were roughened. The best result (see Fig. 5.33) was obtained with all surfaces polished to optical quality except the one facing the PM tube.
Roughening of the surface of the absorber of the phonon detector might possibly lead to a degradation of the signal quality. This is due to the increase of the effective surface produced that way. This translates into a lower volume to surface ratio which might cause additional inelastic scattering of non-thermal phonons on the surface before being absorbed in the film and might therefore decrease the time required for thermalization [Kna85]. For a roughness of about 10 μm no effect on the phonon channel was observed in a test run at Gran Sasso. Therefore the roughening procedure was implemented as a final step in the detector preparation process.
A significant improvement of resolution was achieved with the roughening, especially in the case of crystals that showed a doublet structure of photo lines (see Fig. 5.29). The light collection efficiency was increased and became more homogenous. Figure 5.34 shows the ^{57}Co 122 keV gamma line[6] recorded in two

[6]The 122 keV line was isolated using the phonon detector pulse height spectrum which shows much better energy resolution. The response of the light detector for the selected pulses thus represents the light detector spectrum for the 122 keV line.

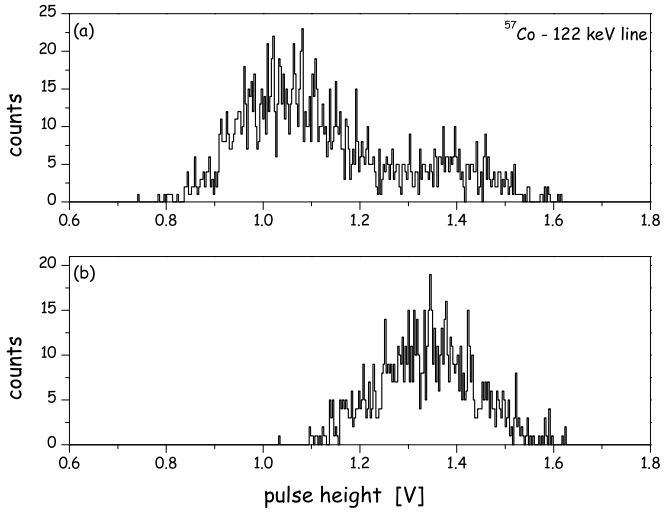

Figure 5.34: The effect of roughening of the crystal surface on the energy resolution. ^{57}Co 122 keV line recorded with the light detector in the Gran Sasso setup. (a) optically polished surface facing the light detector, (b) the same detector module but the crystal surface facing the light detector was roughened (10 μm).

subsequent runs in the Gran Sasso setup. Between these measurements the crystal surface facing the light detector was roughened.

5.2.2 Optimization of detector module

The detector modules were designed using the experience gained in the first phase of the CRESST experiment. In figure 5.35 a sketch of the design is shown [Fra02]. In order to optimize the light collection efficiency a series of different measurements has been performed. The reflector system surrounding the scintillating crystal should be as efficient as possible and the presence of non-reflective materials should be minimized. Additionally, any non-scintillating material inside the detector module should be avoided as this can lead to a potentially dangerous background. Namely, the daughter nucleus of alpha decays of nuclei implanted in the surrounding material might reach the scintillator while the α is absorbed in the surrounding material. The recoil nucleus would lead to a phonon signal with associated light signal typical for the recoil of a heavy nucleus[7], and therefore might mimic a WIMP signal.

[7]The energies of the recoiling heavy nuclei reach up to 104 keV and their low light output when hitting the $CaWO_4$ crystal may mimic a WIMP signal.

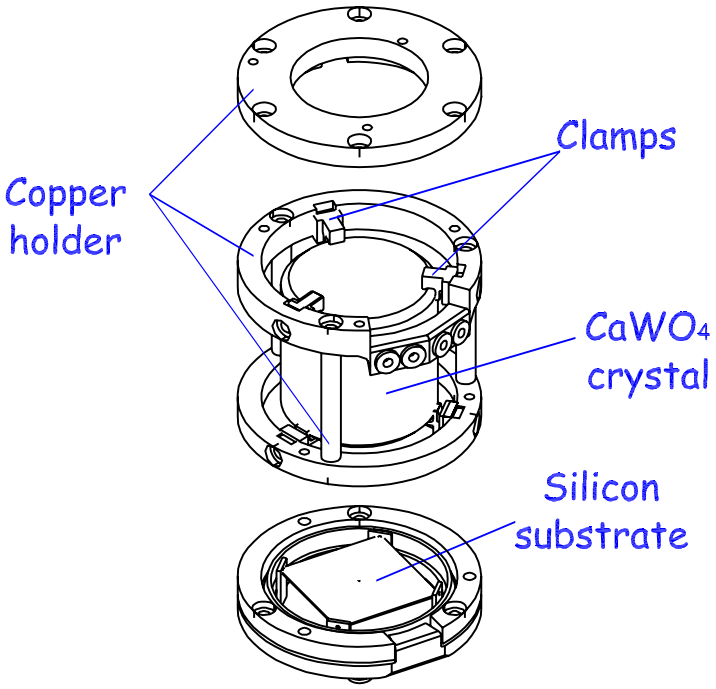

Figure 5.35: Exploded view of the detector module with main parts indicated [Fra02]. The light reflector surrounding the detectors is not shown.

Reflectors

As discussed before, any improvement in light collection efficiency might lead to a substantial increase in sensitivity of the CRESST experiment. Therefore, it is very important to choose the detector holder materials carefully. A series of measurements of the light collection efficiency for different reflecting materials have been performed. Figure 5.36 shows a comparison of the results obtained for the different reflectors. The best light collection was obtained with a new version of the high reflectivity polymeric multilayered foil (VM2002)[8]. In the test runs in the Gran Sasso setup an older version of this foil was used (VM2000)[9].
The deposition of dust particles often contaminated with Rn and its radioactive daughter nuclei is favored on materials that have electrostatically charged surfaces which is usually the case for plastic materials. Therefore, polymeric foil might be a potential source of no-light events, resulting from alpha decays on its surface. However, it was found that the support layer of these foils is made of Polyethylenenaphthalate (PEN) which scintillates as was confirmed with an open ^{241}Am source (5.5 MeV alphas). The luminescence properties of both foils were tested at the SUPERLUMI station under VUV excitation (for details of the setup see section 4.3). The measured excitation and emission spectra of the foils,

[8] 3M Radiant Mirror Film VM2002
[9] 3M Radiant Mirror Film VM2000

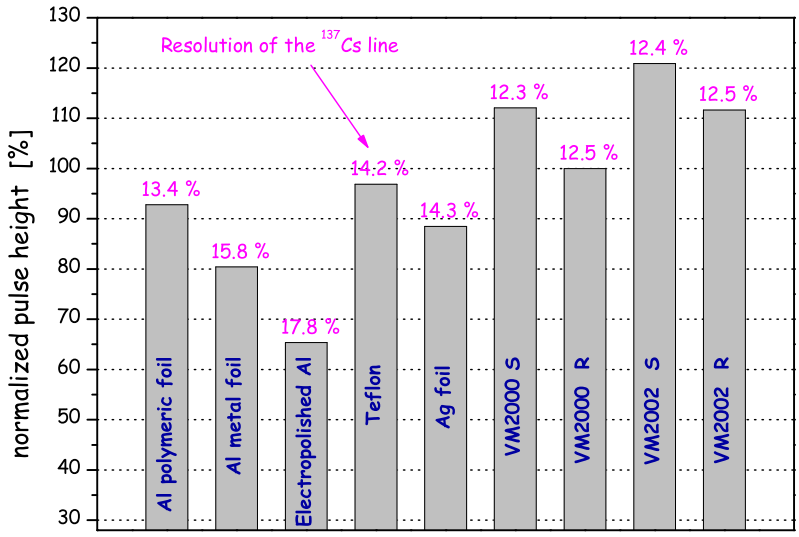

Figure 5.36: Comparison of pulse height and resolution of ^{137}Cs gamma line using different reflective materials. On the Y-axis the pulse height normalized to that obtained using the foil already tested in the Gran Sasso setup (3M foil - VM2000R) while the corresponding resolutions are given above the bars. **R** and **S** indicates whether the reflective or the support layer side is facing the crystal in the case of multilayered polymeric foils.

both at room and liquid He temperature, are shown in figure 5.37. At T = 9 K the integrated light yield of the new foil is by a factor of 1.4 higher compared to the old one. The emission band overlaps with the intrinsic emission of the $CaWO_4$. A direct comparison of light yields of a $CaWO_4$ sample and the foils is not possible due to their significant difference in the geometry.
The reflectivity spectra both for the scintillating and non-scintillating sides of VM2000 foils were measured at a fixed angle of 45° using the spectrophotometer SFM25 (KONTRON Instruments). The results are presented in figure 5.38 and for comparison the reflectivity of aluminium and silver foils are given. A reflectivity $> 95\%$ was measured in the region 400 - 800 nm for both sides of the foil. A sharp absorption edge appears at 390 nm for the non-scintillating side while it is slightly shifted to lower wavelengths in the case of the scintillating support layer. As the emission band of $CaWO_4$ extends into this region, the lowering of the overall reflectivity is compensated by the shift of the absorption edge in the case of the support layer side.
The use of the scintillating foil would significantly reduce the area of non-scintillating material within the module and therefore reduce the production of possibly dangerous background. Therefore, the comparative test was performed

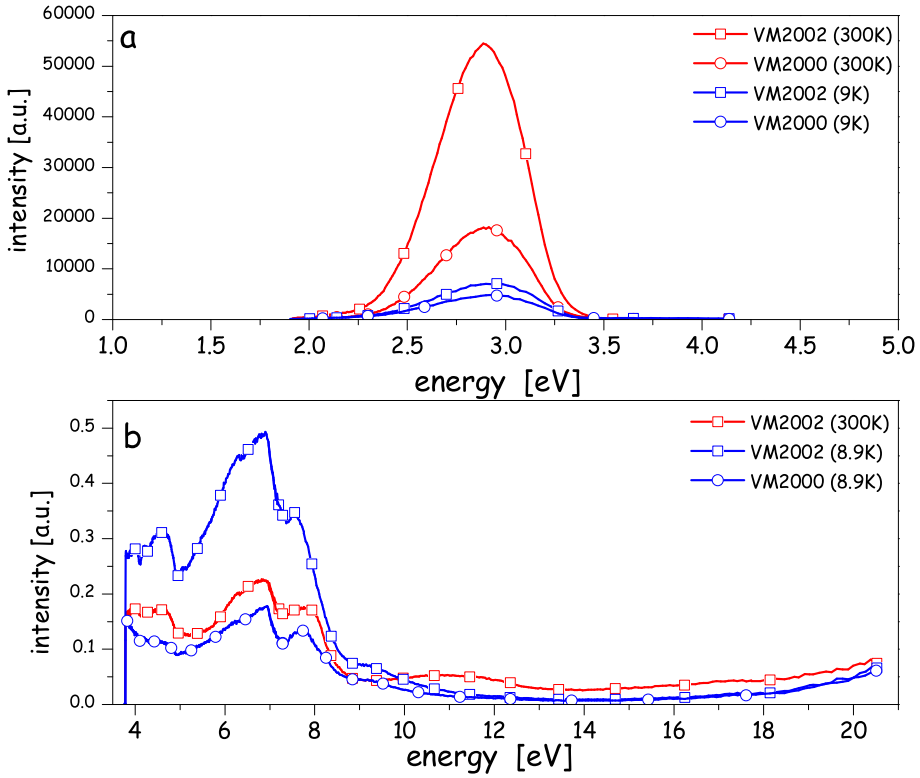

Figure 5.37: Excitation (b) and emission spectra (a) of VM2000 and VM2002 foils measured under VUV excitation. For the emission spectra the excitation was fixed at 40 nm (30 eV). For the excitation spectra the emission was fixed at 420 nm (2.95 eV). Different colors correspond to different temperatures while different symbols are used for the sample identification.

with scintillating and non-scintillating reflectors. Figure 5.39 shows results of two subsequent runs in the Gran Sasso setup. In run 27 a silver foil was used while the scintillating foil was applied in run 28. As the energy of the recoiling daughter nuclei from the alpha decays is typically around 100 keV, such events should appear mainly in this region of the phonon channel. The α emitters may have been implanted by preceding α decays and the recoil nuclei may loose part of their energy before they reach the $CaWO_4$ crystal. Therefore, the energy region where such α-induced background accumulates can be significantly widened to lower energies. As can be clearly seen in figure 5.39, the number of the events with a low intensity of light (or no light) in the critical region, is significantly reduced. The remaining events are most probably due to the presence of other non-scintillating material still present inside the module. This includes clamps

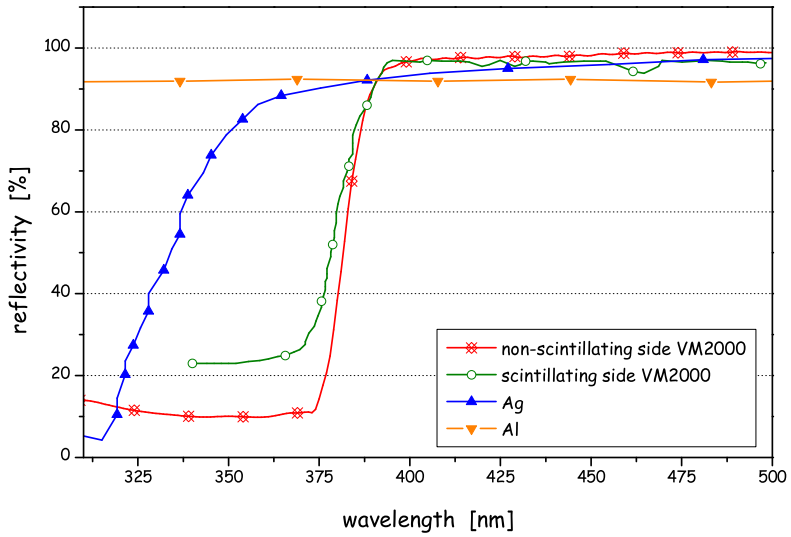

Figure 5.38: Measured reflectivity of a VM2000 multi-layer foil. Reflectivity of Al and Ag foils are given for reference.

that are used to fix the detector and teflon rings which are used to clamp the foil to the frame of the module. Scintillating paint to be used to cover these parts is in the testing phase.

Thermometer

On each $CaWO_4$ crystal a tungsten superconducting phase transition thermometer (SPT) has to be deposited. Here, the effects of the deposition on the scintillation properties as well as the influence of the size of the SPT on the scintillation light yield and the light collection will be discussed.
In the process of deposition of the SPT, the crystal is heated up to $\approx 450°$ C and kept in vacuum at this temperature over 24 h. A decrease of 20-40% in light yield was measured after the deposition process. In figure 5.40 this effect on the ^{60}Co spectrum measured in one of the crystals is illustrated. Additionally, the final roughening procedure was applied and the effect on the pulse height is presented. The corresponding values for the ^{137}Cs gamma line are presented in the table 5.2. One possible explanation for the loss of pulse height and resolution could be the formation of a "dead" layer (either a layer with a reduced scintillation yield or an absorbing layer) at the crystal surface. The comparison of the

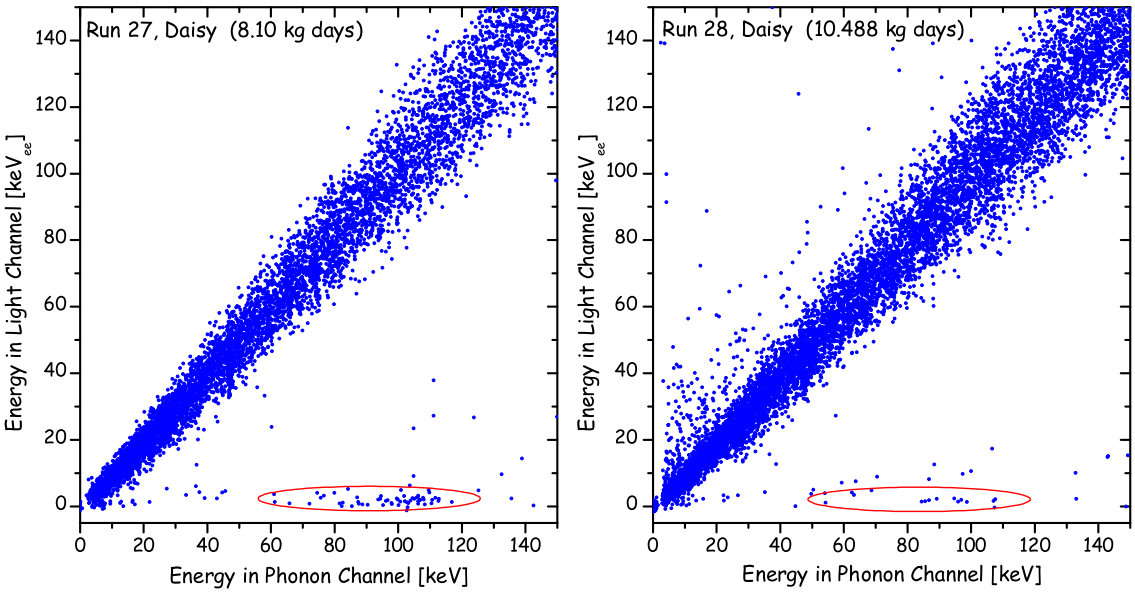

Figure 5.39: Correlation of energy measurements in the phonon and light detectors for two different choices of light reflectors. In Run 27 (left) a silver foil was used, in Run 28 (right) a scintillating foil of high reflectivity (VM2000).

Table 5.2: The effect of the SPT deposition on the pulse height and the resolution of ^{137}Cs line. Sample Julia was taken as an example but a similar effect was observed with all crystals. Additionally, the effect of roughening of the flat crystal surface opposite to the SPT side is also presented.

Status of the crystal	Normalized pulse height [%]	Resolution of ^{137}Cs line [%]
as delivered	100	12.5
after the first deposition	77.4	23.8
3 × cooled down and repolished	77.1	24.7
after the second deposition	56.1	29.3
one surface roughened	108.3	13.3

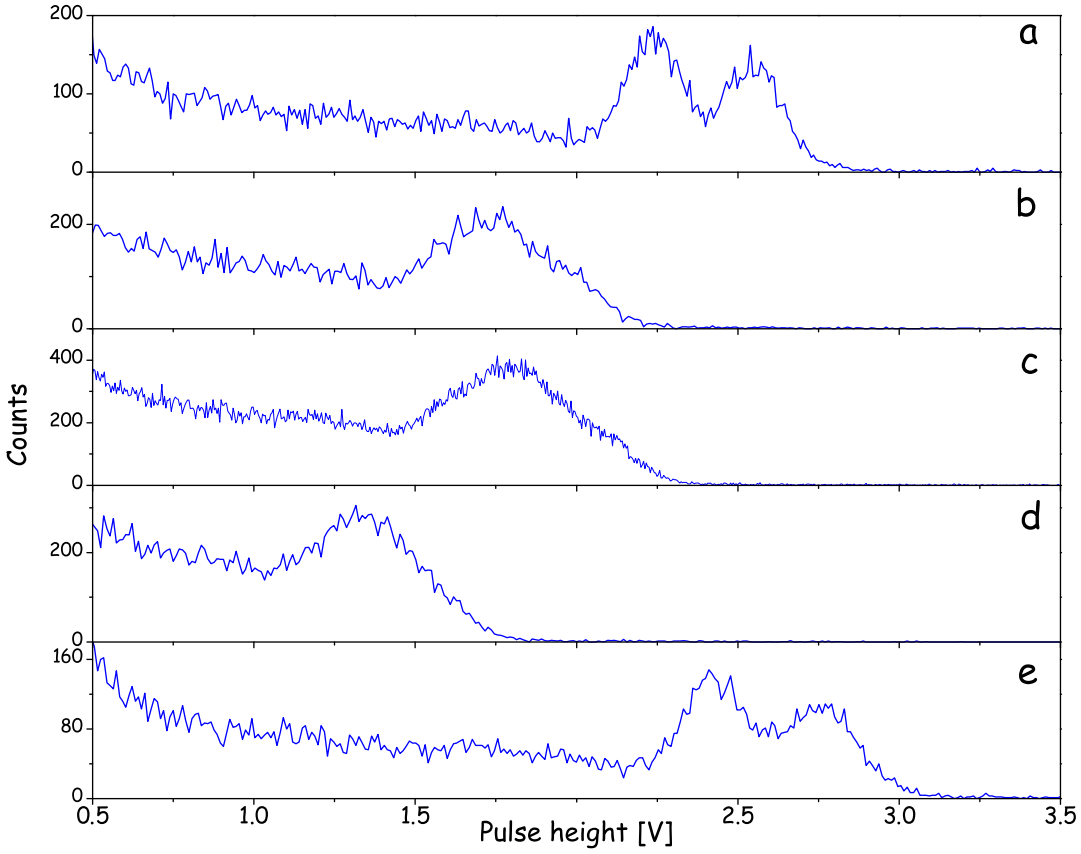

Figure 5.40: ^{60}Co spectra of crystal Julia (Russian) measured:
(a) as delivered
(b) after the first deposition of SPT
(c) after 3 additional cool downs and repolishing of the crystal
(d) after the second deposition of SPT
(e) after additional roughening of one crystal surface.

repeated measurement after one of the flat crystal surface was repolished[10] (Fig. 5.40 c) showed that this does not have a significant effect and therefore can not be an explanation for the observed degradation of the scintillation yield. Yet, the increase of the light collection due to the roughening of the crystal surface can compensate degraded light yield.
As explained in the section 2.7.2, an additional buffer layer of SiO_2 has to be

[10] a layer of $\simeq 0.5$ mm thickness is removed in the polishing process of the side opposite of the thermometer side.

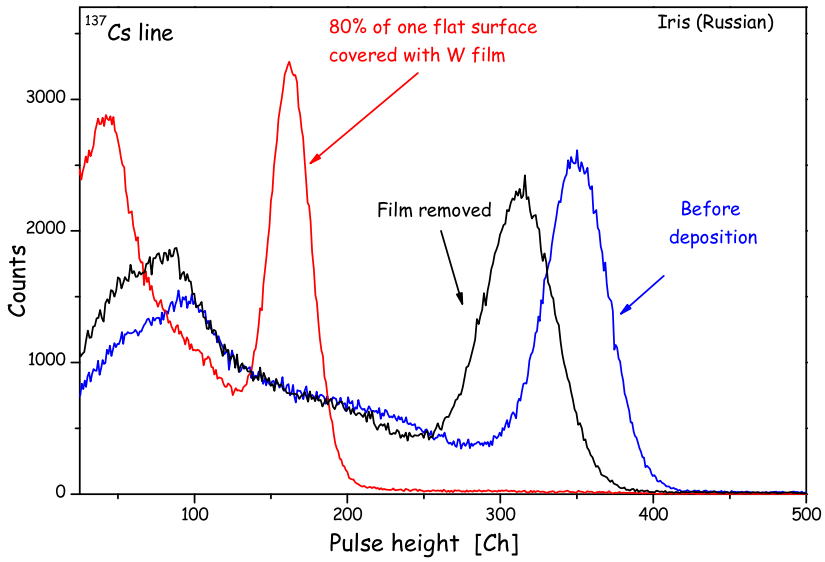

Figure 5.41: Reduction of detected light due to the absorption of the W-SPT. The deposited film was covering ≃80% of the flat crystal face. Light was detected with a PM tube on the opposite side of the crystal.

deposited at the crystal surface in order to prevent the diffusion between the tungsten film and the crystal. Because of its pronounced yellowish color this layer can absorb emitted light and therefore effectively reduce the amount of detected light. In order to address this issue several depositions with different thermometer sizes were made. As the deposition process is affecting the light yield of crystals, a comparison was made by measuring the crystal light yield after the deposition and additionally after the thermometer was removed (crystal face with thermometer was repolished). Figure 5.41 shows the effect of the absorption of a big ($\varnothing = 35\,\mathrm{mm}$) tungsten film on the pulse height of the ^{137}Cs gamma line. The reduction of ≃50% was measured when ≃80% of the flat surface was covered with the film. A thermometer size of $8\times6\,\mathrm{mm}^2$ leads to ≃8% reduction of the pulse height. As this is a typical thermometer size, a reduction of the detected light observed after the deposition process can be only partially explained with an absorption in the film itself.
Possible explanations could be found in the increased number of the oxygen vacancies or a formation of color centers. The deposition of the SPT in vacuum may reverse the effect of the annealing in oxygen atmosphere and lead to the decreased light yield. After deposition annealing can not be applied as the film quality would then be degraded.

5.3 Quenching factor measurements

Since the scintillation light output of $CaWO_4$ which is used as absorber in the CRESST Phase II cryodetector is different for nuclear and electron recoils, one can discriminate gamma and beta background events from nuclear recoil scattering events (see section 2.7.1, Fig. 2.10). The later can result from scattering of neutrons mainly on oxygen, the lightest nucleus of $CaWO_4$, or from WIMPs scattering mainly on tungsten, the heaviest of the crystal nucleus. To possibly discriminate WIMP events from neutron background it is very important to determine the quenching factors of different nuclei in the $CaWO_4$ crystal. The novel technique described in section 4.4 was developed and applied.
In this section the results of these measurements are presented. First a method for the selection of the ions by time-of-flight measurements for different elements are introduced. The description of the data analysis is then given. Finally, the quenching factor results at room temperature obtained using this ion beam technique are presented followed by a brief discussion of the first low temperature measurements as well as of some future plans.

5.3.1 MCP measurements

The time-of-flight mass spectrometer (TOF-MS) used for the quenching factor measurements is described in section 4.4. For the selection of the desired ions the additional deflection plates (shown in figure 4.4) were used as a mass filter. The Micro Channel Plate (MCP), placed at the middle of the flight path of the TOF tube was used to determine the time constants for the ion deflector. Figure 5.42 illustrates the applied selection method using the example of a CuBe target. The two naturally occurring isotopes of copper (^{63}Cu and ^{65}Cu) can be seen nicely separated.
In Appendix C the deflector time parameters determined for a list of used ions are given. The choice was made such that a broad mass range of elements (H, Be, O, Si, Ca, Cu, Y, Ag, Sm, W, Au) covers the ions of $CaWO_4$.
In order to reduce the background contribution due to the dark counts of the photomultiplier (PM) tube by choice of a counting time window (see Fig. 4.7) the time-of-flight for each selected element was measured. It is essential to precisely know the arrival time of the ions for the proper selection of the counting (time) window. The dependence of the time-of-flight, measured with the MCP, on $\sqrt{A}$ (where A is a mass number) for the selected elements is given in figure 5.43 and shows the expected linear relation (Eq. 4.2).

5.3.2 Room temperature measurements

For measurements at room temperature the crystal equipped with a light reflector and a PM tube (see figure 4.6) was mounted at the outlet of the mass

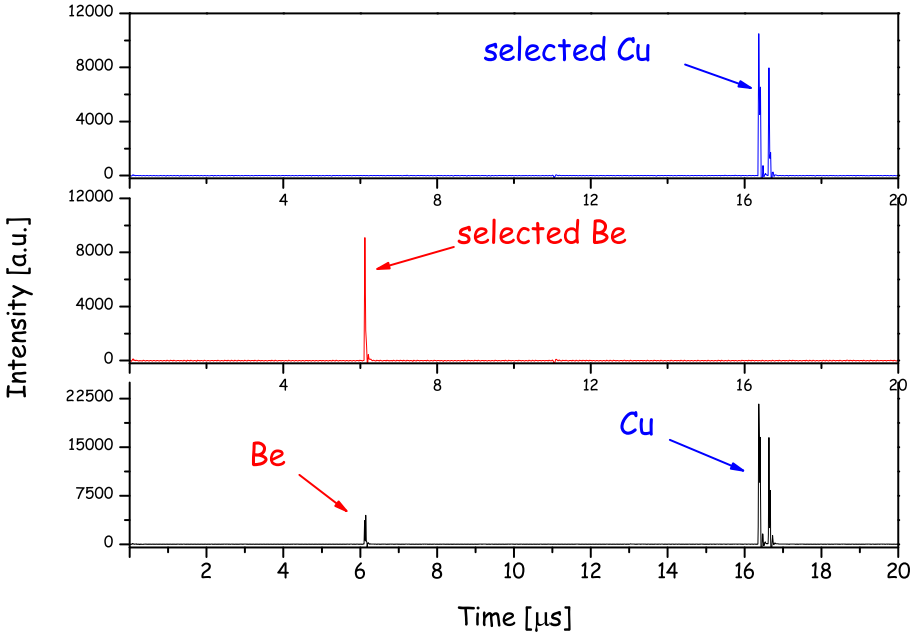

Figure 5.42: Application of deflection plates for the selection of desired ions. Bottom: MCP TOF spectrum of a CuBe target without deflection. Applying the proper selection parameters (Appendix C) only ions of beryllium (middle) or copper (top) are reaching the detector (and also the PM setup at the end of the TOF path).

spectrometer. The length of the counting (time) window was kept the same (30, 40, 50 μs) for all measured elements. For each laser shot the total number of registered photoelectrons as well as their individual arrival times were recorded to the disk. The former was used to determine the light yield, while the time information served to reconstruct light curves of the scintillator response (see section 4.4.4). Figure 5.44 shows light curves of $CaWO_4$ obtained with beryllium and copper ions. As the data acquisition is triggered by the laser shot the time-of-flight (TOF) information can be also derivated from the light curves. Having the detector placed at the outlet of the mass spectrometer the measured TOF is twice as high as the one of the MCP measurement (Fig. 5.43). Figure 5.45 shows the dependence of the time-of-flight, measured with the $CaWO_4$ crystal, on $\sqrt{A}$ for the selected elements.
Measured light curves were fitted in order to determine decay time of $CaWO_4$ measured this way. In figure 5.46 fits of the light curve using both single and

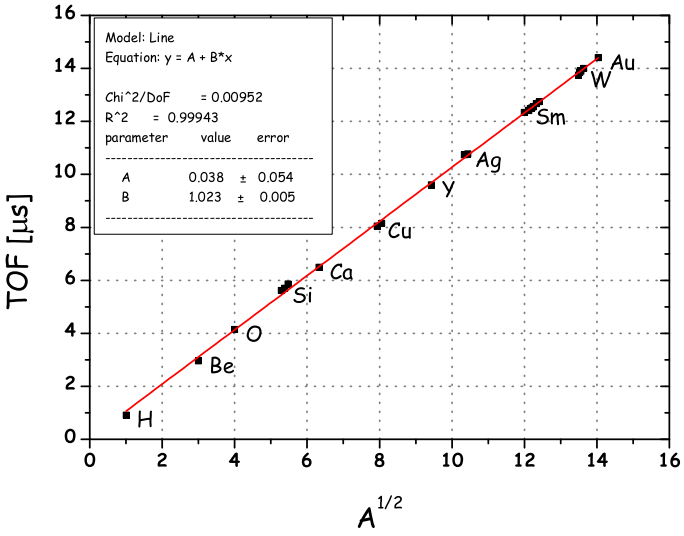

Figure 5.43: Dependence of time-of-flight on $\sqrt{A}$ (where A is a mass number) measured with a MCP placed at half the distance to the PM tube. The solid line represents a linear fit to the measurements with parameters as given in the box.

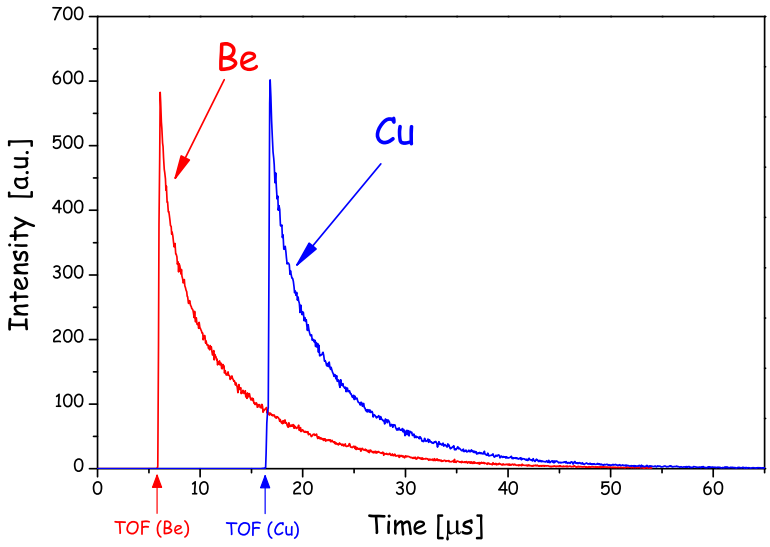

Figure 5.44: Light curves for beryllium and copper.

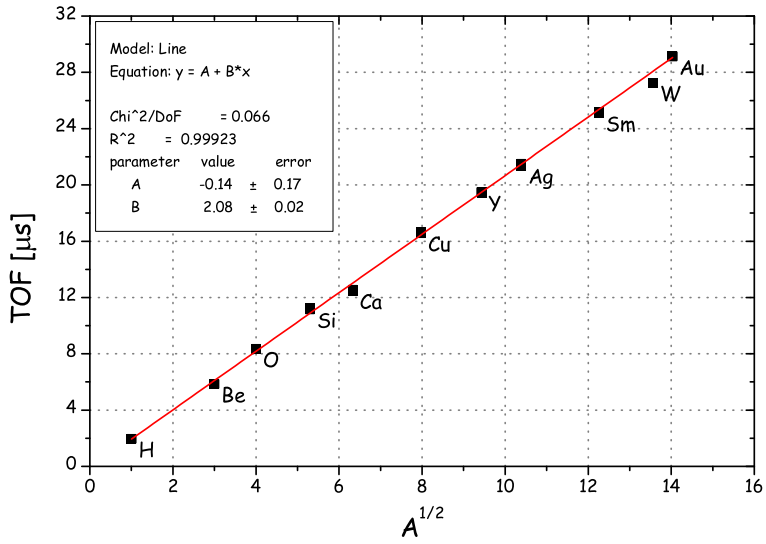

Figure 5.45: Dependence of time-of-flight on $\sqrt{A}$ measured with a $CaWO_4$ crystal in the PM setup placed at the outlet of the mass spectrometer. The solid line represents a linear fit to the measurements with parameters as given in the box.

bi-exponential decays are given. The better agrement of the bi-exponential decay function with the measured data indicates the presence of two decay constants in $CaWO_4$ at 300 K. The faster decay time is 1.08 μs while the longer one 7.96 μs. For $CaWO_4$ biexponential decay curves are reported for low temperatures [Bla83]. For room temperature two decay times $\simeq 2\,\mu$s and $\simeq 9\,\mu$s have been recently reported [Zde04]. Previous values reported are 5 μs measured under particle excitation [Bea62] and 9.2 μs measured under optical excitation [Koe93]. The sharp rise time ($< 50\,ns$) indicates the absence of electrical fields due to charge up of the crystal itself during the measurement. Additionally, the comparison of several subsequently measured light curves confirmed the absence of an additional field that could be produced by a charge up of the crystal itself or the teflon holder used as reflector and collimator. Such a field would lead to a reduced energy of the ions and therefore change their time of flight. This in turn would broaden the rise of the scintillation light curve or shift the offset position of the curve. Nothing of that type has been observed.

Reference measurement

The electron recoil reference measurement for the determination of the quenching factors was made with 5.9 keV X-rays from the ^{55}Fe decay. Figure 5.47 shows the spectra measured with two different $CaWO_4$ samples (Ch01 and Conrad) for

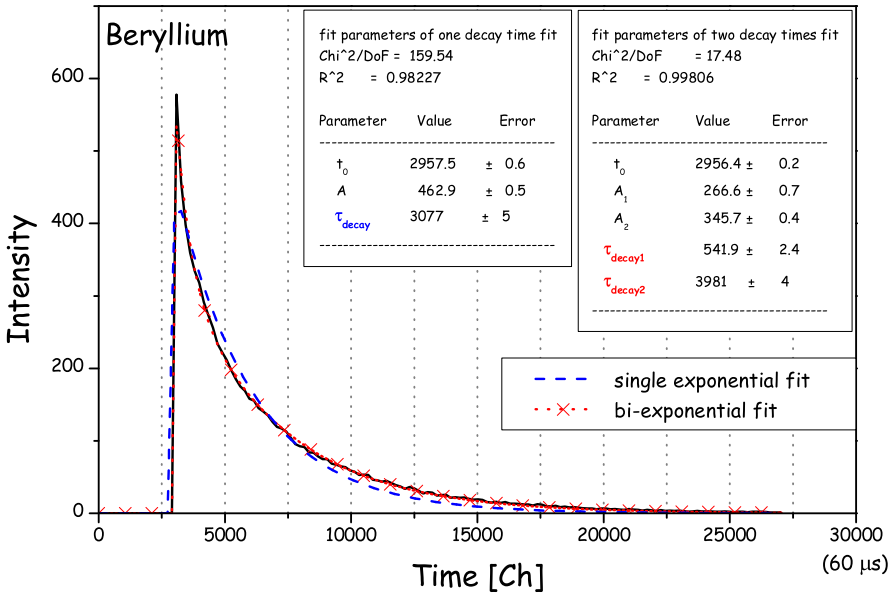

Figure 5.46: Determination of the decay constants of $CaWO_4$ at 300 K from the light curve of beryllium. Bi-exponential fit (dotted line) gives better agrement with measured data compared to the single exponential fit (dashed line) suggesting the existence of two distinguished decay constants. X-axis is given in channels having 1 Ch= 2 ns. Therefore, the fast decay time is 1.08 μs while the longer one is 7.96 μs.

a 30 μs photon counting window (see section 4.4.4). Ch01 has been measured with only one fixed time window (30 μs), while simultaneous measurements with three time windows (30, 40, 50 μs) were made with sample Conrad, in order to probe the dependence of the results on the length of the chosen time window. The spectra have been fitted using the fit procedure developed for ion spectra which will be discussed later.

Table 5.3: Fitted values of the numbers of photoelectrons for the ^{55}Fe peak for two different crystals (Ch01 and Conrad). For Conrad three different time windows have been analyzed. Only the statistical errors of the fits are quoted.

Time window	**Conrad**	**Ch01**
30 μs	23.67 ± 0.13 pe$^-$	15.28 ± 0.11 pe$^-$
40 μs	24.08 ± 0.13 pe$^-$	
50 μs	24.22 ± 0.14 pe$^-$	

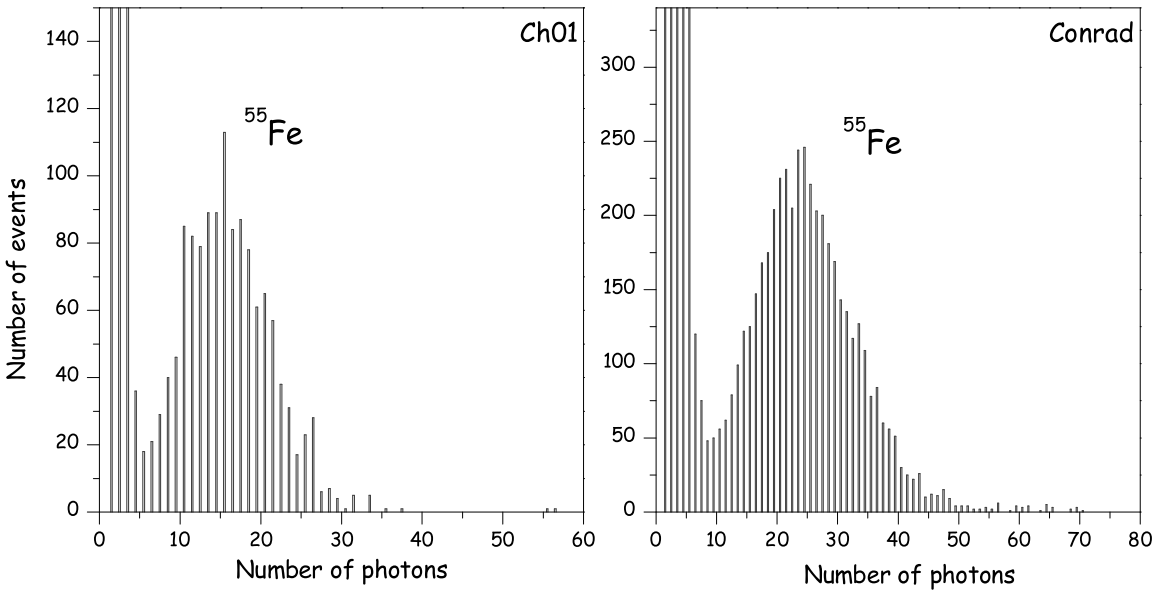

Figure 5.47: ^{55}Fe photon multiplicity spectra recorded with two different crystals for a time window of 30 μs. Corresponding fitted Poissonian mean values are 15.28±0.11 pe$^-$ for the Ch01 sample (left) and 23.67±0.13 pe$^-$ for the Conrad sample (right).

Spectra measured with various elements

A pulsed UV laser was used for desorption and ionization of the atoms which are then accelerated within the ion source and focused at the entrance of the TOF part of the mass spectrometer (Fig. 4.4). The laser power and the ion beam optics were adjusted such that the probability of multiple ion events (more than one ion impinging on the crystal surface per laser shot) was reduced as much as possible. The result is illustrated in figure 5.48. Laser power and focus were tuned that on average only each 15th laser shot gave an ion signal (figure 5.48 top).

Data analysis

For each laser shot a certain number of photons is detected. The main contribution to the recorded spectra comes from laser shots not producing ion signals which measure the dark counts of the photomultiplier. The number of dark counts obeys a Poisson distribution with a small mean value. The number of the

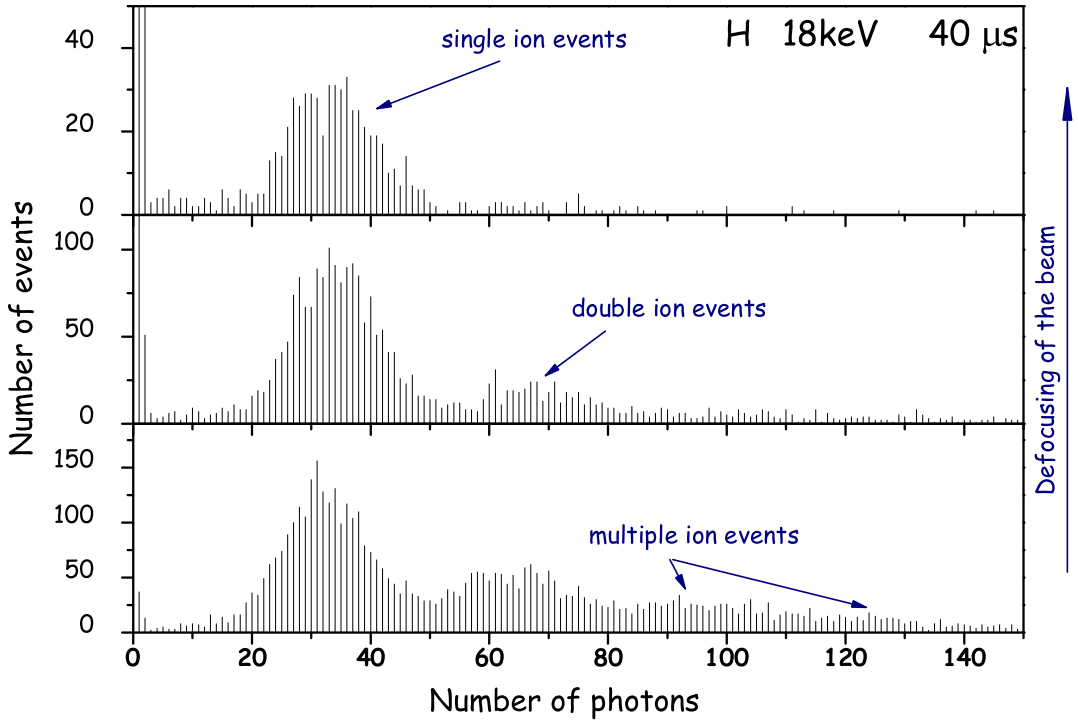

Figure 5.48: Illustration of the effect of the beam defocusing on the shape of photon multiplicity spectra measured for hydrogen of 18 keV. The total number of laser shots for the highest focusing is ≈ 8500 (bottom) while for the other two spectra this number is doubled. Defocusing leads to the reduced probability of multiple ion events but significantly prolongs the measurement time.

photons produced by single ion events [11] gives a spectrum with a Poisson distribution with a higher mean value. Due to a non-zero probability for multiple ion events Poissonians will appear with a mean value equal to a multiple of the mean of the first one. In the counting procedure the origin of the registered photons cannot be identified. Therefore, the background had to be accounted for in the fit function.
For simplicity first only none (background) and one ion (signal) arriving per laser shot will be considered. In this case the probability to have k registered photons, $P_t(k)$, is given by

$$P_t(k) \;=\; P_{ion}(0) \,\cdot\, P(k,\overline{B}) \;+\; P_{ion}(1) \sum_{l=0}^{k} P(l,\overline{B})\, P_S(k-l,\overline{n} \,\cdot\, 1)\,, \qquad (5.3)$$

[11] Due to the reduced laser power and applied beam defocusing only single and a double ion events are occurring.

where $P_{ion}(i)$ is the probability for i ions arriving per laser shot, $P(k, \overline{B})$ is the probability of observing k background counts from a Poissonian distribution with a mean $\overline{B}$ and $P_S(m, \overline{n})$ is the probability that m signal counts are observed when $\overline{n}$ is the average number of observed photons for single ion events. The term describing the ion signal sums the probabilities of all possible contributions of background and signal counts. When up to N ions arrive per laser shot equation 5.3 generalizes to

$$P_t(k) \;=\; P_{ion}(0) \;\cdot\; P(k, \overline{B}) \;+\; \sum_{i=1}^{N} P_{ion}(i) \sum_{l=0}^{k} P(l, \overline{B})\, P_S(k-l, \overline{n} \;\cdot\; i)\,. \qquad (5.4)$$

Here, $P_{ion}(i)$, $\overline{n}$ and $\overline{B}$ are the fit parameters. The background is described by a Poissonian with a scale factor $P_{ion}(0)$ which can be fitted. The mean value $\overline{B}$ of the background Poissonian is fixed using a separate background measurement for each time window. The signal can be fitted with a selectable number of multiple ion events to be taken into a consideration. The scale factor $P_{ion}(i)$ for each of the signal Poissonians i.e. the probability that a number i of ions arrives per laser shot and the average number $\overline{n}$ of detected photoelectrons per ion are free fit parameters. In figure 5.49 different fits to the multiplicity spectra measured for H and W ions are shown. The dashed lines represent fitted spectra using the method described above.
As the peak positions of the single and double ion events of the hydrogen spectra are well separated from the background it was possible to check the validity of the background model used in the fit. Therefore, the three scale factors ($P_{ion}(0)$, $P_{ion}(1)$, $P_{ion}(2)$), $\overline{n}$ and $\overline{B}$ were left as free fit parameters. Within the statistical errors the values obtained for $\overline{B}$ are in agrement with those from the background measurements.
In the case of the hydrogen spectra there is a definite excess of measured events over the fitted line on the left hand side of the single ion peak [12]. Such a background could be either produced by a relatively small number of ions that reached the crystal surface with a reduced energy or by backscattered ions which deposit only part of their energy in the crystal. In order to address this question, the process of the ions impinging onto the crystal surface was simulated using the SRIM2003 simulation package (Stopping and Range of Ions in Matter version 2003)[SRI]. This package calculates the stopping power and the range of ions in matter using a full quantum mechanical treatment of ion-atom collisions. Details of the parameters used as well as tables containing the summarized results are given in the Appendix D. Here, only the effect of backscattered ions will be discussed.

[12] This effect was only observed in the case of the hydrogen spectra where the signal peak position is far from the background, whereas for the heavier ones the Poissonians overlap such that the effect can not be noticed.

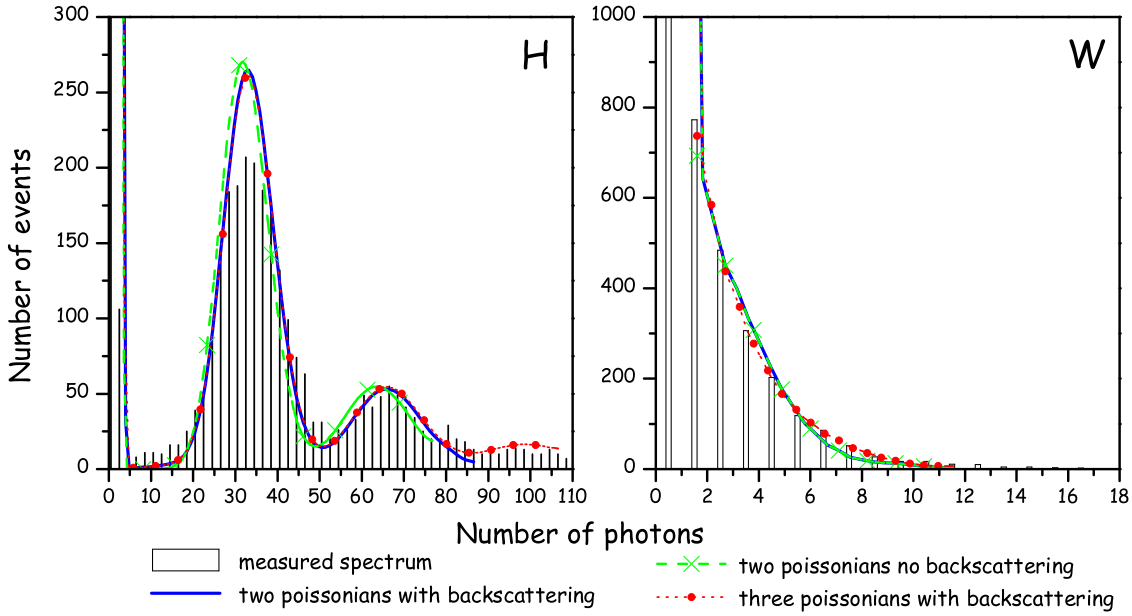

Figure 5.49: Comparison of different fits to photon multiplicity spectra. Two examples are shown: hydrogen, 18 keV (left) and tungsten, 18 keV (right). The histograms represent the measured data. The solid lines are likelihood fits including single and double ion events and backscattering of the ions. The dashed lines are fits without the backscattering effect while the dotted lines show the fits which include triple ion events and backscattering of the ions. The fit parameters are given in the table 5.4.

Figure 5.50 shows the simulated spectra of the energy deposition in the target ($CaWO_4$) crystal from the backscattered ions for several projectiles. The total number of simulated ions is the same for all elements (10000 ions) and the numbers of backscattered ones are indicated on the figure. The energy spectra as well as the probabilities for the backscattering obtained from the simulation were implemented in the fit using the following procedure. An energy deposition with a energy lower than the nominal one will result in the production of a reduced number of photons obeying Poisson statistics within each energy bin. In order to consider energy losses due to the backscattering, the following fit function was used

$$P_t(k) = P_{ion}(0)P(k,\overline{B}) + \sum_{i=1}^{N} P_{ion}(i) \sum_{l=0}^{k} P(l,\overline{B}) \int_0^{E_{ion}} P_S(k-l, \overline{n}\, i \frac{E_d}{E_{ion}}) P_{BS}(E_d) dE \,, \tag{5.5}$$

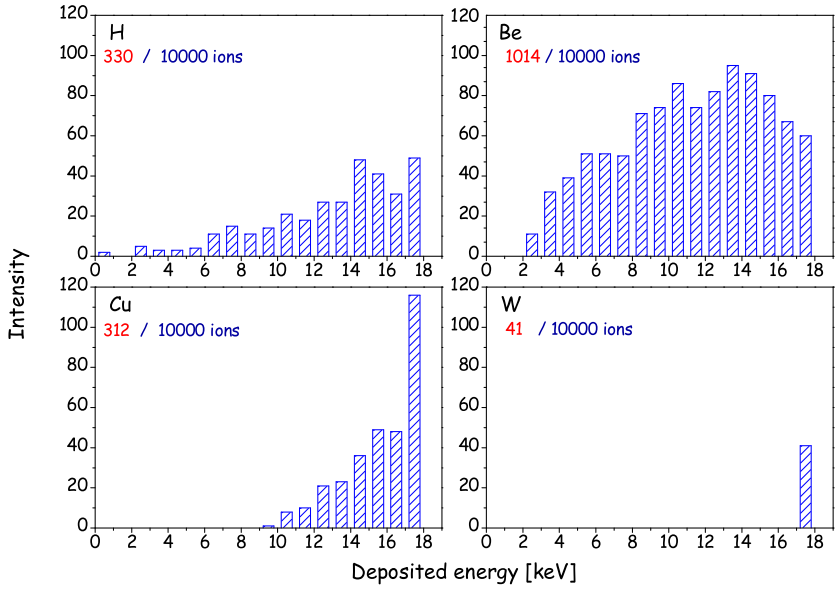

Figure 5.50: Reduced energy deposition due to backscattered ions. A SRIM2003 simulation was used and a total of 10000 ions have been simulated in each case. For each element the number of ion hits with a reduced energy deposition due to backscattering is indicated in the upper left corners of the graphs.

where $P_{BS}(E_d)$ is the probability density that due to the backscattering losses the energy E_d is deposited instead of the full energy of the ion E_{ion} ($P_{BS}(E_d)$ has been calculated with SRIM2003).
Fits containing the effect of backscattering are shown in figure 5.49. Adding the backscattering effect gave a slightly better agreement with the measured data in the case of the lighter elements. No change was observed for the heavier ones where the backscattering effect is only in the permil range. Therefore, the backscattering of the ions can be only a partial explanation for the observed shape of the hydrogen spectrum.
For the extremely light ions like hydrogen another possibility for energy losses is conceivable. Protons that are flying close to the collimator inner surface could be scattered with a shallow angle and therefore reach the crystal surface with a reduced energy. In order to address this issue, a test measurement was performed where a thin tape was glued on top of the existing ion collimator hole ($\varnothing = 1\,\mathrm{mm}$). A hole with a diameter of 0.7 mm was made in the center to prevent the ions from hitting the surface of the long collimator hole. This way, the number of the events that can scatter off the teflon surface should be considerably reduced. The resulting spectra showed a lower relative intensity of the excess events. But,

most probably due to a non perfect alignment of the used collimator, the effect was still partially observed. This indicates that the nature of the small excess background in the region below the single ion peak can be at least partially explained but further investigation is needed. Nevertheless, these excess events are only a very small fraction of the total counts and have a negligible influence on the fitted peak positions.

Table 5.4: Fitted values of the mean number of photoelectrons observed for single ion hits $\overline{n}$ of signal Poissonians using different fitting procedures shown in figure 5.49.

Fit description	**Hydrogen**	**Tungsten**
Double ion events and backscattering effect	32.96 ± 0.10	1.72 ± 0.05
Double ion events and no backscattering effect	31.75 ± 0.10	1.72 ± 0.10
Triple ion events and backscattering effect	32.99 ± 0.07	1.63 ± 0.10

A comparison of the results obtained for H and W from the fits is given in table 5.4. The effect of backscattering is noticeable only for the lighter elements while the heavier ones are more sensitive to the number of Poisson distributions included into the fit due to the strong overlap of distributions. As previously discussed, using the defocusing of the beam the probability for multiple ion events is reduced as much as possible and therefore only single and double ion events had to be taken into account. This can be considered as a conservative approach since the introduction of the third Poissonian into a fit shifts the mean to smaller values. Cross checking was made on several examples where the same spectra have been fitted in addition with a triple ion event peak and all fitted values were within the statistical error of the fits. The backscattering effect was included in the final fitting procedure as it gave a slightly better agreement in the case of lighter elements.
The ratio of the normalized (to 1 keV) number of registered photons from the ion spectra and the reference measurement[13] will give the quenching factor for that specific element:

$$QF(ion) = \frac{pe^-(^{55}Fe)}{pe^-(ion)} \cdot \frac{18\,keV}{5.899\,keV}\,. \tag{5.6}$$

[13]Only K_α X-rays (5.899 keV) were taken into account.

Results

Figure 5.51 shows the resulting fitted spectra for oxygen, calcium and tungsten ions of 18 keV measured with the sample from crystal Conrad with a 30 μs time window.

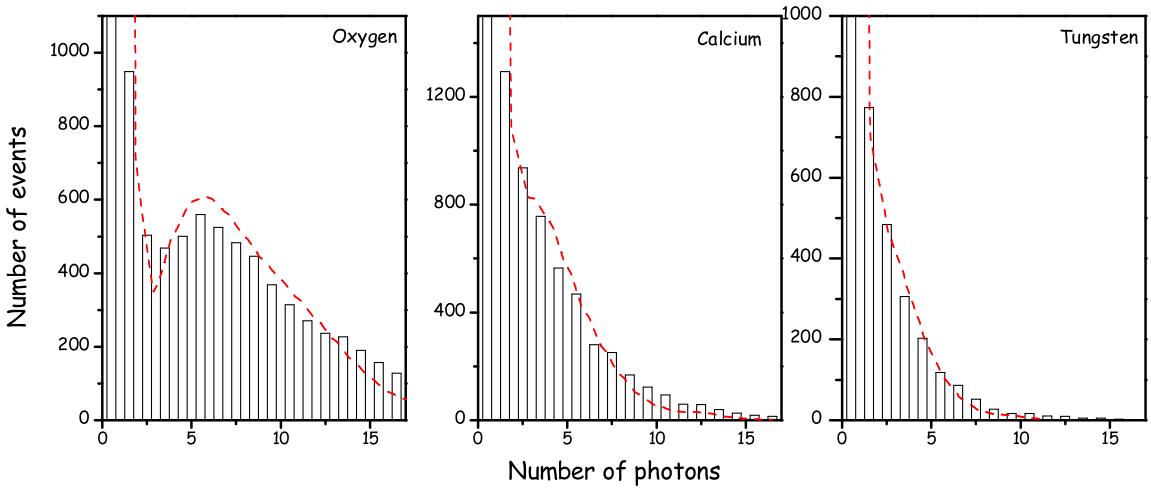

Figure 5.51: Fit of measured spectra for oxygen (left), calcium (middle) and tungsten (right) ions using the Conrad sample. Presented spectra are measured with a 30 μs time window. Corresponding fit values of the mean number of pe^- are **O**: $5.15 \pm 0.07\,\mathrm{pe}^-$, **Ca**: $2.70 \pm 0.06\,\mathrm{pe}^-$ and **W**: $1.72 \pm 0.05\,\mathrm{pe}^-$.

Mean values obtained from the fits to spectra of all elements, as well as numerical values calculated for the quenching factors are given in table 5.5. A graphical presentation of the dependence of the quenching factors on the ion mass, evaluated with different time windows, is given in figure 5.52. For the sample Conrad three time windows (30, 40, 50 μs) have been measured while only the 30 μs time window was selected in the measurements with sample Ch01. It should be noted that the measurements with sample Ch01 were done before the recording of the light curves was developed and the overall statistics is significantly lower compared to the measurements of the Conrad sample. In addition, within the 30 μs time window not all emitted light is collected (see figure 5.44) whereas practically no light is emitted more than 40 μs after the impact. This could be an

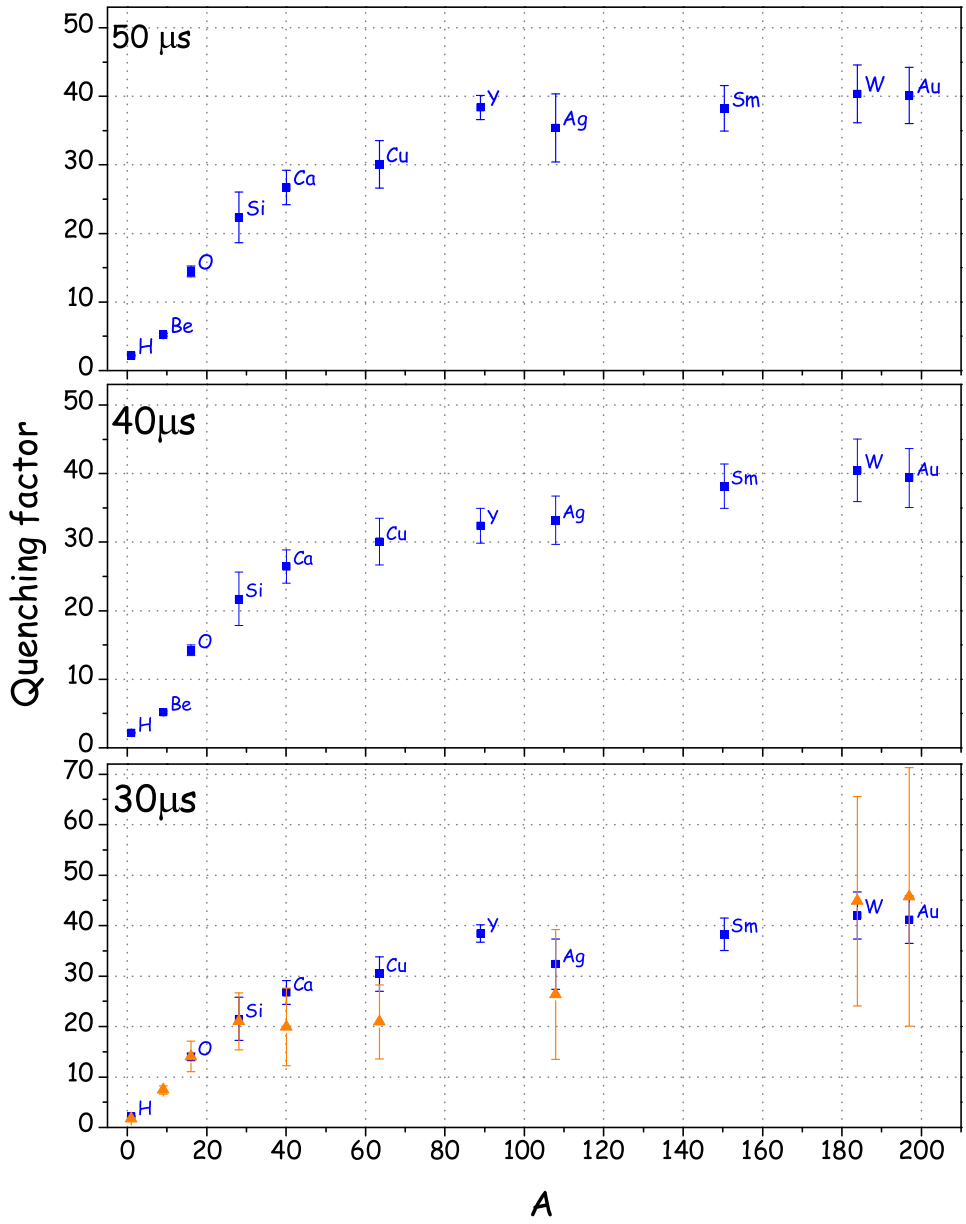

Figure 5.52: Dependence of the quenching factor on the mass of selected elements. Results from sample Conrad and Ch01 are shown as squares and triangles, respectively. Measurements using three different time windows are shown for comparison.

Table 5.5: Mean number of detected photoelectrons and quenching factor values (sample Conrad).

	Mean value [pe$^-$]			**Quenching factor**		
	30 μs	40 μs	50 μs	30 μs	40 μs	50 μs
H	32.95±0.10	33.77±0.10	33.78±0.10	2.19±0.06	2.18±0.06	2.19±0.06
Be		14.17±0.09	14.17±0.09		5.2±0.2	5.2±0.2
O	5.16±0.07	5.15±0.06	5.11±0.06	14.0±0.8	14.2±0.8	14.5±0.8
Si	3.36±0.20	3.38±0.18	3.31±0.16	21.5±4.3	21.7±3.9	22.4±3.7
Ca	2.70±0.06	2.78±0.07	2.77±0.07	26.8±2.3	26.4±2.4	26.7±2.5
Cu	2.38±0.07	2.44±0.08	2.46±0.08	30.4±3.4	30.1±3.4	30.1±3.5
Y	1.88±0.02	2.27±0.05	1.93±0.02	38.4±1.7	32.4±2.5	38.4±1.8
Ag	2.23±0.10	2.21±0.07	2.09±0.08	32.4±5.0	33.2±3.5	35.4±5.0
Sm	1.89±0.04	1.92±0.04	1.93±0.04	38.3±3.2	38.2±3.2	38.2±3.3
W	1.72±0.05	1.81±0.06	1.83±0.05	42.0±4.7	40.5±4.5	40.4±4.2
Au	1.75±0.06	1.87±0.06	1.84±0.05	41.2±4.7	39.3±4.3	40.1±4.1

explanation for slightly different values of mean values of pe^- measured in the 30 μs time window and 40 μs (see table 5.5). Yet, practically identical values are obtained in the 40 μs and 50 μs time window measurements.

The quenching factor for ^{206}Pb can be calculated using data from Run 27 of the CRESST experiment in Gran Sasso. In this run, a silver foil was used as a reflector. An external surface contamination of ^{210}Po was identified (see figure 5.5). This nuclide originates from radon, and is a common contaminant on or slightly below surfaces, where it can be implanted by alpha decays. It decays to ^{206}Pb and an α particle. Figure 5.53 shows a scatter plot of Run 27 where on the Y-axis the ratio of the energy of light and phonon detector is plotted as a function of the energy of the phonon channel. The dashed lines represent the acceptance band for neutrons taking a quenching value QF = 7.4 deduced from the proof-of-principle experiment (see fig. 2.10, Sec. 2.7.1) while the dotted lines correspond to the quenching factor of oxygen (14.2) from the mass spectrometer measurement. The events in question are seen as a well defined horizontal strip between 80 and 110 keV, clustered along and slightly below the lower dashed line. They occur when a ^{210}Po nucleus on the reflector foil surrounding the module decays into the α particle of 5.3 MeV and the ^{206}Pb nucleus with 104 keV. If the α moves away from the $CaWO_4$ detector and the ^{206}Pb goes into the detector, the result is a low energy, low light event. The energies of the events extend below the 100 keV of the ^{206}Pb nucleus since the ^{210}Po was implanted on the surface of the foil or somewhat below it by previous alpha decays, and the ^{206}Pb nucleus loses some energy on the way out. A similar process can take place

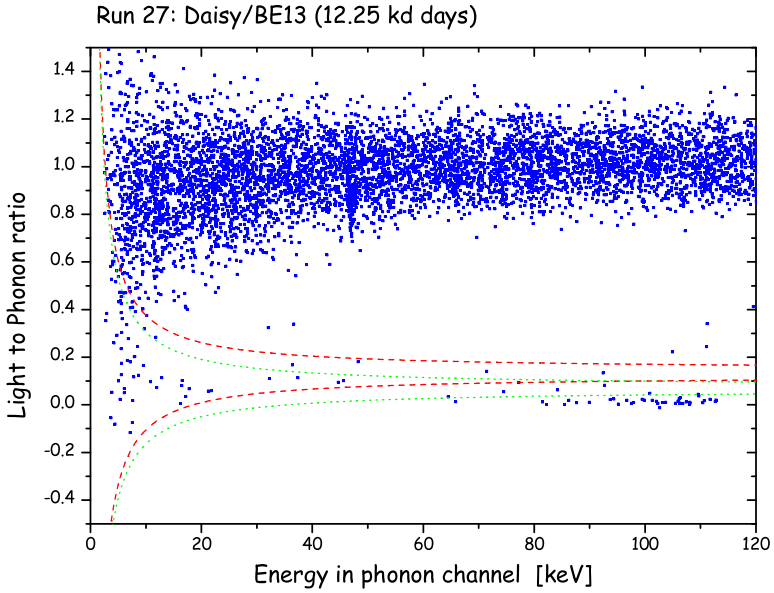

Figure 5.53: Distribution of light yield (ratio of energy in the light channel to energy in the phonon channel) as a function of the energy in the phonon channel (recoil energy) in Run 27. Below the upper and lower dashed (dotted) curves 90 % and 10 % of recoils with a quenching factor of 7.5 (14.2) are expected, respectively. The group of events below the lower dashed line, in the energy region around 100 keV corresponds to the recoils of ^{206}Pb (see text).

when the ^{210}Po is on or near the surface of the $CaWO_4$ crystal. In this case it is the alpha that loses some energy on the way out, leading to energies somewhat above 100 keV. With these events identified as ^{206}Pb, their light yield may be used to find the quenching factor for ^{206}Pb in the experiment. The horizontal character of the cluster indicates constancy of the quenching factor with energy. The group of events below the lower acceptance line for QF = 7.4 have the light yield distribution shown in figure 5.54. Fitting the peak with a Gaussian gives a mean light yield of 0.021±0.003. This translates into a quenching factor of 48.7 ± 7.1 for ^{206}Pb recoils which is also shown in figure 5.55.

A neutron scattering experiment for the measurement of quenching factors has been assembled at the Technische Universität München in Garching [Joc02]. Preliminary results measured for the oxygen and calcium recoils in $CaWO_4$ (O: 12.8 ± 0.5 and Ca: 15.9 ± 4.1 [Jag04b]) are for comparison also shown in figure 5.55. For the tungsten recoils it was only possible to determine a lower limit of $QF(W) > 33$ (at $2\,\sigma$ confidence level) [Jag04b].

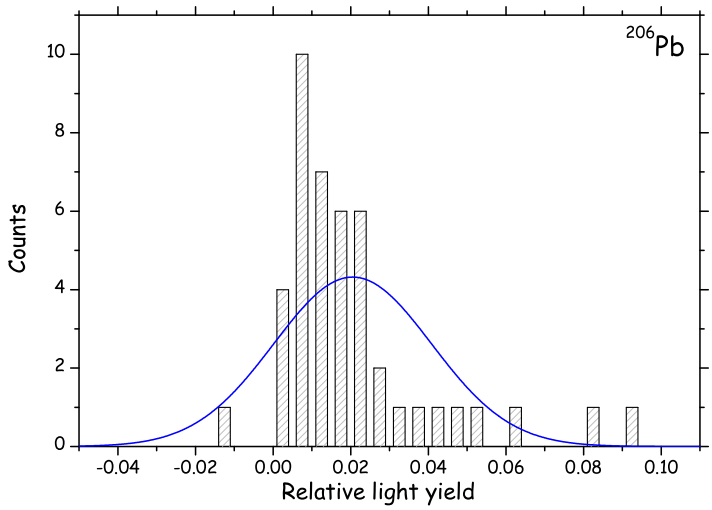

Figure 5.54: Light yield for ^{206}Pb recoils. A Gauss fit gives a mean light yield of 0.021±0.003 .

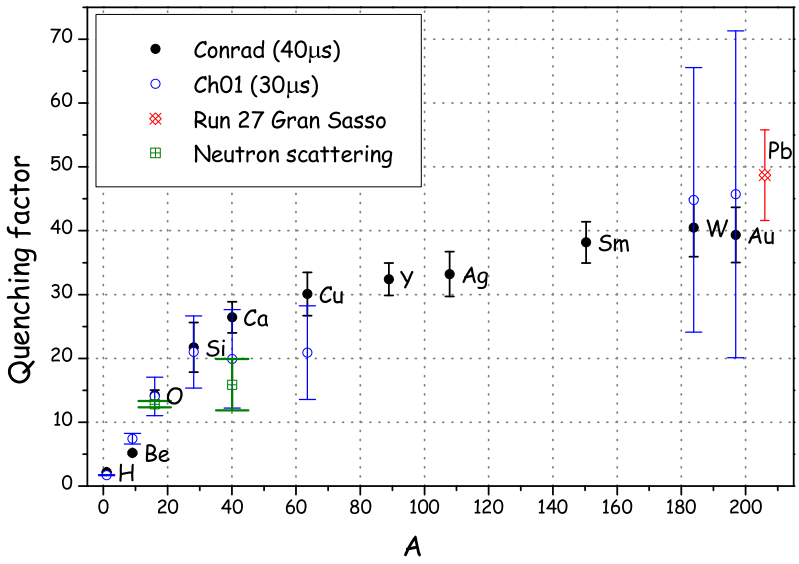

Figure 5.55: Summary of measurements of the quenching factors for $CaWO_4$ crystal. Discussion is given in the text.

The method developed in this work allowed the first measurement of the quenching factor for tungsten recoils in a $CaWO_4$ crystal. The result is

$$QF(W) \;=\; 40.5 \;\pm\; 4.5\,. \tag{5.7}$$

5.3.3 Low temperature measurements

In order to further investigate quenching factors at low temperatures, a setup described in section 4.4, Fig. 4.8 was assembled. The increased number of dark counts due to the exchange of the detector (an APD at 77 K was used instead of the PMT) was partially compensated by a pulse shape discrimination. The data acquisition was modified such that the record containing a pulse recognized as a dark count was discarded (for details see section 4.4). The main disadvantage of this method is a significant prolongation of the measurement time. In addition, the decay time of the scintillation process in $CaWO_4$ increases with decreasing temperature (see for example [Bea62] [Bla83]). Figure 5.56 shows the light curve of $CaWO_4$ measured at 6 K. The dashed line is a fit with each two

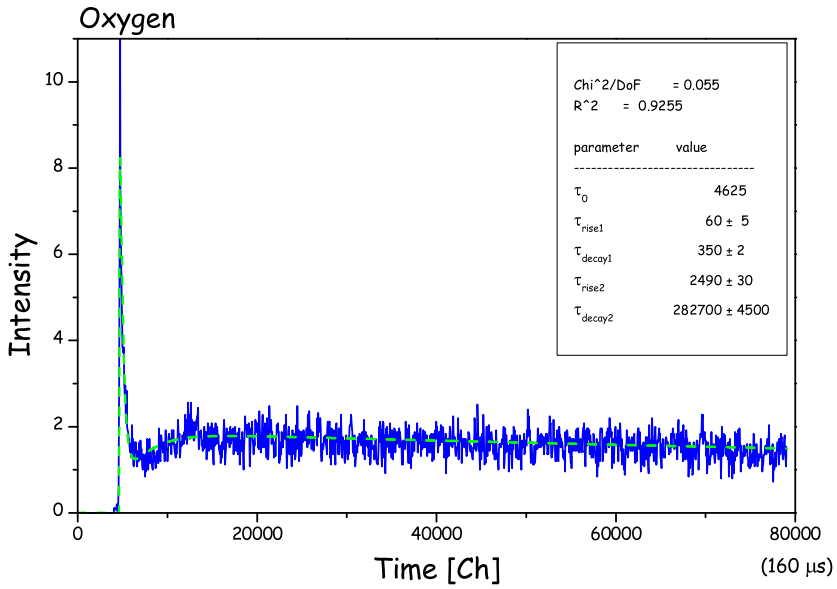

Figure 5.56: Light curve of a $CaWO_4$ crystal produced under excitation with oxygen ions at 6 K. The X-axis is given in channels (2 ns / Ch). The light curve was fitted with two exponential components with separate rise and decay times. The fast decay time is about 700 ns while the longer one is about 560 μs. The emission of the fast component starts practically instantaneous while the component with the long decay time also has a slow rise ($\tau_{rise} = 4.9\ \mu s$).

exponential rise and decay times (see equation 3.19). The fast decay is about 700 ns while the value for the slow decay time is about 560 μs. The rise time of the slow component is about 4.9 μs. The uncertainties are relatively big due to the short measurement time window (150 μs). Blasse reports two components in the scintillation response of $CaWO_4$ at 6 K of decay times of a few μs for the fast component and $\approx 350\,\mu$s for the slow component [Bla83]. In order to collect all the emitted light, the time window has to be significantly enlarged compared to the room temperature measurements.
Figure 5.57 depicts a set of photon multiplicity spectra measured with oxygen ions at 6 K. The photoelectrons were counted on-line for different time windows (indicated along the left side of the graph). As a consequence of the increased number of discarded shots, due to the presence of dark counts, the overall statistics is dramatically decreased for the large time windows as illustrated on figure 5.57. An additional problem arises for the reference measurement. Data acquisition with a triggering on the signal from the detector can not be used due to the high number of dark counts. Different other methods have been tested but non of them gave convincing results. Therefore, substantial improvements of the existing setup are necessary for the low temperature measurements of quenching factors.
Improvements may be achieved with an active biasing scheme to quench the avalanche of the APD . The passive mode applied in the existing setup limits the current that can flow through the diode to a value small enough to ensure the avalanche to be quenched, the active mode reduces the reverse voltage across the diode to be significantly below break-down for a certain time after each pulse. Passive quenching suffers from a rather slow time response, since the resistors required to stop the avalanche are quite large resulting in large RC time constants. Active quenching requires special fast electronics and FETs capable to switch the required voltage (several 10 V) within a few ns. Therefore, active quenched APDs should have an overall performance quite comparable to standard photon counting PMTs, as long as a fast quenching can be achieved.
Another possibility would be to use a Hybrid Detector, combining features of APD's and PMT's. Using a semi-transparent photocathode, the Hybrid Detector at first strongly accelerates the free electron released from the photocathode by a photon. This electron, in a second stage, bombards an APD structure which acts as secondary electron amplifier. Since the APD can not be operated in Geiger mode due to the large diode area required (typically several square mm), the overall amplification is typically 10^4 or less (for 8 to 10 kV acceleration voltage). Yet, when cooled, it can still be used for single photon detection. Advantages of this device would be shorter pulse rise time and shorter pulse duration. The main disadvantage of the detector is its lower quantum efficiency compared to an ADP which, however, should still be as good as that of a PMT at room temperature.

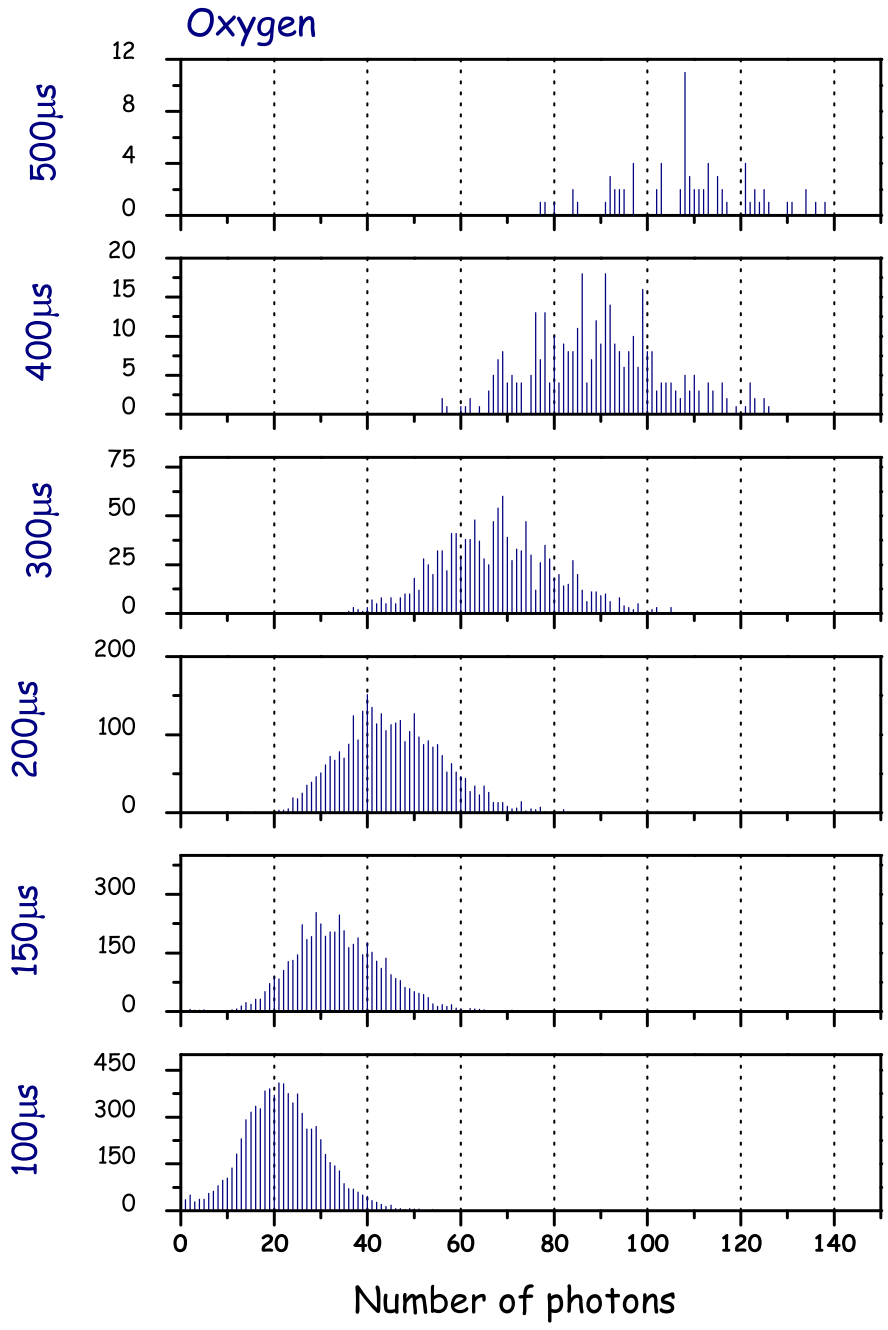

Figure 5.57: Spectra for 18 keV oxygen ions, measured at 6 K. Simultaneous counting was performed for several counting window lengths (time indicated at the left-hand side). Discussion is given in the text.

5.3.4 Summary

A new method has been developed for the measurement of quenching factors of light yields of ions interacting in scintillators. It uses a mass spectrometer to accelerate ions and measures in single photon counting mode the light which they produce when impinging onto a crystal.
As previously mentioned, a possible drawback of the new technique for the quenching factor measurement could be a surface dependence of the light yield of the probed scintillator. In the case of $CaWO_4$ crystals we could not observe any surface dependence. Strong arguments for this could be found in the comparison of the light yields of the ^{210}Po alpha decay identified in Run 27 (see figure 5.5). The ^{210}Po process provide an argument that the quenching factor is the same for surface events and interior events in the crystal. In Fig. 5.5 there are two nearby peaks for ^{210}Po decay, labelled "internal" and "external". "Internal" events are in the interior of the crystal and therefore show the full energy of the ^{210}Po decay. The somewhat lower energy of the "external" peak corresponds to surface events where the ^{206}Pb nucleus escapes and only the α remains in the crystal. The light yield is the same for both peaks, showing, at least for alpha particles, that the quenching factor is the same for interior and surface events. This supplements the argument in [Meu99] that the absence of any splitting of the electron-photon band, where one has electrons mostly near the surface and photons mostly in the interior, demonstrates that bulk and surface events have the same quenching factor.
The measured value for oxygen ions is in good agreement with the value obtained from a neutron scattering measurement at room temperature [Jag04a]. The quenching factor of tungsten recoil in $CaWO_4$ crystals was measured for the first time and an extremely high value of 40.5 ± 4.5 was obtained. Some discrepancies between the different measurement techniques for the quenching factor of calcium in $CaWO_4$ (see figure 5.55) indicates that further investigation is needed.
To investigate the origin of the behavior of the quenching factors the energy loss processes for ions impinging on the $CaWO_4$ crystal were calculated with the SRIM2003 simulation package. The results summarized in table D.1 clearly show that the quenching effect can not be explained only by the reduction of the energy losses for ionization of the material as this value saturates for ions heavier than copper whereas the quenching factor further increases. The only parameter that is further changing with ion mass is the range in the target material. This may indicate a saturation of the excited states of $CaWO_4$ along the path of the ion, especially for the extremely heavy ones.
The measured high quenching for tungsten nuclei gives further discrimination potential for the CRESST Dark Matter search. Figure 5.58 shows the low energy distribution in the Dark Matter run. The vertical axis represents the light yield expressed as the ratio (energy in the light channel / energy in the phonon

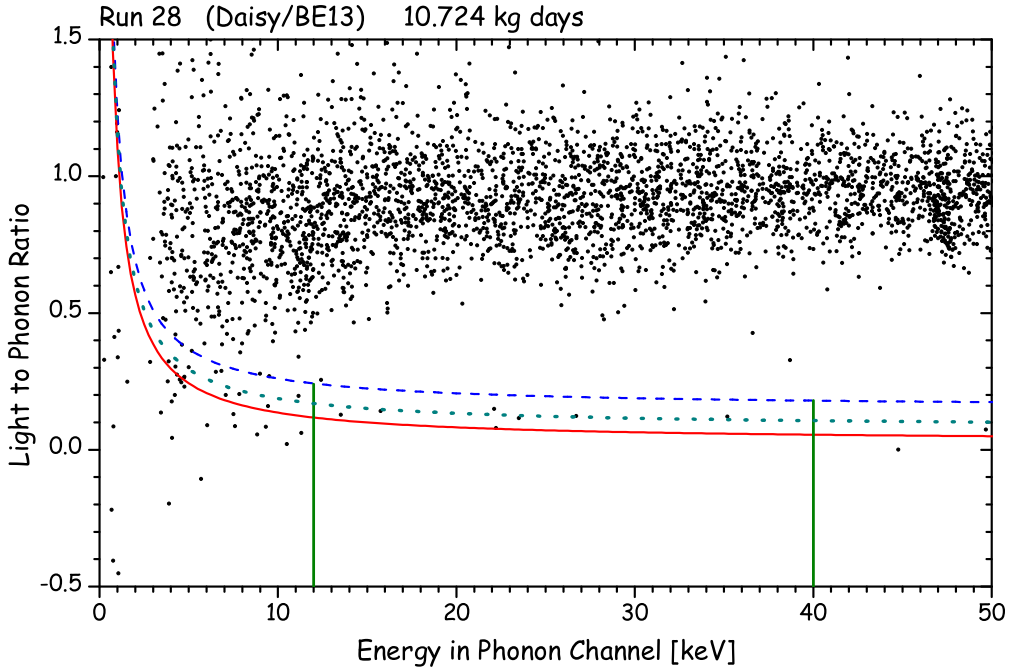

Figure 5.58: Low energy distribution of simultaneous phonon and light detection in the Dark Matter run. The vertical axis represents the light yield expressed as the ratio (energy in the light channel / energy in the phonon channel), while on the horizontal axis the energy in the phonon channel is given. Taking a quenching factor of 7.4 from the proof-of-principle experiment for nuclear recoils, the region below the dashed curve will contain 90 % of the nuclear recoils. The corresponding acceptance band for QF value of 14.2 (from the mass spectrometer measurement for oxygen ions) is shown as the dotted line. Taking a quenching factor of 40 for tungsten, as measured with the ion beam technique, the region below the solid line will contain 90 % of tungsten recoils. The vertical lines indicate the energy range used for the WIMP analysis.

channel), while on the horizontal axis the energy in the phonon channel is given. The points with negative energy arise in the pulse fitting procedure when a negative amplitude results for small pulses close to the noise. The determination of a nuclear recoil acceptance region in the phonon-light plane is based on a knowledge of the quenching factor. For this calculation the quenching factor Q=7.4 was used. Then, assuming Gaussian fluctuations parameterized with the energy resolution of the light and phonon channels, the dashed line on the plot of Fig. 5.58 gives the boundary below which 90 % of the nuclear recoils are expected. Finally, an analysis threshold of 12 keV was chosen in order to stay well above the energy where electron and nuclear recoil bands intersect. The

upper energy for the analysis was chosen to be 40 keV, since due to the suppression of higher energy recoils by form factor effects, more than 95 % of all WIMP induced tungsten recoils are expected below this energy for any WIMP mass. Thus, nuclear recoil acceptance region on the plot of Fig. 5.58 is below the dashed line and from 12 to 40 keV in the phonon or total energy channel. In this acceptance region there are a total of 7 events. To check on systematic effects due to the uncertainty of the quenching factor upon varying QF that the number of recoils below the 90% acceptance line remains the same 7 counts for quenching factors in the range from 6.7 to 11.1. Higher values of QF will lead to stronger limits. Most of these events for Q = 7.4 are in the region expected for neutron-induced recoils. Furthermore, Monte Carlo simulations for CRESST setup without neutron shielding [Wul04a] yield an estimate for the neutron background of about 0.6 events/(kg day) for $12\,keV < E_{recoil} < 40\,keV$, in reasonable agreement with observed 0.65 events/(kg day). A limit calculated for coherent ("spin independent") interactions, assuming a standard halo model[14]. The Helm spin-independent form factor was used for the nucleus [Hel56] with the parametrization suggested in Ref. [Lew96b] and A^2 scaling for coherence. The dashed line in Fig. 5.59 shows this limit calculated with the optimum interval method of Ref. [Yel02], together with the DAMA (1-4) 3σ signal region [Ber04a] and exclusion limits from EDELWEISS [Ben02] and CDMS [Col04b].

In the above discussion a global limit on the light yield to identify nuclear recoils was applied. Further, important improvements in CRESST technique are to be anticipated if it were possible to use the information from the phonon-light output to identify which particular nucleus is recoiling. For neutrons in this recoil energy range CRESST Monte Carlo simulation shows that the dominant scattering in the $CaWO_4$ is on the oxygen, with less than 5% of the nuclear recoils due to tungsten. Hence, the QF value derived from the neutron scattering experiments (proof-of-principle experiment see section 2.7.1) is essentially determined by oxygen recoils. On the other hand for coherently interacting WIMPs the scattering is dominated by the tungsten, and a much higher value of QF applies. Taking the measured quenching factor of 40 for tungsten[15], the region below the solid line in figure 5.58 will contain 90 % of the tungsten recoils. A particulary strong limit for WIMPs with coherent scattering results from selecting a region in the phonon-light plane corresponding to tungsten recoils. Here, no events have been observed in the data shown in Fig. 5.58. The exclusion limit obtained this way for spin independent scattering is shown in figure 5.59 - the solid line.

[14]Isothermal halo, WIMP characteristic velocity: 220 km/s, mean Earth velocity: 232 km/s, local WIMP density: 0.3 GeV/c^2/cm^3.

[15]For the energy region of interest (12-40 keV) constant value QF = 40 was assumed. As previously discussed the horizontal character of ^{206}Po recoil events (see Fig. 5.53) from the Run 27 indicates the constancy of the QF with energy, for energies below 100 keV.

The dependence of the exclusion limit on different values of QF for tungsten was tested. The number of events below the solid curve in figure 5.58 remains at zero for quenching factors down to QF = 35.8 where an event at 22.2 keV shows up below the line. This single event would move the minimum of exclusion curve from 1.6×10^{-6} pb to 2.3×10^{-6} pb. The result is then stable down to QF = 23.4, where a second event at 13.5 keV occurs and would move the minimum of the exclusion plot up to 3.8×10^{-6} pb. This confirms the stability of the results against uncertainties in the value of the quenching factor for tungsten.

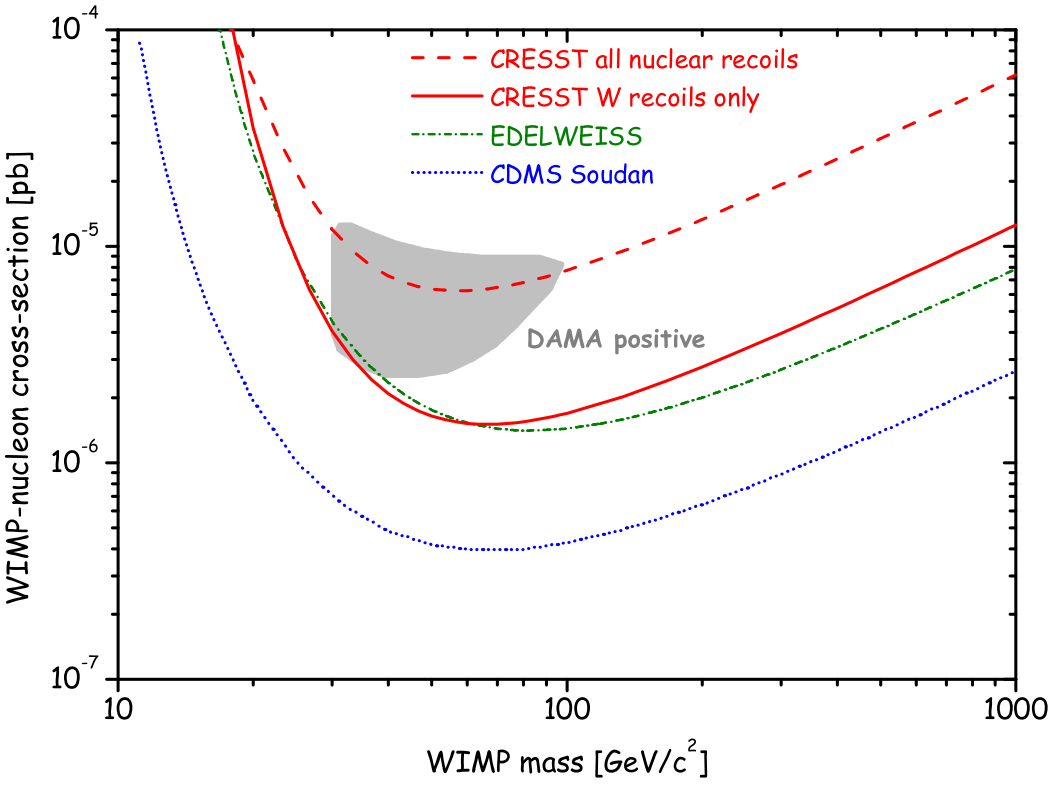

Figure 5.59: Exclusion limits from the Dark Matter run for WIMPs with spin-independent interaction. The dashed curve is obtained when all nuclear recoils with a quenching factor higher then 7.4 are interpreted as WIMPs. The measured quenching factor for tungsten in $CaWO_4$ allows the identification of WIMP interaction at tungsten nuclei. The solid line is the limit obtained when only tungsten recoils with QF=40 as measured in this work are considered. The regions above the curves are excluded at 90 % CL. The filled region represents the claim of a positive WIMP signal by the DAMA collaboration [Ber04a]. For comparison recent exclusion limits of the EDELWEISS collaboration [Ben02] and of the CDMS collaboration [Col04b] are shown.

Chapter 6

Conclusions and Perspectives

Despite overwhelming indirect evidence for the existence of Dark Matter in the Universe, the direct detection and an understanding of the nature of Dark Matter remain the outstanding challenges of present day physics and cosmology. Astronomical observations and astrophysical data have yielded detailed information on the composition of the Universe. While baryonic matter contributes only 4% to the density of the Universe, Dark Matter constitutes a much larger fraction of about 26%. The remaining 70%, needed to close the Universe, are attributed to a so far unknown form of energy, the so-called Dark Energy. The Dark Matter may consist of Weakly Interacting Massive Particles (WIMPs). Supersymmetry provides a well-motivated WIMP candidate in the form of the lightest supersymmetric particle. WIMPs are expected to be gravitationally bound in an approximate isothermal halo around the visible part of our galaxy with a density of ~ 0.3 GeV/cm^3 at the position of the Earth [Jun96]. Interaction with ordinary matter is expected via elastic scattering on nuclei which, for the spin-independent case, should be coherent with all nucleons in a nucleus resulting in a cross-section rising in proportion to A^2 and therefore preferring heavy nuclei [Jun96]. The energy transferred to tungsten nuclei reaches up to about 40 keV and the expected rates are below 1 event/kg/day.

The goal of the CRESST Phase II experiment is to detect WIMP Dark Matter particles via elastic scattering off nuclei. Cryogenic detectors based on 300 g scintillating $CaWO_4$ target crystals are being developed. A very efficient discrimination of nuclear recoils from radioactive γ and β backgrounds down to recoil energies of about 10 keV is achieved by simultaneous detection of phonons and light [Meu99]. Additional passive shielding is achieved by the use of a shielded low background cryostat located deep underground in the Laboratorio Nazionale del Gran Sasso (LNGS).

In this work the scintillation properties, being of crucial importance for the background rejection efficiency of direct Dark Matter searches based on phonon-light detection, and the radiopurity of $CaWO_4$ crystals of different origin were studied. The radiopurity of both the raw materials and the grown crystals was measured. A low level of radioactive contamination from the natural decay chains, ($\simeq 100\,\mu$Bq/kg) was obtained for 300 g ($\varnothing = 40$ mm, h = 40 mm) $CaWO_4$ crystals.

Extensive studies of the influence of different parameters and conditioning procedures (geometry, thermal and surface treatments) on the light yield of $CaWO_4$ crystals have been carried out resulting in a significantly improved reproducibility of the scintillation quality. The effect of small changes of the geometry of the crystals and the influence of different surface treatments on the energy resolution and the light output of the crystals was tested and an energy resolution $\Delta E/E \approx 8\%$ at E = 662 keV was obtained for some of the best samples. The influence of thermal processing in different atmospheres on the scintillation properties of $CaWO_4$ was studied leading to a substantial improvement of both the light yield and resolution.

Furthermore, the light collection of the detector modules for CRESST Phase II was optimized. Scintillating high reflectivity foil was tested and its scintillation properties were studied. The use of scintillating foil significantly reduces the amount of non-scintillating material in the immediate vicinity of the absorber. Radioactive decays in non-scintillating materials in the vicinity of the absorber can produce potentially dangerous backgrounds that could mimic WIMP signals. Scintillating paint to cover the remaining non-scintillating material will be tested in near future.

The quenching of the scintillation light emitted as a result of nuclear recoils is the key for efficient background rejection in cold Dark Matter particle detectors that utilize scintillators. A new and powerful method of measurement of quenching factors (ratio of the light yields of electron recoils and of nuclear recoils of the same energy) was developed. It relies on the measurement of the number of photons produced when the scintillating crystal is bombarded by different ions. The method allows to measure quenching factors for a wide range of different elements and scintillating absorbers. Using this technique the quenching factor of tungsten in $CaWO_4$ was measured for the first time. The high quenching factor of 40 for tungsten recoils, measured at room temperature, gave a particulary strong upper limit for the coherent scattering of WIMPs.

In order to measure quenching factors at low temperatures first tests have been performed using a He cryostat. Further improvements of the existing setup are necessary and will be tested in the near future. Yet, simultaneous phonon-light

measurements of α decay processes with a heavy daughter nucleus (^{206}Pb) measured at low temperature ($\simeq 10\,mK$) indicate no substantial change of quenching factors of heavy ions with temperature.

The upgrade of the CRESST experimental setup with 66 channel SQUID readout system will allow the installation of 33 detector modules providing $10\,kg$ of target material. Together with the recently installed neutron shield and the muon veto this should enhance the sensitivity of CRESST's to WIMP Dark Matter interactions by two orders of magnitude. Identification of recoiling nuclei, developed within this work, offers practically multiple target choice within one absorber crystal that offers examination of a wider WIMP mass range and provides additional sensitivity. In the case of a positive Dark Matter signal the different recoil energy spectrum of the absorber nuclei give a unique signature and a powerful tool for further identification and verification of properties.

Appendix A

High Purity Germanium γ-spectroscopy measurements - HPGe

Table A.1: $CaCO_3$ powders

	Source	**Alfa Aesar**		**Ukraine**		**Karat**	**China**
	Measured in	F	GS	F	GS	F	GS
	Sample mass [g]	25.81	25.81	35.39	36.39	33.35	21.8
	Live time [h]	156.8	412.823	48.5	67.03	71.2	229.41
Decay chain	**Nuclide**						
	^{137}Cs		<5		<26		<11
	^{60}Co		<12		<31		<15
	^{40}K	<120	<99		<300	<150	<172
^{238}**U**	^{234}Th	<45	<69		<781		
	^{234m}Pa		<516		<3600		
	^{226}Ra		<15		4600±800		1800±300
	^{214}Pb	<11		3900±200		2200±150	
	^{214}Bi	<10		3800±200		2000±150	
	^{210}Pb	200±90	<6000	1300±300	<40000	500±300	<16000
^{232}**Th**	^{228}Ac						71±16
	^{212}Pb	<7	<15		<53		
	^{208}Tl	13±8		400±100		30±20	
^{235}**U**	^{235}U	<27	<2		<40		<15

- **F** - Measurement performed in Modane (France); activity is given in mBq/kg; 90% CL limits; $1\,\sigma$ errors;
- **GS** - Measurement performed in Gran Sasso (Italy); activity is given in mBq/kg; 95% CL limits; $1\,\sigma$ errors;

Table A.2: WO_3 powders

	Source	**Alfa Aesar**		**Ukraine**		**Karat**	**China**
	Measured in	F	GS	F	GS	F	GS
	Sample mass [g]	56.63	56.63	59.0	59.0	49.90	58.0
	Live time [h]	164.75	391.95	230.85	388.246	92.95	357.85
Decay chain	**Nuclide**						
	^{137}Cs	<2	41±7	21±3	27±6	410±90	<4
	^{60}Co	5±4	<8	<2	<2		<4
	^{40}K	110±40	<90	270±40	470±93	370±80	<63
^{238}**U**	^{234}Th	<780		<720			<224
	^{234m}Pa	<510		<450			<1800
	^{226}Ra		<24		<20		
	^{214}Pb	<8		12±10		<60	
	^{214}Bi	<8		13±6		<12	
	^{210}Pb	<800	<184000	<380	<2kBq/kg	<450	<1kBq/kg
^{232}**Th**	^{228}Ac	<13					
	^{212}Pb	13±6	<22		<19		<12
	^{208}Tl	<11				12±9	
^{235}**U**	^{235}U		<17		<13		<2

- **F** - Measurement performed in Modane (France); activity is given in mBq/kg; 90% CL limits; $1\,\sigma$ errors;
- **GS** - Measurement performed in Gran Sasso (Italy); activity is given in mBq/kg; 95% CL limits; $1\,\sigma$ errors;

Table A.3: $CaWO_4$ crystals

	Description	**Alexej III** (Ukrainian)	**Godebert** (Ukrainian)	**Berta** (Russian)	**Elena** (Russian)	**Gloria** (Russian)	**K01** (Karat)	**Ch01** (Chinese)
	Measured in	GS	GS	F	GS	F	F	F
	Sample mass [g]	299.6	299.6	24.45	300	307	301.95	21.5
	Live time [h]	403.708	450.840	232.4	428.387	253	135.9	206.75
Decay chain	**Nuclide**							
	^{137}Cs	<2	<2	4±3	<2	<1	<4	<2
	^{60}Co	<1	<1	<5	<2	<3	6±2	6±4
	^{40}K	<16	18±10	260±70	<19	<17	110±30	<701
	^{176}Lu							12±4
^{238}**U**	^{234}Th			<500		<125	<300	<300
	^{234m}Pa	95±42	<59		<90			
	^{226}Ra	10±3	13±2		<6			
	^{214}Pb			<20		<5	21±6	<10
	^{214}Bi			<30		<4	29±8	<20
	^{210}Pb	<4000	<3600	<1100	<2000	860±430	1500±600	<700
^{232}**Th**	^{228}Ra	<2	<2				<4	<10
	^{212}Pb			<30	<4	<4	12±7	<7
	^{208}Tl			<20		<2	<3	<20
^{235}**U**	^{235}U	<2	<2	<10	<2	<4	<7	<10

- **F** - Measurement performed in Modane (France); activity is given in mBq/kg; 90% CL limits; 1 σ errors;
- **GS** - Measurement performed in Gran Sasso (Italy); activity is given in mBq/kg; 95% CL limits; 1 σ errors;

Appendix B

Inductively Coupled Plasma Mass Spectroscopy measurements - ICP-MS

ICP-MS measurements have been performed in the chemistry laboratory of the Gran Sasso laboratory in Italy and in the Durham University chemical laboratory in the United Kingdom.
A series of measurements have been performed in order to understand the dissolving process and to get more accurate results. Semi-quantitative results of the measurements of the samples from the ingots of the crystals are presented in the following tables:

- **UK** - Measurement performed in Durham University (UK);
- **GS** - Measurement performed in Gran Sasso (Italy)

Table B.1: **Agnes (Russian) measurements**

Description	**Agnes**			
Measured in	GS	GS	UK	UK
Preparation	125mg in 50ml HNO_3 dilution 1:1	125mg dissolved at 180° in 50ml HNO_3 dilution 1:5	Dissolved at room temperature for a week in HF+HNO_3 1:1	Dissolved at room temperature for a week in HNO_3
Natural element	**[ppb]**	**[ppb]**	**[ppb]**	**[ppb]**
Li	11	< 25		
B	72000	92000		
Na	30000	8800		
Mg	3000			
Al	7800	9000		
Si	57000	71000		
K	4500	9400		
Sc	21	< 88		
Ti	150	< 880		
Cr	220	< 480	1280	1050
Mn	97	130		
Fe	22000	29000		
Co	56	100		
Ni	330	470	2530	1950
Cu	100	130		
Zn	240	540	6220	4570
Ga	220	310		
As	< 31	< 380		
Se	1400	4200		
Sr	14000	16000	31160	26230
Y	5500	6800	12980	10350
Zr			430	
Mo	48	< 140		
Te	< 46	< 570		
I	44	170		
Cs	3.9	< 16		
Ba	16000	19000	27600	35080
La	28	45	50	50
Ce	37	40	30	20
Pr	3	< 9	10	10
Nd	640	750	1720	1460
Sm	15	< 51		
Eu	< 1	< 13		
Gd	3500	4400	10420	8310
Er	1300	1700	6440	5110
Yb	76	97	210	150
Lu	20	26	50	40
Hf	15	< 22		
Pb	200	270		
Bi	13	20		

Table B.2: **Berta and Elena (Russian) measurements**

Description	**Berta**			**Elena**
Measured in	UK	UK	UK	GS
Preparation	Dissolved at room temperature for a week in $HF+HNO_3$ 1:1	Dissolved at room temperature for a week in HNO_3	Dissolved in $HF+HNO_3$ evaporated and prepared in HNO_3	112.5mg dissolved in microwave + 10ml HNO_3c. in 50ml
Natural element	**[ppb]**	**[ppb]**	**[ppb]**	**[ppb]**
Li				11
B				5200
Na			169840	16000
Mg				1500
Al				4600
Si				8000
Sc				15
Ti				130
Cr				300
Mn				150
Fe				60000
Co			170	200
Ni			435	5600
Cu	1270	2250		62
Zn	3660		5640	600
Ga				62
As				< 28
Se				110
Sr	24480	22700	20915	2100
Y	8510	7140	6665	850
Zr	230		125	
Mo			8030	38
Te			520	< 56
Ba	30490	35350	6930	2600
La	50	50		44
Ce	50	30		25
Pr	10			1.3
Nd	980	860	780	1100
Sm	70	20		< 5.8
Eu	10	10		< 1.5
Gd	5760	5000	4655	1000
Er	4170	3490	2315	940
Yb	130	110	90	62
Lu	40	40		6.9
Hf				< 2.9
Pb				84
Bi				8.2

Table B.3: **Conrad (Ukrainian) measurements**

Description	**Conrad**		
Measured in	UK	UK	UK
Preparation	Dissolved at room temperature for a week in $HF+HNO_3$ 1:1	Dissolved at room temperature for a week in HNO_3	Dissolved in $HF+HNO_3$ evaporated and prepared in HNO_3
Natural element	**[ppb]**	**[ppb]**	**[ppb]**
Na			67165
Al			1565
Co			185
Ni			510
Cu	1720	130	
Zn	3510		6225
As			115
Sr	85110	72400	64570
Y	180	150	115
Zr	50		
Mo			9975
Te			470
Ba	31270	3796	6415
La	10		
Ce	60	30	
Nd	20	10	
Sm	20		
Eu	1	10	
Gd	550	430	400
Pb		870	

Table B.4: **Karat crystals measurements**

Description	**KARAT**		
	K08	**K09**	**K11**
Measured in	UK	UK	UK
Preparation	Dissolved in HF+HNO_3 evaporated and prepared in HNO_3		
Natural element	**[ppb]**	**[ppb]**	**[ppb]**
Na	53500	23870	89555
Al	1630	1035	2500
Sc	450	370	315
Cr	520		175
Mn		125	110
Co	185	210	205
Ni	3330	405	1355
Cu		125	
Zn	16260	7735	6530
As	160	360	175
Sr	1195	1415	1485
Y	100	140	140
Mo	17195	14575	15900
Cd		110	65
Te	675	630	630
Nd		65	
Gd		65	
Re		55	50

Table B.5: **Chinese crystal measurement**

Description	**Chinese** Ch01
Measured in	UK
Preparation	Dissolved in HF+HNO_3 evaporated and prepared in HNO_3
Natural element	**[ppb]**
Na	10180
Co	200
Ni	385
Zn	7865
As	80
Sr	49310
Y	195
Mo	7935
Te	335
Lu	230

Appendix C

Deflection plate parameters

A list of the time constants of the deflection plates determined for the selection of ions using MCP measurements is given in table C.1. Additionally, the materials used as target material for the the quenching factor measurements are listed.

Table C.1: Deflection plate parameters.

Element	**Z**	**A**	**Abundance(s)**	**TOF** [μs]	**C** [μs]	**D** [μs]	**Target material**
H	1	1.008	99.98%	0.916	0.1	0.1	Stainless Steel
Be	4	9.012	100.0%	2.96	1.0	0.3	CuBe
O	8	15.995	99.76%	4.15	1.6	0.1	$CaWO_4$
Si	14	27.977 28.977 29.974	92.23% 4.67% 3.10%	5.62 5.70 5.86	2.3	0.2	Stainless Steel
Ca	20	39.963	96.94%	6.50	2.6	0.1	$CaWO_4$
Cu	29	62.930 64.928	69.17% 30.83%	8.05 8.16	3.1	0.4	CuBe
Y	39	88.906	100.0%	9.61	3.7	0.4	Y foil
Ag	47	106.905 108.905	51.84% 48.16%	10.7 10.8	4.1	0.4	Ag foil
Sm	62	143.912 146.915 147.915 148.918 149.917 151.920 153.922	3.1% 15.0% 11.3% 13.8% 7.4% 26.7% 22.7%	12.34 12.41 12.48 12.51 12.55 12.67 12.75	4.7	0.4	Sm foil
W	74	181.948 182.950 183.951 185.954	26.50% 14.31% 30.64% 28.43%	13.75 13.84 13.93 14.05	5.2	0.4	CuW or $CaWO_4$
Au	79	196.967	100.0%	14.41	5.6	0.4	Au foil

Appendix D

SRIM2003 Simulation

The process of ions impinging onto a $CaWO_4$ crystal was simulated using the program package SRIM2003 (The Stopping and Range of Ions in Matter version 2003) [SRI]. SRIM is a group of programs which calculates the stopping and the range of ions (up to 2 GeV/amu) in matter using a quantum mechanical treatment of ion-atom collisions (assuming a moving atom as an "ion", and all target atoms as "atoms"). This calculation is made very efficient by the use of statistical algorithms which allow the ion to make jumps between calculated collisions and then averaging the collision results over the intervening gap. During the collisions, the ion and atom have a screened Coulomb interaction, including exchange and correlation interactions between the overlapping electron shells. The ion has long range interactions creating electron excitations and plasmons within the target. These are described by including a description of the target's collective electronic structure and interatomic bond structure when the calculation is setup (tables of nominal values are supplied). The charge state of the ion within the target is described using the concept of an effective charge, which includes a velocity dependent charge state and long range screening due to the collective electron sea of the target. Main improvements in the last version of this program, SRIM2003, are new theoretical calculations with emphasis on lower energies and on the stopping of heavy ions. The accuracy of SRIM2003 stopping power calculations is also significantly improved. When compared to experimental data, the percentage of data points within 5% and within 10% of the SRIM2003 calculations are 69% and 86% respectively.
The calcium tungstate crystal target material was defined as a solid target with a density of 6.116 g/cm^3. Ions were selected with a fixed initial energy and normal incidence angle. Full cascades[1] have been simulated for all selected ions of the initial energy 18 keV. The total number of simulated ions was 10000.

[1]Detailed Calculation with full Damage Cascades is a mode in which simulation follows every recoil until its energy drops below the lowest displacement energy of any target atom.

The iteration starts with a certain rate of energy loss of the ion to the target electrons, i.e. the electronic stopping power. Then, the target atom that is hit and starts a recoil cascade is identified, along with its recoil energy. Each cascade is then divided into displacement collisions, vacancy production, replacement collisions and interstitial atoms, as described below.
The number of displacement collisions indicates how many target atoms were set in motion in the cascade with energies above their displacement energy. A vacancy is defined as the hole left behind when a recoil atom moves from its original site. Replacement collisions, are processes which reduce the number of vacancies. If a moving atom strikes a stationary target atom and transfers more than its displacement energy to it, and the initial atom, after the collision, does not have enough energy to move onwards, and it is the same element as the atom it struck, then it just replaces that atom in the target and there is no vacancy created. This mechanism may reduce the total vacancies by up to 30%. The summation goes as

$$\text{Displacements} = \text{Vacancies} + \text{Replacement Collisions}\,.$$

Finally, when a recoil atom stops, and is not a replacement atom, then it becomes an interstitial. These may be summed as

$$\text{Vacancies} = \text{Interstitials} + (\text{Atoms which leave the target volume})$$

An atom that leaves the target volume is no longer followed. That is, if it leaves the target front surface or the rear surface, it is discarded. So, vacancies occur within the target, and the final resting place of a moving recoil atom can be some distance from its vacancy. If the recoil leaves the target, clearly the sum of interstitials will be less than the number of vacancies by the loss of that atom. Replacement collisions are not part of this equation because each replacement collision reduces the number of vacancies and the number of interstitials by one, leaving the equation in balance.
A number of different output parameters are listed and here only some of them will me mentioned. The program assumes that there is cylindrical symmetry in the final ion distributions. The assumed cylindrical axis is perpendicular to the target surface at the point of ion impact. (This is correct only if the initial ion beam is normal to the target surface). The "radial" parameters refers to these cylindrical coordinates. The "projected" parameters assumes that an X-Y plane has been inserted through the axis, and the final ion distribution is projected onto this plane.
Figure D.1 illustrates difference in the range and number of vacancies produced per ion for ions of different masses. Summary results concerning the range and total energy losses for selected ions are given in table D.1.
Selecting a group of backscattered ions and studying their kinetics gives the energy of them at the moment when they left the target. The difference between

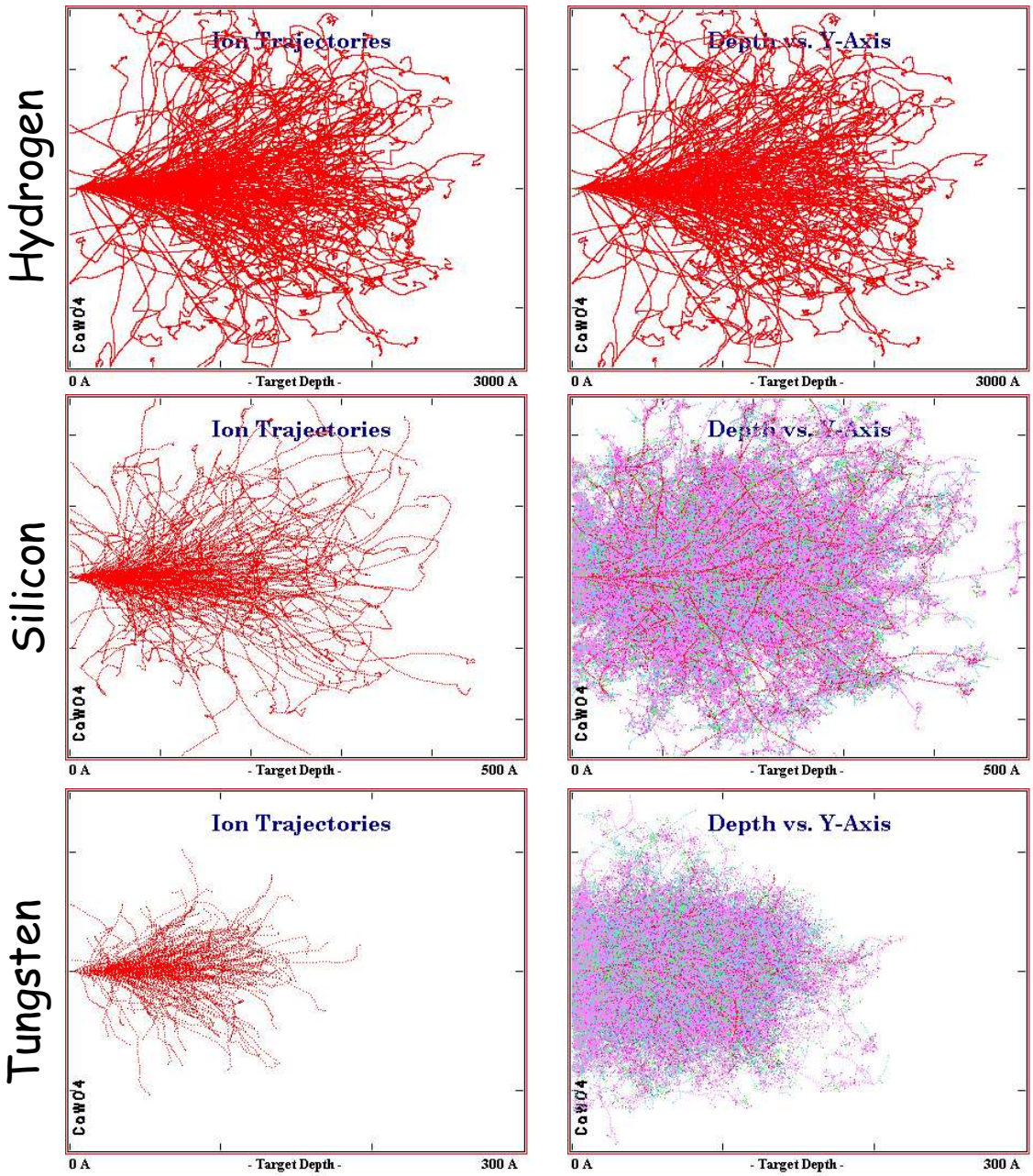

Figure D.1: Projected ranges for three different ions. Left: Trajectories of the ions; Right: Trajectories of both ions and atoms of the target material. Following color code applies: red color represents ion trajectories, green calcium atoms trajectories, blue the ones of tungsten atoms and pink is associated with oxygen.

the initial and calculated energy then gives total deposited energy. Number of backscattered ions on a sample of 10000 simulated ones is also in table D.1 (last column). With an exception of hydrogen the probability for the backscattering

is decreasing with an increase of mass of the ions going down to < 5 promil for tungsten. Figure D.2 shows the distribution of the energy deposited by the backscattered ions in the $CaWO_4$ target that have been used for the data analysis.

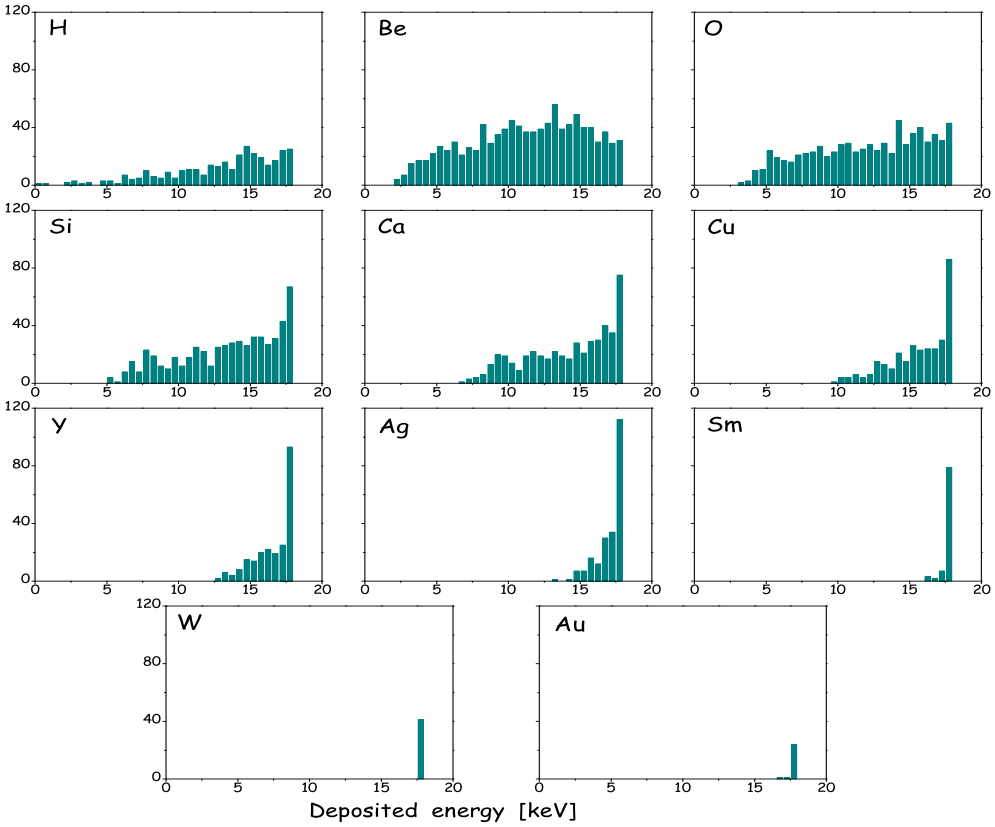

Figure D.2: Energy distribution of the deposited energy from the backscattered ions in the $CaWO_4$ target using the SRIM2003 simulation. The used bin width corresponds to 0.5 keV.

Table D.1: Summary results from the SRIM2003 simulation.

Element	**Range**			**Energy Loss** [%]									Number of backscattered ions
				Ionization			Phonons			Vacancies			
	Longit. [nm]	Lateral [nm]	Radial [nm]	Ions	Recoils	Total	Ions	Recoils	Total	Ions	Recoils	Total	
H	160.5	55.0	86.2	96.25	0.38	96.63	1.36	1.9	3.26	0.07	0.05	0.12	330
Be	65.7	31.7	50.4	42.22	11.94	54.16	4.08	39.19	43.27	0.61	1.96	2.57	1014
O	31.1	14.1	22.1	28.25	16.81	45.06	3.0	48.7	51.7	0.56	2.68	3.24	734
Si	18.9	7.8	12.1	16.6	20.73	37.33	2.44	56.43	58.87	1.06	2.75	3.81	573
Ca	14.7	5.6	8.8	9.85	22.75	32.6	2.18	61.06	63.24	0.52	3.64	4.16	482
Cu	12.2	4.3	6.7	3.7	24.12	27.82	2.0	65.65	67.65	0.54	3.98	4.52	312
Y	10.6	3.5	5.5	4.28	23.67	27.95	1.77	65.7	67.47	0.55	4.04	4.59	229
Ag	9.9	3.2	4.9	5.71	23.1	28.81	1.61	65.01	66.62	0.55	4.02	4.57	220
Sm	9.7	3.0	4.7	2.83	23.28	26.11	1.45	67.65	69.1	0.58	4.2	4.78	91
W	9.4	2.7	4.3	6.32	22.19	28.51	1.26	65.58	66.84	0.57	4.07	4.64	41
Au	9.4	2.7	4.2	6.82	21.96	28.78	1.21	65.38	66.59	0.58	4.05	4.63	26

Bibliography

[3M] 3M, http://www.mmm.com/lightmanagement/

[Abr02] D. Abrams et al., Exclusion Limits on the WIMP-Nucleon Cross-Section from the Cryogenic Dark Matter Search, *submitted to Phys.Rev.D*

[Abu00] R. Abusaidi et al., Exclusion Limits on the WIMP-Nucleon Cross Section from the Cryogenic Dark Matter Search, *Phys. Rev. Lett.* **84** (2000) 5699

[Alc00] C. Alcock et al., The MACHO Project: Microlensing Results from 5.7 Years of LMC Observations, *Ap. J.* **542** (2000) 281–307

[Ale98] A. Alessandrello et al., Measurements of internal radioactive contamination in samples of Roman lead to be used in experiments on rare events, *Nucl. Instr. and Meth.* **142** (1998) 163–172

[Alp48] R. Alpher, R. Herman, G. Gamow, The Evolution of the Universe, *Nature* **(162)** (1948) 774–775 and 680–682

[Ang02] G. Angloher, et al., Limits on WIMP Dark Matter using Sapphire Cryogenic Detectors, *Astropart.Phys.* **18** (2002) 43–55

[Ang04] G. Angloher, et al., J. Ninkovic, CRESST-II: Dark Matter search with scintillating absorber, *Nucl. Instr. and Meth.* **(A520)** (2004) 108–1112, Proc. LTD-10

[Apr04] E. Aprile et al., The XENON Dark Matter Search Experiment, *Preprint* **astro-ph/0407575** (2004)

[Arn99] F. Arneodo et al., Neutron background measurements in the ICARUS area at the underground Gran Sasso Laboratory, Preprint, 1999

[Arp92] C. Arpesella, Background Measurements at Gran Sasso Laboratories, *Nuclear Physics B (Proc. Suppl.)* **28A** (1992) 420

[Bah92] J. N. Bahcall, C. Flynn, A. Gould, Local Dark Matter from a Carefully Selected Sample, *Astrophys. J.* **389** (1992) 234

[Bau98] L. Baudis et al., GENIUS: a new Dark Matter project, *Phys. Rep.* **307** (1998) 301

[Bau99] L. Baudis et al., New Limits on Dark Matter WIMPs from the Heidelberg-Moscow Experiment, *Phys. Rev.* **D59** (1999) 022001

[Bea62] G.B. Beard et al., Temperature dependent luminescence of $CaWO_4$ and $CdWO_4$, *J. App. Phys.* **33(1)** (1962) 144–147

[Bed97] V. Bednyakov, H.V. Klapdor–Kleingrothaus, S.G. Kovalenko, Superlight neutralino as a Dark Matter particle candidate, *Phys. Rev.* **D 55** (1997) 503

[Bel85] E. Bellotti et al., New Measurement of Rock Contaminations and Neutron Activity in the Gran Sasso Tunnel, *INFN/TC-85/19*

[Ben02] A. Benoit et al., Improved Exclusion Limits from the EDELWEISS WIMP Search, *Phys. Lett.* **B545** (2002) 43–49

[Ber99] R. Bernabei et al., On a further search for a yearly modulation of the rate in particle Dark Matter direct search, *Phys. Lett.* **B450** (1999) 448

[Ber00] R. Bernabei et al., Search for WIMP Annual Modulation Signature: Results from DAMA, *Phys. Lett.* **B480** (2000) 23–31

[Ber04a] R. Bernabei et al., DAMA/NaI results, *Preprint* **astro-ph/0405282** (2004)

[Ber04b] G. Bertone, D. Hooper, J. Silk, Particle Dark Matter:Evidence, Candidates and Constraints, *Preprint* **hep–ph/0404175** (2004)

[Bir64] J.B. Birks, *The theory and practice of scintillating counting*, Pergamon press, 1964

[Bla83] G. Blasse, G. Bokkers, Low temperature Decay Time Measurements on the Luminescence of Calcium Tungstate ($CaWO_4$), *J Solid State Chem* **(49)** (1983) 126–128

[Bla94] G. Blasse, Grabmaier B., *Luminescence materials*, Springer-Verlag, Heidelberg, 1994

[Böh80] M. Böhm et al., Thermally and optically simulated processes in X-irradiated scheelite type crystals, *J. de Physique* **41** (1980) 3810–3829

[Büh96] M. Bühler et al., Status and Low Background Considerations for the CRESST Dark Matter Search, *Nucl. Instr. and Meth.* **A370** (1996) 237

[Bur95] A. Burkert, The structure of Dark Matter Halos in Dwarf Galaxies, *Ap. J.* **447** (1995) L25–L28

[Car99] R.G. Carlberg et al., The Omega-M - Omega-Lambda Dependence of the Apparent Cluster Omega, *Ap. J.* **516** (1999) 552

[Chr04] P. Christ, Rutzinger S. et al., High detection sensitivity achieved with cryogenic detectors in combination with matrix-assisted laser desorption/ionization time-of-flight mass spectrometry, *Eu. J. Mass Spec.* **(10)** (2004) 469–476

[col04a] CAST collaboration, First results from the CERN Axion Solar Telescope, *Preprint* **hep-ex/0411033** (2004)

[Col04b] CDMS Collaboration, First Results from the Cryogenic Dark Matter Search in the Soudan Underground Lab, *Preprint* **astro-ph/0405033** (2004)

[Cop03] C.J. Copi, L.M. Krauss, Comparing WIMP Interaction Rate Detectors with Annual Modulation Detectors, *Phys.Rev.Lett. D* **67** (2003) 103507

[Coz03] C. Cozzini, *CRESST Dark Matter Search with Cryogenic Calorimeters*, PhD thesis, Ludwig-Maximilians-Universität München, 2003

[Coz04] C. Cozzini, et al., J. Ninkovic, Detection of the Natural Alpha Decay of Tungsten, *to be published in Phys. Rev. C*

[Dav85] M. Davis, G. Efstathiou, C. S. Frenk, S. D. M. White, The evolution of large-scale structure in a universe dominated by cold Dark Matter, *Ap.J.* **292** (1985) 371–394

[Der92] S.E. Derenzo, W.W. Moses, In *Proceedings of the CRYSTAL 2000 International Workshop on Heavy Scintillators for Scientific and Industrial Applications*. Charmonix, France, 1992

[Die68] G.H. Dieke, *Spectra and Energy Levels of Rare Earth Ions in Crystals*, John Wiley & Sons, 1968

[Dod94] S. Dodelson, L. Widrow, Sterile Neutrinos as Dark Matter, *Phys.Rev.Lett.* **72** (1994) 17–20

[Eis87] M. Eisenbud, *Environmental Radioactivity*, Academic Press, Inc., 3. Edition, 1987

[Eng92] J Engel, Nuclear Form Factors for the Scattering of Neutralinos, *Nucl. Physics B (Proc. Suppl.)* **28A** (1992) 310–313

[Fal94] T. Falk, K.A. Olive, M. Srednicki, Heavy sneutrinos as Dark Matter, *Phys. Let. B* **(339)** (1994) 248–251

[Fra02] T. Frank, *Development of Scintillating Calorimeters for Discrimination of Nuclear Recoils and Fully Ionizing Events*, PhD thesis, Technische Universität München, 2002

[Fre88] K. Freese, J. Frieman, A. Gould, Signal Modulation in Cold Dark Matter Detection., *Phys. Rev.* **D 37** (1988) 3388

[Fuk98] M Fukugita, C.J. Hogan, P.J.E. Peebles, The Cosmic Baryon Budget, *Ap.J.* **(503)** (1998) 518–530

[Gai] R. Gaitskell, V. Mandic, Direct Detection of WIMP Dark Matter, Sensitivity Plots, web link http://dmtools.berkeley.edu/limitplots/

[Glu73] M. Gluyas, F.D. Hughes, B.W. James, The elastic constants of calcium tungstate 4.2-300K, *J. Phys. D* 6

[Gon04] P. Gondolo, Non-Baryonic Dark Matter, *Preprint* **astro–ph/0403064** (2004)

[Goo85] M. W. Goodman, E. Witten, Detectability of certain Dark Matter candidates., *Phys. Rev.* **D 31** (1985) 3059

[Gra75] R. Grasser, E. Pitt, A. Scharmann, G. Zimmerer, Optical properties of $CaWO_4$ and $CaMoO_4$ crystals in the 4 to 25 eV region, *Phys. Stat. Sol. b* **69** (1975) 359

[Gra76] R. Grasser, A. Scharmann, Luminescent sites in $CaWO_4$ and $CaWO_4$:Pb crystals, *J.Luminescence* **12/13** (1976) 473–478

[Gra82] R. Grasser, A. Scharmann, K. Strack, On the intrinsic nature of the blue luminescence in $CaWO_4$, *J.Luminescence* **27** (1982) 263–272

[Gre02] A. M. Green, Calculating Exclusion Limits for WIMP Direct Detection Experiments without Background Subtraction, *Phys. Rev.* **D65** (2002) 023520

[Hah87] T. Hahn, editor, *International Tables of Crystallography*, volume Vol. A, Reidel, Boston, 1987

[Han04] S. Hannestad, Neutrinos in cosmology, *New J. Phys.* 6(108)

[Har02] S.P. Hart et al., Status of Dark Matter searches in the Boulby mine, *Nucl.Phy. B* **110** (2002) 91–93

[Hel56] R.H. Helm, Inelastic and Elastic Scattering of 187-MeV Electrons from Selected Even-Even Nuclei, *Phys. Rev.* **(104)** (1956) 1466

[Heu95] G. Heusser, Low Radioactivity Background Techniques, *Ann. Rev. Nucl. Part. Sci.* **45** (1995) 543

[Hoe02] H. Hoekstra, H.K.C. Yee, M.D. Gladders, Properties of galaxy Dark Matter halos from weak lensing, *New Astron.Rev.* **46** (2002) 767

[Hor92] D. Horn et al., The mass dependance of CsI(Tl) scintillation response to heavy ions, *Nucl. Instr. and Meth.* **A 320** (1992) 273–276

[Hua03] Y. Huang et al., A study of luminescence properties of (Gd^{3+}, Dy^{3+}, Nb^{5+})-doped lead tungstate single crystals, *Optical materials* **23** (2003) 443–447

[Hub29] E. Hubble, A relation between distance and radial velocity among extragalactic nebulae, *Proc. Nat. Acad. Sci.* **(15)** (1929) 168

[Ich93] M. Ichige et al., Operating characteristics of photomultipliers at low temperature, *Nucl. Instr. and Meth.* **A 327** (1993) 144–147

[Jag04a] T. Jagemann, *Measurement of the Scintillation Light Quenching for Nuclear Recoils induced by Neutron Scattering in Detectors for Dark Matter Particles*, PhD thesis, TU München, 2004

[Jag04b] Th. Jagemann, private communication, 2004

[Joc02] J. Jochum et al., Neutron Scattering Facility for the Calibration of the Response to Nuclear Recoils, *AIP Conf.Proc.* **(605)** (2002) 525–528

[Jun96] G. Jungman, M. Kamionkowski, K. Griest, Supersymmetric Dark Matter, *Phys. Rep.* **267** (1996) 195

[Kas98] A. Kashlinsky, Determining Ω from the cluster correlation function, *Phy. Rep.* **307** (1998) 67–73

[Kee02] R. Keeling, *Studies of Scintillators for the CRESST Dark Matter Search*, PhD thesis, Keble College, Oxford, 2002

[Kha02] S. Khalil, C. Munoz, The Enigma of the Dark Matter, *Contemp. Phys.* **43** (2002) 51–62

[Kin97] W.J. Kindt et al., A silicon avalanche photodiode for single optical photon counting in the Geiger mode, *Sensors and Actuators* **A 60** (1997) 98–102

[Kna85] W. Knaak et al., In *Proceedings of the fifth international conference*, volume Springer series in solid-state science, pp. 174–176. Springer Verlag, 1985

[Kno03] R.A. Knop et al., New Constraints on Ω_M, Ω_Λ, and w from an Independent Set of Eleven High-Redshift Supernovae Observed with HST, *Astrophys.J.* **(598)** (2003) 102–137

[Koe93] Cz. Koepke, A. Wojtowicz, A. Lempicki, Excited state apsorption in excimer pumped $CaWO_4$ crystals, *J. Lum.* **(54)** (1993) 345–355

[Kol02] V.N. Kolobanov et al., Optical and luminescent properties of anisotropic tungstate crystals, *Nucl. Instr. and Meth.* **A486** (2002) 496–503

[Kos92] M. Koshiba, Observational neutrino astrophysics, *Phys. Rep.* **(220)** (1992) 229–381

[Kur04] A. Kurylov, M. Kamionkowski, Generalized analysis of weakly-interacting massive particle searches, *Phys. Rev. D* **69** (2004) 063503

[Lew96a] J. D. Lewin, P. F. Smith, Review of mathematics, numerical factors, and corrections for Dark Matter experiments based on elastic nuclear recoil, *Astropart. Phys.* **6** (1996) 87

[Lew96b] J. D. Lewin, P. F. Smith, Review of Mathematics, Numerical Factors, and Corrections for Dark Matter Experiments based on Elastic Nuclear Recoil, *Astropart. Phys.* **6** (1996) 87

[Lin63] J. Linhard, V. Nielsen, M. Scharff, Integral equations governing radiation effects, *Mat. Fys. Medd. Dan. Vid. Selsk.* **33(10)** (1963) 1–42

[Lus94] Ch. Lushchik et al., Multiplication of the electronic excitation in CaO and $YAlO_3$ crystals with free and self-trapped excitons, *J. Physics: Cond. Matter* **6** (1994) 11177–11187

[Mat98] M. Mateo, The Kinematics of Dwarf Spheroidal Galaxies, *Ann. Rev. Astron. Astrophys.* **36** (1998) 435

[Mei00] O. Meier, In *Proc. LTD-8*, volume A444, p. 350. Nucl. Instr. and Meth., 2000

[Meu99] P. Meunier et al., Discrimination between Nuclear Recoils and Electron Recoils by Simultaneous Detection of Phonons and Scintillation Light, *Appl. Phys. Lett.* **75(9)** (1999) 1335

[Nag98] V. Nagirnyi et al., Excitonic and recombination processes in $CaWO_4$ and $CdWO_4$ scintillators under synchrotron irradiation, *Radiation measurements* **29(34)** (1998) 247–250

[Nav96] J.F. Navarro et al., The Structure of Cold Dark Matter Halos, *Ap. J.* **462** (1996) 563–575

[Ost03] J.P. Ostriker, P. Steinhardt, New Light on Dark Matter, *Science* **300** (2003) 1909–1913

[Pap99] L. Papadopoulous, Scintillation response of organic and inorganic scintillators, *Nucl. Instr. and Meth.* **A 434** (1999) 337–344

[Pec77] R.D. Peccei, H.R. Quinn, CP Conservation in the Presence of Pseudoparticles, *Phys. Rev. Lett.* **(38)** (1977) 1440

[Pen66] A.A. Penzias, R.W. Wilson, Determination of the Microwave Spectrum of Galactic Radiation., *Ap.J.* **(146)** (1966) 666–669

[Pet04] F. Petricca, et al., J. Ninkovic, Light detector development for CRESST II, *Nucl. Instr. and Meth.* **(A520)** (2004) 193–196, Proc. LTD-10

[Pet05] F. Petricca, *Dark Matter Search with Cryogenic Phonon-Light Detectors*, PhD thesis, Ludwig-Maximilians-Universität München, 2005

[Prö95] F. Pröbst et al., Model for Cryogenic Particle Detectors with Superconducting Phase Transition Thermometers, *J. of Low Temp. Phys.* **100** (1995) 69

[Raf99] G.G. Raffelt, Particle Physics from Stars, *Ann. Rev. Nucl. Part. Sci.* **49** (1999) 163–216

[Raf00] G.G. Raffelt, Axions and other very light Bosons, *Eur.Phys.J.* **C** (2000) 298–305

[Ram99] Y. Ramachers, Non-Baryonic Dark Matter Searches, *Preprint* astro–ph9911260

[Sad99] B. Sadoulet, Deciphering the nature of Dark Matter., *Rev. Mod. Phys.* **71** (1999) 2

[Sch88] R. Schaeffer, J. Silk, Cold, warm, or hot Dark Matter - Biased galaxy formation and pancakes, *Ap.J.* **332** (1988) 1–16

[Smi68] D.L. Smith, R.G. Polk, T.G. Miller, *Nucl. Instr. and Meth.* **(64)** (1968) 157

[Spe03] D. N. Spergel et al., First Year Wilkinson Microwave Anisotropy Probe (WMAP) Observations: Determination of Cosmological Parameters, *Astrophys.J.Suppl.* **(148)** (2003) 175

[Spi99] M. Spiro, E. Aubourg, N. Palanque-Delabrouille, Baryonic Dark Matter, *Nuclear Physics B (Proc. Suppl.)* **77** (1999) 402–419

[Spo94] N. Spooner et al., The scintillation efficiency of sodium and iodine recoils in a NaI(Tl) detector for Dark Matter searches, *Phys. Lett.* **B 321** (1994) 156–160

[SRI] SRIMgroup, The Stopping and Range of Ions in Matter - SRIM2003, WEB:http://www.srim.org/SRIM/SRIM2003.htm

[Tov98] D. Tovey et al., Measurements of scintillation efficiencies and pulse-shapes for nuclear recoils in NaI(Tl) and CaF_2(Eu) at low energies for Dark Matter experiments, *Phys. Lett.* **B 433** (1998) 150–155

[Tov00] D.R. Tovey et al., A New Model Independent Method for Extracting Spin-Dependent (Cross Section) Limits from Dark Matter Searches, *Physics Letters B* **488** (2000) 17–26

[Wei03] C. Weinheimer, The neutrino mass direct measurements, *Preprint* **hep-ex/0306057** (2003)

[Wul04a] H. Wulandari, J. Jochum, W. Rau, F. von Feilitzsch, Neutron Background Studies for the CRESST Dark Matter Experiment, *preprint* hep-ex/0401032

[Wul04b] H. Wulandari, J. Jochum, W. Rau, F. von Feilitzsch, Neutron flux underground revisited, *preprint* hep-ex/0312050

[Yan03] L. Yang et al., Performance of a large area avalanche photodiode at low temperature for scintillation detection, *Nucl. Instr. and Meth.* **A 508** (2003) 388–393

[Yel02] S. Yellin, Finding an upper limit in the presence of an unknown background, *Phys. Rev. D* **66** (2002) 032005

[Zde04] Y.G. Zdesenko et al., Scintillation properties and radioactive contamination of $CaWO_4$ crystal scintillators, *Nucl. Instr. and Meth.* (to be published)

[Zim91] G. Zimmerer, Status report on luminescence investigations with synchrotron radiation at HASYLAB, *Nucl. Instr. and Meth.* **A308** (1991) 178–186

[Zwi33] F. Zwicky, Die Rotverschiebung von extragalaktischen Nebeln, *Helv. Phys. Acta* **6** (1933) 110–127

Acknowledgments

I thank to Prof. Dr. Rainer Kotthaus for giving me the possibility to accomplish this work within CRESST group at Max-Planck-Institut für Physik in Munich. I am grateful to Dr. Franz Pröbst who constantly supported and supervised this work. I cannot thank him enough for always taking time for answering any question, even though he was overwhelmed by work.
Thanks a lot to all the members of the Cryodetector Group at MPI in Munich.

First of all, I would like to thank my officemate Federica Petricca. She will understand if I say just thank you for being such great person. Special thanks also to Dr. Peter Christ with whom it was always a pleasure to work and share everyday problems appearing in the lab. To him I also thank for allowing the spin off of the spin off possible :-)) and for all the reading he did for this thesis. I would also like to thank to Dr. Godehard Angloher who had a wish to teach me Bavarian (up to now without success :-))). I wish to thank also to Cristina, Torsten, Stefan and Antonio for spending nice time (not only in the office) in Munich and sharing everyday problems. To Hans Seitz who made a lot of small (and not so small) pieces for me (always urgently :-))). I also thank for always practising my poor German. Thanks also to Dieter Hauff, Dr. Wolfgang Seidel, Dr. Leo Stodolsky for the interesting discussions and all the MPI group. Thank you.

Great thanks to all people from the MPI workshop that had a patience for my little ideas. Special thank to Mr. Kosmali.

Thanks also to Carlo Bucci for his support in Gran Sasso and Dr. Matthias Laubenstein for performing the radioactivity measurements on Germanium detectors in Gran Sasso. For the same measurements performed in Modane I would like to thank to Claudine Goldbach. Special thanks also to Dr. Vitali Nagirnyi who made a UV spectroscopy measurements possible and helped with a fruitful discussions. Thanks to Dr. Vitalii Mikhailik for making X-ray and VUV spectroscopy measurements possible.

Finally, I would like to thank the whole Oxford group and Garching group,

for useful discussions during the meetings. Special thank to all people from the Garching crystal lab.

For all translations and time spent on my half private problems and the paperworks I would like to thank to Uschi - thanks a lot.

Posebno bih želela da se zahvalim mojoj majci i sestri za celokupnu podršku tokom mog školovanja - Mnogo HVALA.

At the end I owe special thank to Jovica, that gave me a full support during the last years, especially for the writing period :-)) - HVALA MNOGO.